Diagnosing the Masses

A thesis submitted to the University of Manchester for the degree of

Doctor of Philosophy in the Faculty of Science and Engineering

2020

Danielle J McDougall

School of Natural Sciences

Department of Chemistry

I. Table of Contents

II. List of Figures

III. List of Tables

IV. List of Equations

V. Abbreviations

AD	Androgen Dependent
Amm Form	Ammonium formate
AS	Androgen Sensitive
BMS	Bone Marrow Stroma
Cer	Ceramide
CK	Cytokeratin
CS	Cholesterol Sulfate
DESI	Desorption Electrospray Ionisation
DG	Diglyceride
DHT	5-alpha-dihydrotestosterone
DRE	Digital Rectal Exam
ECM	Extra Cellular Matrix
ESI	Electrospray Ionisation
FFPE	Formalin Fixed Paraffin Embedded
H&E	Haematoxylin and Eosin
HEPES	(4(-2-hydroxyethyl)-1-piperazineethanesulphonic acid)
IHC	Immunohistochemistry
IPA	Iso-propanol Alcohol
ITO	Indium Tin Oxide
LASER	Light Amplification *via* Stimulated Emission of Radiation
L-Glu	l-glutamine
LMIG	Liquid Metal Ion Gun

m/z	Mass to Charge Ratio
MALDI	Matrix Assisted Laser Desorption Ionisation
MeOH	Methanol
mRNA	Messenger Ribonucleic Acid
MS	Mass Spectrometry
MSC	Microbiology Safety Cabinet
MSI	Mass Spectrometry Imaging
MTS	(3-[4,5,dimethylthiazol-2-yl]-5-[3-carboxymethoxy-phenyl]-2-[4-sulfophenyl]
MTT	3-(4,5-Dimethylthiazol-2-yl)-2,5-diphenyltetrazolium bromide
PA	Phosphatidylacid
PBS	Phosphate Buffered Saline
PC	Phosphatidylcholine
PCA	Principal Component Analysis
PCa	Prostate Cancer
PE	Phosphatidylethanolamine
PI	Phosphatidylinositol
PIN	Prostatic intraepithelial Neoplasia
PS	Phosphatidylserine
PSA	Prostate Specific Antigen
REIMS	Rapid Evaporative Ionisation Mass Spectrometry
RPMI	Roswell Park Memorial Institute
SEM	Scanning Electron Microscopy
SI	Secondary Ion

SIMS	Secondary Ion Mass Spectrometry
SRB	Sulforhodamine B
TB	Toluidine Blue
TCA	Trichloro-acetic acid
TG	Triglyceride
ToF-MS	Time of Flight Mass Spectrometry
TURP	Trans-urethral Resection of the Prostate
TX	Trypsin

VI. Abstract

Lipidomics is a growing field for mass spectrometry imaging (MSI) and ambient mass spectrometry analysis. Lipidomics is an important area of research due to the ability to gain information from downstream genomic changes. This research has demonstrated the overall strengths and limitations of a variety of mass spectrometry methods on a range of sample types, focusing mainly on the changing lipid profile. This includes desorption ionisation electrospray mass spectrometry (DESI-MS), rapid evaporative ionisation mass spectrometry (REIMS), and time of flight secondary ion mass spectrometry (ToF-SIMS).

Prostate cancer (PCa) is the primary cause of cancer related death in Western males. It is not possible to distinguish indolent and aggressive disease, therefore the patient is treated for the more severe form, leading to overtreatment and associated complications. Literature has shown that non-steroidal anti-inflammatory drugs (NSAIDs) can potentially prevent growth of PCa, offering an alternative treatment approach. This study demonstrated that mass spectrometry imaging MSI methods such as DESI and SIMS are able to distinguish between PCa cell lines in combined pellets by observing the differences in the lipid profile. The response of the NSAID ibuprofen on PCa cell lines varying in clinical aggression was examined using MSI. As a result, it was established that ibuprofen was able to diminish the metabolic activity of the cancerous cell lines, LNCaP, LNCaP-C42 and LNCaP-C42B, sparing the normal epithelial line, PNT2-C2. This drug interaction caused significant changes to the intensities of several lipid classes including phosphatidic acid (PA) and phosphatidylinositol (PI) species. This research validated the combined strengths of these MSI techniques when used together. The potential of ambient methods such as REIMS was examined, focusing on optimising the setup for lipid profiling. Overall this thesis has outlined the benefits of MSI methods both on their individual merits and when used together for lipidomic analysis.

VII. Declaration

No portion of the work referred to in the thesis has been submitted in support of an application for another degree or qualification of this or any other university or other institute of learning;

Copyright statement

i. The author of this thesis (including any appendices and/or schedules to this thesis) owns certain copyright or related rights in it (the "Copyright") and s/he has given The University of Manchester certain rights to use such Copyright, including for administrative purposes.

ii. Copies of this thesis, either in full or in extracts and whether in hard or electronic copy, may be made **only** in accordance with the Copyright, Designs and Patents Act 1988 (as amended) and regulations issued under it or, where appropriate, in accordance with licensing agreements which the University has from time to time. This page must form part of any such copies made.

iii. The ownership of certain Copyright, patents, designs, trademarks and other intellectual property (the "Intellectual Property") and any reproductions of copyright works in the thesis, for example graphs and tables ("Reproductions"), which may be described in this thesis, may not be owned by the author and may be owned by third parties. Such Intellectual Property and Reproductions cannot and must not be made available for use

without the prior written permission of the owner(s) of the relevant Intellectual Property and/or Reproductions.

iv. Further information on the conditions under which disclosure, publication and commercialisation of this thesis, the Copyright and any Intellectual Property University IP Policy (see http://documents.manchester.ac.uk/display.aspx?DocID=24420), in any relevant Thesis restriction declarations deposited in the University Library, The University Library's regulations (see http://www.library.manchester.ac.uk/about/regulations/) and in The University's policy on Presentation of Theses.

VIII. Appreciation and Thanks

I would like to offer a huge thank you to my supervisors Professor Nick Lockyer and Dr Adam McMahon for their continual support and encouragement throughout the work undertook. They have enabled me to keep motivated and excited about my project throughout.

I would also like to thank Dr Mick Brown and Dr Claire Hart. Without their support and collaboration I would not have been able to work with the prostate cell lines.

Thanks must also go to my secondary sponsors; Waters Corporation. Specific appreciation goes to Emrys Jones and Vlad the robot. I am truly grateful for his help and advice during my time at Waters.

I would also like to give a huge and heartfelt acknowledgment to my family, especially my mummy. They have given constant support throughout my whole academic career, as well as pushing me when I doubted myself. They have stood by my side and were there for me throughout each and every step that was taken. Without their love and encouragement I would not have made it this far and for that I am truly thankful.

I would also like to express my gratitude to the Chamber. Having such a close group of friends by my side throughout this time has been a blessing. Your love and support has helped me endless amounts.

And finally, to Matthew Gentry, my PhD partner in crime! Thank you for all of your support, love and care and your continued friendship despite my constant freak-outs and breakdowns! I wouldn't have been able to do this without you by my side. Thank you

IX. COVID-19 Impact Statement

The secondary funding of this research was awarded by Waters Corporation, Wilmslow. This was given under the premise that the majority of work and research would be undertaken at the Wilmslow site. However, during the COIVD-19 lockdown, this site became restricted to authorised personnel only, and has yet to reopen for non-essential work. This created a large problem as not only is most of the instrumentation used during this thesis based at this site, but also no external access to data was given. Therefore, all further experimentation using Waters instrumentation was halted following lockdown. This specifically affected any REIMS work, as the only set up of this system is at the Wilmslow site.

Also, during this lockdown, all lab-based activity at the University of Manchester was suspended, including cell culture, and all non-essential instrumentation ordered to be turned off and vented. It must also be discussed that the arrival and installation of the J105 chemical imager, the instrument responsible for the ToF-SIMS data within this thesis, occurred in February 2020. Therefore, the time that would have been spent acquiring additional data was severely impacted. This also led to an effect of limited access to data and the designated processing PC to aid in analysis of the collected data.

The COVID-19 lockdown had an overall large impact on the final confirmatory analysis for the overall thesis. Therefore, this research that could be done for this thesis was seriously impacted, due to lack of instrumentation, sample access and restricted access for data processing.

Chapter 1

The Involvement of Lipid Species in Prostate Cancer

1. Introduction to Prostate Cancer

1.1. Introduction

Prostate cancer (PCa) is the second most common malignancy, globally, and the primary cause of cancer deaths in western males. Despite the number of new cases of PCa decreasing over the past 3 years, it is still considered a significant health issue. It is estimated that approximately 16% of all men will be diagnosed with PCa at an average age of 67 years old.[1] PCa is a very slow growing malignancy; however, it has the predilection to metastasise to the bone marrow stroma (BMS). Once PCa has reached this stage it is estimated that the patient has a significantly reduced survival rate.[2]

1.1.1. General morphology

The prostate, an organ unique to the male reproductive tract, is a branched exocrine secretory gland. Weighing approximately 18 grams, the prostate is found below the bladder with the urethra running through the centre. The function of the prostate gland is primarily for semen secretion. This is a thin, milky fluid with a pH of 7.5 which assists in transportation of sperm for successful fertilisation of the female ovum. The alkalinity of the semen aids in increasing the lifetime of the sperm due to the inherent acidity of the vagina. The sperm and fluid from the vas deferens contributes to approximately 10% of the seminal fluid produced.[3]

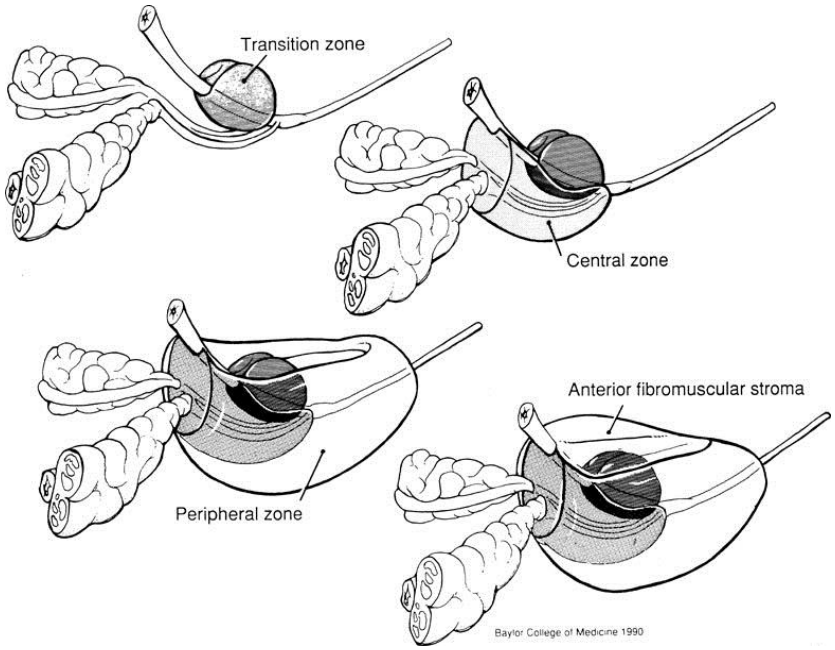

Figure 1.1: A diagram depicting the clinically significant zonal regions of the prostate[4]

There are three main glandular regions that define the prostate; the transitional, the central and the peripheral zone (Figure 1.1).[5] Normal prostrate epithelium contains luminal epithelial cells, basal cells and a small amount of neuroendocrine cells that are scattered throughout the prostate (Figure 1.2).[6] The luminal cell is a androgen-dependant cell that primarily expresses high levels of the prostatic secretory proteins, including; low molecular weight cytokeratin protein (CK 5/6), prostate specific antigen (PSA), and androgen receptor.[7] CK are antibodies with CK 5/6 being an intermediate sized basic protein that protects the epithelial cell from damage or stress[8]. In normal healthy tissue these proteins are mainly expressed by the epidermis and the squamous epithelium as well as basal cell layers in the case of prostate gland.[9,10]

In particular, the PSA is most useful in the detection of any prostate malignancies, which will be discussed in greater detail later on. Conversely, the basal cell layer expresses the high molecular weight CK and p63, which is a tumour protein.[11]

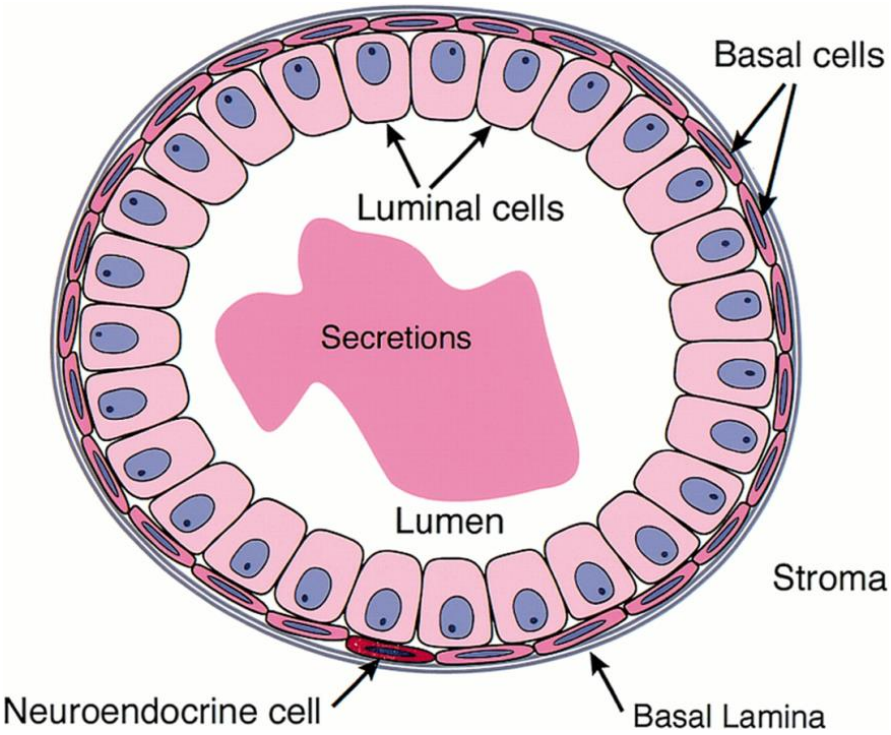

Figure 1.2: A diagram depicting the different cell types observed within the prostate gland.[7]

1.1.2. Androgen involvement

Androgen is a term for a male steroid hormone that is involved in stimulation and control of the development and maintenance of male characteristics. The most well understood androgen is testosterone; however, androgen also refers to 5-alpha-dihydrotestosterone (DHT), androstanediol, androstenedione and androsterone.[12]

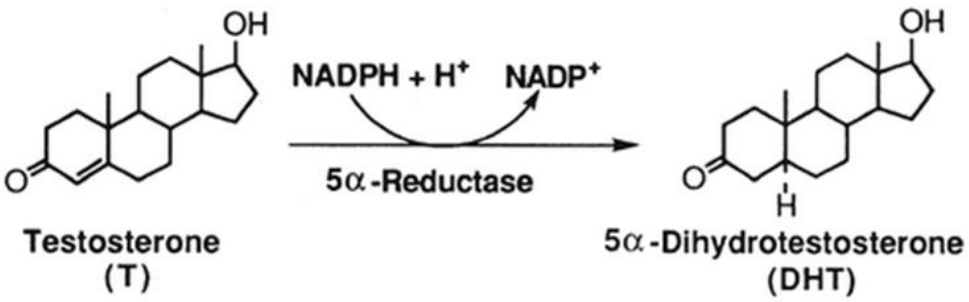

Figure 1.3: Chemical structure of testosterone and 5-alpha-dihydrotestosterone including the co-factors needed for the conversion.[13]

The growth of early prostate cancer requires 5-DHT which is a metabolite of the 5-alpha reductase system and produced from testosterone (Figure 1.3). These cells are dependent on the concentration of androgen present and therefore are referred to as androgen dependant (AD). However, later stages of the disease may respond to androgen but do not specifically depend on its presence for growth. These cells are androgen sensitive (AS). Therefore, it has been postulated that the metastatic disease can be treated by hormone therapy to prevent cancer growth, however once the tumour surpasses the AD stage, hormone therapy is no longer an option.[14]

1.2. Prostate Cancer Types

There are a number of different cancer models that stem from prostate cancer. Each of these models has a different mode of metastasis as well as differences in their androgenic response.

1.2.1. Prostatic adenocarcinoma

This is the most common type of prostatic cancer that occurs in humans, making up 90-95% of all diagnoses. Adenocarcinoma occurs in the luminal cells which line the organ, typically

where the secretion of semen occurs. This is a slow growing form of PCa and is usually found early enough for curative methods. It is proposed that due to the slow growing nature of this cancer, this won't affect a number of men within their lifetime.[1] It has been shown that a large proportion of adenocarcinomas occur within the peripheral zone, whereas only 25% of adenocarcinoma tumours are present in the transitional zone. However, this presents difficulty in distinguishing between adenocarcinoma and prostatic intraepithelial neoplasia (PIN) as this also develops mainly in the peripheral zone. The epithelial layer cells form a monolayer which is a major histological identification point that distinguishes adenocarcinoma from the double layer found on benign BPH.[15]

1.2.2. Prostatic small cell carcinoma

Prostatic small cell carcinoma (PSCC) is considered one of the more aggressive forms of PCa that does not lead to a change in PSA values. Therefore, it is extremely difficult to diagnose and often leads to detection at a more advanced stage.[1] In most cases this cancer will spread to the surrounding bone marrow stroma (BMS). PSCC produces osteosclerotic bone metastases as it has a tendency to target the skeleton. However, in addition to BMS metastases, this cancer has been known to spread to the lymph nodes, lungs and adrenal glands.[16] It has been suggested that once the cancer has reached the metastatic stage that the patient is classed as terminal due to the aggressive nature of the metastases.[1]

1.2.3. Prostatic Intraepithelial Neoplasia

Prostatic intraepithelial neoplasia (PIN) is a condition witnessed in males which is defined by a neoplastic growth of epithelial cells in pre-existing prostatic ducts.[17] High grade PIN (HG-PIN) is the most likely precursor of prostatic carcinoma.[18] Analysis of HG-PIN highlights most of the phenotypic, biochemical and genetic changes seen with adenocarcinoma,

however, there is no invasion of the basement membrane of the duct, typical of malignancies. As HG-PIN is the most likely pre-cursor to PCa, being able to detect and prevent further damage would be clinically useful.[19] Unfortunately, the only detection method of PIN is biopsy. Although it tends to increase PSA levels in the blood serum, there is no direct correlation.[17]

1.3. Cell lines

Over the years a number of cell lines have been derived and immortalised from a number of prostate carcinomas and the consequential metastasis. These cells lines enable experimentation into the causes, treatment, and potential prevention of prostate cancer. Extensive studies have been performed over the past few decades using these cell lines, providing a better understanding of the biology, aetiology, and pathology of the disease.[20]

1.3.1. LNCaP

The LNCaP cell line is one derived from culture explants from a needle biopsy from a patient suffering with lymph node adenocarcinoma of the prostate. The LNCaP model grows readily *in vitro* with a doubling time of approximately 60 hours. This model maintains malignant properties and therefore shows the potential usage of these cells, not only *in vitro,* but also in athymic nude mice as they develop tumours at the injection site.[20] This property holds many benefits, particularly with respect to 3D imaging possibilities. LNCaP demonstrates a good model for androgen dependent prostatic cells and offers the possibility to study the involvement of hormones and androgen response on the growth rate and other homeostatic factors.[21] LNCaP cells contain a number of androgen receptors, whilst oestrogen and progestin receptors are not detectable. It has been shown that the

presence of androgens not only directly affects the growth *in vitro* but also indirectly as it makes the cells more sensitive for growth factor mediated stimuli.[22] Overall, LNCaP has proven to be an effective model for lymph node metastatic prostate cancer despite its low metastatic potential.[23]

1.3.2. LNCaP Derivatives

There are several, well established, derivatives of the LNCaP Cell line. Experimentation continued on this cell line in the 80's and this cells were injected as a xenograft into a nude mouse, creating an LNCaP tumour on the flank of the mouse. This produced a slightly more invasive model of the cell line named LNCaP-C4-2. Following this, the mouse underwent metastatic mutations due to the cancer, spreading to the BMS. These cells were then isolated and immortalised as a much more aggressive and invasive model, LNCaP-C4-2B.[20,21]

1.3.3. PC-3

A unique feature of prostate cancer is that is oestrogenic and therefore results in the formation of bone metastasis. PC-3 cells were derived from bone metastasis of a grade IV prostate cancer patient. PC-3 lacks the androgen receptor and the metastatic potential of PC-3 is much higher than that of LNCaP and its derivatives, which is considered to be moderately metastatic. PC-3 has been demonstrated as a more aggressive and invasive cancer type of prostatic small cell carcinoma.[6]

1.3.4. PNT2-C2

In order to fully explore the differences between cancers, it is essential to have a biological control such as a normal cell line. The cell line use for this is PNT2-C2. It is ideal as a

biological control as it is a normal human epithelial cell line and primarily non-tumorigenic. Using the SV40 protein, this cell line was derived and immortalised in the early 1990s and holds many characteristics that are unique to healthy tissue.[24] This cell line naturally secretes PSA protein and is androgen sensitive, as is typical for normal prostatic tissue. Therefore this cell line provides a good biological control for this thesis.

Table 1-1: A table describing the key characteristics of a number of relevant prostate cancer cell lines

Cell line	Model	Androgen sensitivity	PSA secretion	Metastasis
LNCaP	Human	AD	PSA +	Lymph node
LNCaP-C4-2	Mouse	AI	PSA +	Bone Marrow Stroma
LNCaP-C4-2B	Mouse	AI	PSA +	Bone Marrow Stroma
PC-3	Human	AI	PSA -	Bone Marrow Stroma
PNT2	Human	AS	PSA +	N/A

1.4. Current Clinical Detection Methods

1.4.1. Clinical testing

It is currently very difficult to distinguish indolent and aggressive disease, leading to overtreatment and associated complications. The most commonly used test for those at higher risk of PCa, is detection of the prostate specific antigen (PSA) protein in the blood serum.

1.4.1.1.Prostate Specific Antigen

PSA is a 33 kDa protein which, as mentioned earlier, is secreted exclusively by the prostatic epithelium. PSA is detectable at much higher concentrations in the semen than the blood serum, at mg/ml and ng/mL respectively. However, this is by no means diagnostic as PSA can be increased *via* a number of non-cancerous states.[25] Despite this, screening for PSA

combined with a digital rectal exam (DRE) of the prostate is presently the most valuable approach in the early detection of PCa.[26, 27]

1.4.2. Immunohistochemistry

Immunohistochemistry (IHC) is another important method in the detection and classification of PCa. This is a staining method, utilising the specificity of binding of antibodies to antigens within tissue biopsy sections. IHC uses specific antibodies labelled with dyes and fluorescent markers to allow for spatial and semi-quantitative information about the localisation of particular biomolecules.[28]

1.4.2.1. Haematoxylin and Eosin

The current gold standard for IHC in the detection of PCa is haematoxylin and Eosin (H&E).[29] This enables pathologists look specifically at the morphology of the tissue.

1.4.2.2.Gleason Grading

The Gleason grading system was initially based on research undergone in 1959. This study enrolled a total of 270 men, all diagnosed with prostate cancer. The principle researcher in this project was Dr Donald Gleason. This research demonstrated two typical histologic patterns exhibited within the tumour biopsy samples. From this, a score was created combining the sum of these two common grade patterns to achieve an overall score ranging from 2-10. It was concluded that a higher Gleason score corresponded to a progressive increase in the patient mortality. From this, five classes were created by using distinctive prognostic patterned observed within the tissue (Figure 1.4).[30]

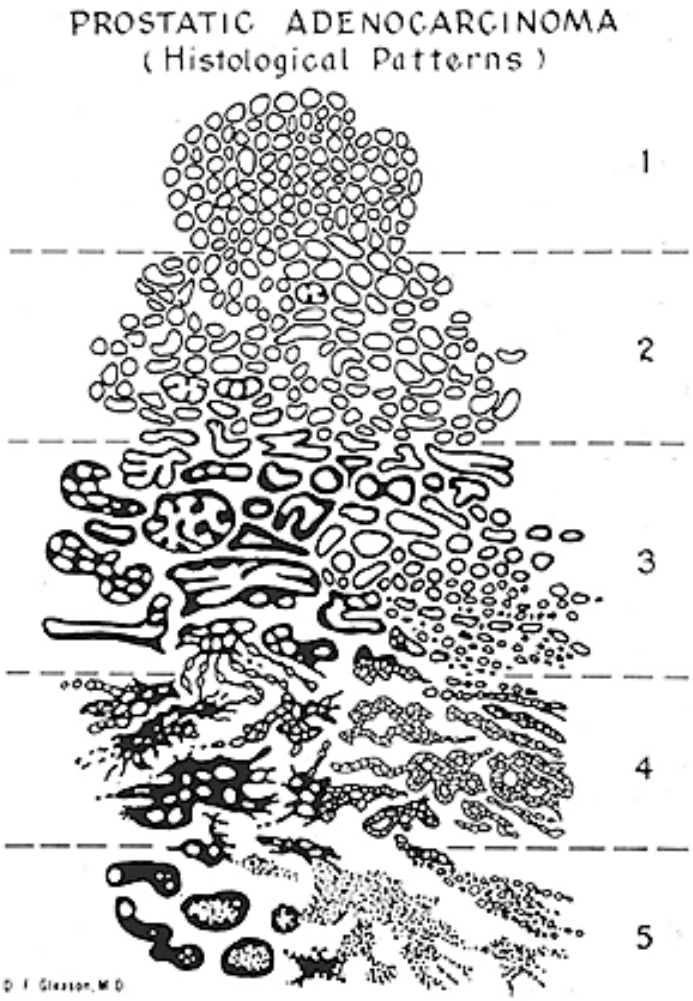

Figure 1.4: Gleason score diagram [31]

The total Gleason score is calculated by summing the scores of the two major cell anatomies. The first number being that of the most dominant cell morphology and the second number that of the non-dominant cell morphology.[32] Example Gleason graded images (Figure 1.5) show the morphology that is typical for each grade.

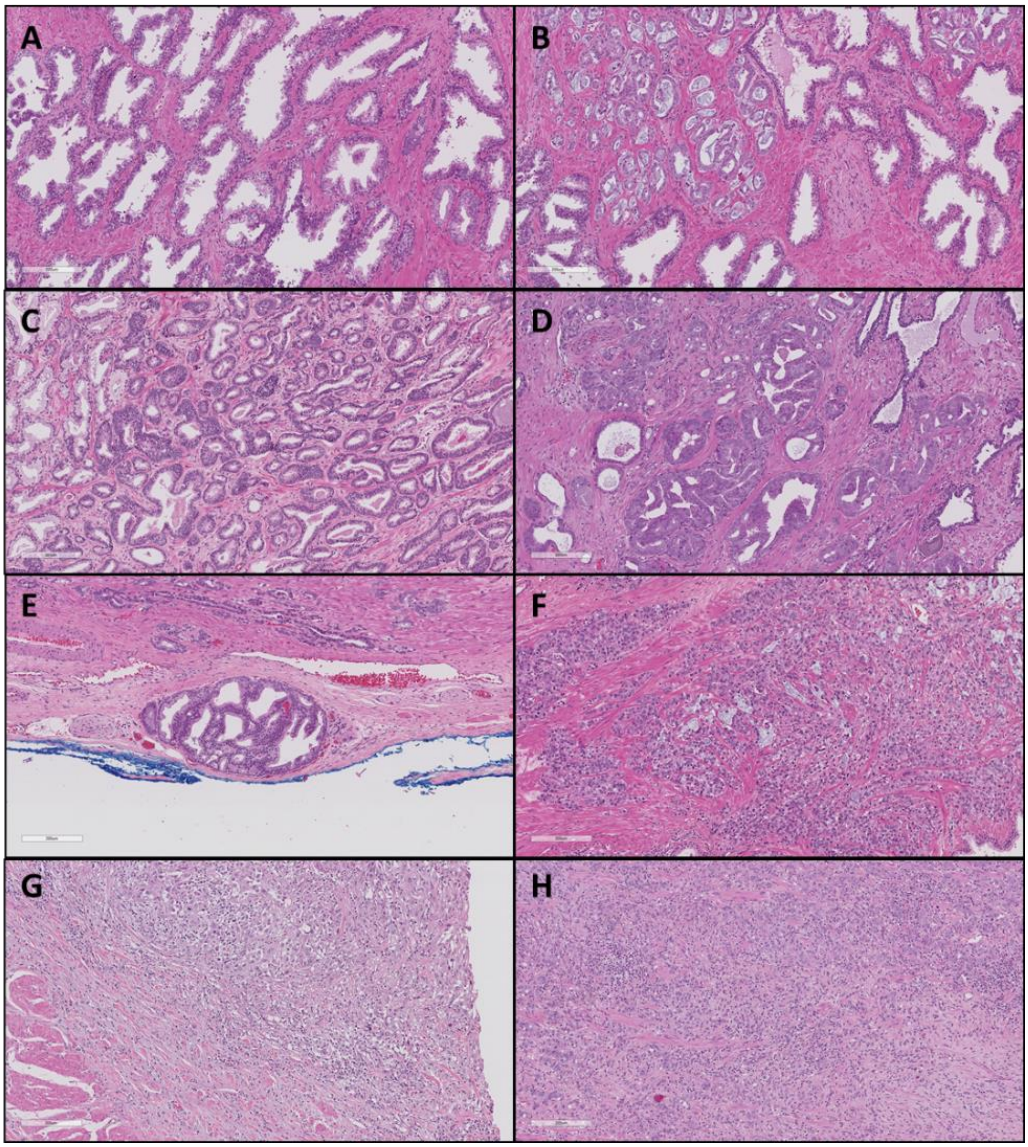

Figure 1.5: H&E stained prostate sections, graded by an in-house pathologist. (A) demonstrates healthy prostate tissue without a Gleason score, (B) Gleason score 3, infiltrating normal glands (right hand side), (C) Gleason score 3+3, (D&E) Gleason grade 4 with cribriform growth, (F&G) Gleason score 4+5, (H) Gleason score 5+5.

Healthy prostate tissue should have small regular epithelial nuclei, stained blue by haemotoxin, surrounding vascular structures throughout the section. On the other hand, as the cancer progresses and the gleason score increases, tightly packed irregular regions of cells and smaller stromal areas are observed. At the highest gleason grade, 6+6, there is very little to no vascularisation and tight clumps of infiltrating cells make up the tissue.

1.4.2.3.Immunofluorescence

While H&E staining provides information about the morphology and structure of the sample, it does not acquire information about the gene expression profiles of the cells. Genetic profiling provides functional data about the sample, giving further information with regards to disease likelihood and other factors.[33] Immunohistochemical staining of tissue exploits the genetic changes within a sample using antibody binding to specific antigens on the surface of samples. Using fluorescent markers, this staining can allow for visualisation of the distribution of specific cellular changes and components within the sample. Therefore, IHC staining is a highly useful technique in order to extend and improve upon existing images.[34]

1.5. Introduction to Lipids

Lipids by nature are highly non-polar due to their long acyl chains and general hydrocarbon composition. However, there are some exceptions to this such as cholesterol. These species do not contain long acyl chains, however, are non-polar and soluble in organic solvents. Of the main biological molecules that make up tissue, lipids are possibly the most varied, structurally. This diversity can be categorised into individual groups including fatty acyls, glycerolipids, glycerophospholipids, sphingolipids, sterols and prenols (Table 1-1).[35]

Table 1-2: The main lipid classification groups and the corresponding sub classifications of lipid species showing their generic structure with R representing the fatty acyl chain based on the classification from LIPID MAPS. The asterisks highlights the general structure shown

Classification	Subcategory	General Structure*
Fatty Acyls (FA)	Fatty acids (FA)	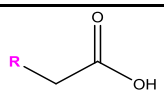
Glycerolipids (GL)	Monoacylglycerols (MAG) Diacylglycerol (DAG)* Triacylglycerol (TAG)	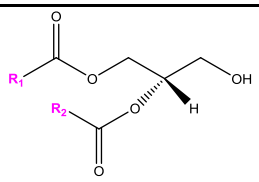
Glycero-phospholipids (GP)	Glycerophosphocholine (PC)* Glycerolphospho-ethanolamine (PE) Glycerolphospho-serine (PS) Glycerolphospho-glycerol (PG) Glycerolphospho-inositols (PI)	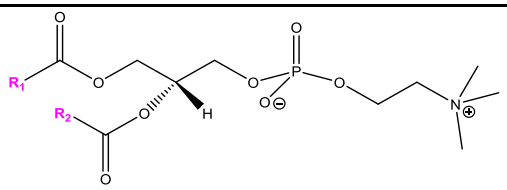
Sphingolipids (SP)	Sphingoid bases Ceramides	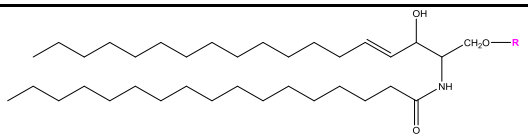
Sterol Lipids (ST)	Sterols Steroids Secosteroids Cholestane skeleton*	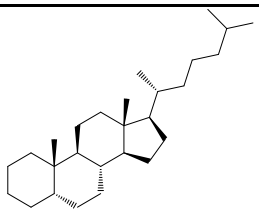
Polyketides (PK)	Linear Polyketides Flavonoids	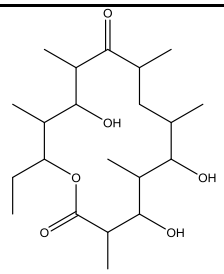
Saccharolipids (SL)	Acylaminosugar	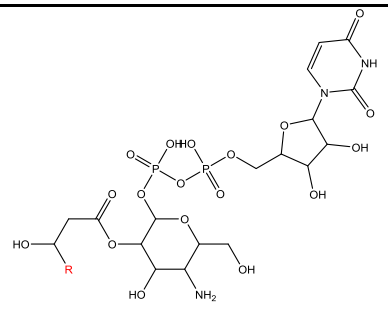
Prenol Lipids (PL)	Isoprenoids Polyprenols	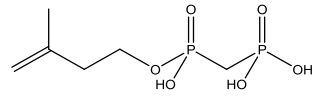

Lipids are involved in membrane structure, cell signalling, and energy production. The crucial role of lipids in a biological system can be demonstrated by the large number of studies involving diseases that disrupt the lipid metabolome.[36] Lipid levels in biological systems are tightly regulated, spatially, therefore any deregulation of this network can be considered to contribute onset of a pathological concern. This makes lipidomics ideal for diagnosing and informing treatment decisions for diseases such as cancer, due to the high lipid content found in the most tissue as well as the role of lipids in cancer biology.

1.5.1. Lipid classes

The term 'lipid' has been defined as a substance of biological significance that is insoluble in water.[37] Therefore, as this definition is highly broad, this leads to number of highly diverse species that are defined as lipids. Therefore, the fundamental building blocks of each compound were explored to classify these species focusing mainly on the ketoacyl groups and isoprene groups. Based on this system, 8 major categories were defined based on the structural makeup of the lipids (Table 1-2).[38]

1.5.2. The role of lipids in cancer

The role of lipids in cancer is becoming more emphasised than ever due to the presence of new methods and techniques with the ability to detect changes in lipids. A key attribute of cancer tissue is the need for a constant source of FAs and cholesterol. It has been theorised that this is due to increased need for membranes to enable growth, division, and also to enable processes such as metastasising and dissemination to other areas of the body.[39] Early research exhibited increased levels of cholesterol and overall fluctuations in the phospholipids in tumour samples. These changes also extended to other cell types in the tumour micro environment. It was discovered that a highly expressed tumour specific

antigen (OA-519) in breast cancer, encodes for fatty acid synthase (FASN).[40] Since then, literature has illustrated the ability of cancer cells to alter lipid metabolism. Studies have shown that cancer can lead to changes in fatty acid saturation, which in turn leads to the alteration of properties and aspects of cellular machinery. This can cause changes within the cell lipid uptake to *de novo* lipogenesis, which is the process of acetyl-CoA being synthesised into fatty acids. This leads to an overall increase of saturated phospholipids in the cell membrane.[41] Normal cells predominantly depend on the uptake of free FAs from the circulating blood supply. However, for cancerous cells, the activation of *de novo* FA synthesis changes the properties of FA metabolism altering the uptake as well as allowing for modification and degradation of the FA species.[42] Fatty acid synthesis is typically an anabolic process, involving the conversion of carbons extracted from nutrients into FA chains. The source of these carbons is primarily provided from citrate which comes from the tricarboxylic acid cycle (TCA) cycle. Free FA can then be esterified via the glycerol phosphate pathway to convert into the tail moieties of phospholipid species which in turn constitute the main building blocks of the cell membrane.

1.6. The detection of cancer using mass spectrometry imaging techniques

As prostate cancer has been tenuously linked to diet, particularly in Western males, using an approach that encompasses environmental factors is beneficial. Using techniques such as mass spectrometry to globally detect the metabolites found in a biological sample such as cell cultures, blood plasma, or histological sections can be subjected to statistical analysis to show which metabolites are up or down regulated between groups. As a result any important features detected can then be applied to a biological pathway in order to diagnose biomarkers of a disease or outline a treatment, making metabolomics a useful

clinical application. Once a pathway has been highlighted, a more targeted approach can be applied where certain metabolites are examined one at a time. This will increase the overall sensitivity and accuracy of the results, but the overall number of visible metabolites will diminish. Metabolic alterations are associated with increased mortality in prostate cancer to the fatty acid synthase pathway. Lipidomics analysis of PCa has shown that a variety of lipids are changed during the cancer process such as CE, PE, PC and SM.[43] With the direct link between lipids and many cancers, MSI is an appropriate platform for studying prostate cancer in more detail.[44] Although the changing lipid profile is the target for this research, it is also important to consider the global changes that are also occurring within cancerous tissue. Using a large and diverse variety of mass spectrometry techniques, the literature has demonstrated the ability to detect and understand the changes occurring to the cancer micro environment. It has been demonstrated that understanding each layer of change and mapping these to give a thorough understanding and overview of the metabolism of the tissue is vital in the role of curing cancer.[45] This highlights the advantage of using a range of mass spectrometry methods, giving a plethora of data and enabling thorough understanding of the sample in question. As a result, the mass spectrometry techniques used in this research will examine the merits of these methods both individually and when used together.

1.6.1. Mass spectrometry introduction

Mass spectrometry (MS) is one of the most extensively used analytical techniques in biological and biomedical research due to its high versatility and comprehensive coverage. It can be used in a plethora of applications from forensics, to pharmaceuticals, and clinical diagnosis. Mass spectrometry generates rapid, high sensitive, qualitative and quantitative information, hence its application in research. MS produces ions from a sample which are

separated based on their mass to charge ratio (*m/z*). These ions will be detected by the instrument and transformed into a spectrum of *m/z* values versus the relative signal intensity. This technique can be used to determine the structure of a molecule, physical properties of a sample, and reaction dynamics.[46] The first fully functioning mass spectrometer was produced in the 19th century by the Cavendish laboratory in the University of Cambridge.[47] Since then a large range of mass spectrometers have been produced, each generating and detecting ions in different ways. Some of the most popular commercially available mass analysers available today include; time of flights, quadrupole mass filters, and ion trap instruments, each of these having their own benefits as well as disadvantages. Since mass spectrometry is adaptable, it can be used as a standalone instrument or in tandem with other analytical techniques such as chromatography, ion mobility or, most importantly for this project, imaging platforms. These provide separation of the molecules in the sample, allowing for a second or even third dimension of analysis.[48]

Imaging techniques have been used as a standard tool for biomedical research and more specific to this project, over the past decade, mass spectrometry imaging (MSI) has grown in popularity and importance.[46] Its ability to acquire molecularly specific images combined with histological information has enabled an overlap of information, using mass spectral information to explain regions of histological significance. Using the spatial distribution of molecules in the sample, MSI maps the chemical identity of species as a function of their position on the surface.[49] Although, it must be considered that an increase in spatial resolution ultimately leads to a decrease in signal intensity and therefore this causes a reduction in quality of the ion images as well as affecting the time for acquisition.[4] Imaging techniques are an essential process for medical applications. For example, in managing cancer, imaging techniques are vital in areas of diagnosis, indicating abnormalities and guiding treatment and biopsies. Lateral resolution is a key factor in procuring high quality images and there are many factors that influence resolution of the image. The defined pixel

number denotes the number of points of data the instrument will acquire, and the pixel size defines the resolution within the defined space. Other factors have influence, such as sensitivity, probe beam size, spot size, and matrix applications. These factors are instrument and technique dependent and will be discussed in greater detail later.

1.6.2. Secondary Ion Mass Spectrometry

Secondary ion mass spectrometry (SIMS) is a highly useful tool in the analysis of biological substances down to sub-cellular sizes at physiological concentrations. SIMS is a form of chemical analysis that is capable of distinguishing the composition of elements and small molecules on the surface or near the surface of a sample, with down to sub-micron spatial resolution.[50]

SIMS analysis allows for the detection and identification of surface molecules by using a primary ion beam to target the surface of a sample, creating secondary ions which will be detected and analysed. A number of sources are used for SIMS analysis, including monoatomic sources, large poly-atomic cluster sources and liquid metal ion guns. Each source type demonstrates a difference in sensitivity as well as the method in which ions are generated. Each ion beam has a number of benefits as well as disadvantages, which will be discussed later in more detail.

One of the main advantages of SIMS is the high spatial resolution it can achieve. SIMS has been shown to be very successful in imaging low molecular weight, targeted inorganic compounds and biomolecules with spatial resolution reaching down to <100 nm. SIMS is a surface sensitive technique, with the ion beam interacting with the only the topmost monolayers of the sample, down to ~10 nm in depth.[49,51]

1.6.2.1.Secondary ion formation

Secondary ions are formed *via* the high impact energy of a primary ion beam, usually between 5-40 keV. This bombardment causes collisions between the ions and molecules at the surface of the sample, resulting in the sputtering of molecular fragments and atoms.

Equation 1

$$I_i = I_\emptyset \, Y_i \alpha \theta_i \eta$$

Where:

I_i is the detected current of species *i*,

$I_\emptyset$ is the primary ion flux,

Y_i denotes the sputter yield,

θ_i gives the fractional concentration of the chemistry of species *i* on the surface,

α defines the ionisation probability

η is the transmission of the analysis system.

This equation allows for the explanation of the relationship between the emission of the particles with respect to the chemical configuration of the species at the surface (Equation 11).

1.6.2.2.Sputtering Effect

The sputtering effects seen can have an effect further down the sample to an extended lattice zone (Figure 1.6). This is witnessed as a perturbation of the ions below the surface.

However, a fraction of this dissipation of energy from the primary ion to the lattice will reach the surface once again and will induce the emission of a surface particle.

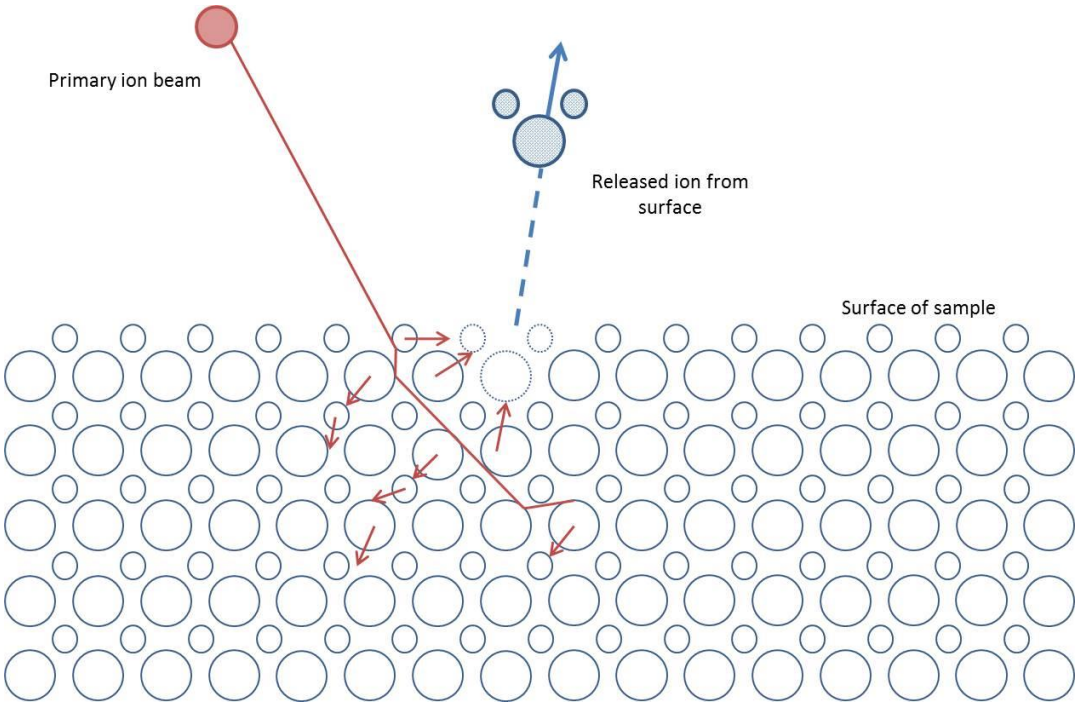

Figure 1.6: Sputtering effect seen during secondary ion mass spectrometry, where the red arrows indicate the interaction of the molecules within the sample and the blue arrow highlights the production of an ion from the surface. Adapted from A. Benninghoven et al[52]

During the sputtering process, secondary neutrals and photons are produced. As a result, only a small proportion, between 10^{-5} and 10^{-2}, of the sputtered molecules are ionised and as they leave the surface, are accelerated by a potential difference towards an appropriate MS platform.[52] There are a number of processes involved in SIMS that can affect sputtering. A number of studies have been taken to understand the essential physics on this effect. It has been theorised that the disappearance cross section (σ) is an indication of the average extent of damaged area. However, as Delcorte et al. show using molecular dynamic simulations, this value varies for different fragments.[53]

Equation 2

$$J_i(\emptyset) = J_{i0} \exp(-\sigma_i \emptyset)$$

Equation 2 links the primary ion flux (φ) to the intensity of fragment J (I_i) at zero fluence (J_{i0}) and the disappearance cross section of species i (σ_i). As a result, the decay caused by an ion impact can be measured by using an exponential fit. This can be used to show that the disappearance cross section of fragments can be correlated to the ejected species size.

1.6.2.3.Ion sources

The development of different ion sources has allowed for increased sensitivity for the instrumentation. The primary ion beam situated on the SIMS instrumentation are typically liquid metal ion guns (LMIGs). These beams are classically highly focused, translating into a high lateral resolution during the imaging process. The original LMIGs developed used metals such as indium and gallium as the sources. However, recent developments have highlighted that gold and bismuth cluster ion sources allow for a greater yield of secondary ions produced.[50]

Over the years a number of ion sources have been established in order to improve the overall resolution and sensitivity of the instrumentation, specifically in the development of cluster ion beams. Polyatomic cluster ion beams are a much gentler technique and therefore cause less destruction of the surface during analysis. These clusters are based on C60 carbon allotrope, fullerene[55] or Ar-clusters[56] which typically consist of 2000 Ar atoms[57], are most useful in the characterisation of large bio-molecular structures. The advantage of these sources compared to LMIGs is that the kinetic energy caused by the impact of these large clusters, is spread across a larger number of atoms causing a reduction in the energy

per impacting atom, as opposed to one high energy impact from a singly charged atom. As a result the overall damage caused to the molecular structure of the surface is greatly reduced. The polyatomic-cluster ion gun causes a much wider crater formation on the surface of a sample; however, overall less damage to the underlying layers is caused.[48]

1.6.2.4.Static SIMS

Static SIMS minimises the probability of detecting damage caused by the primary beam, which ensures that <1% of the surface is perturbed. This mode renders this process 'non-destructive' as the likelihood of an ion impacting with the same area of surface is extremely low. In order to maintain this, the primary ion beam dose that can be used is limited, usually to around 10^{12} ions per cm^{-2} of sample (~1% of the sample surface). This value is known as the *static limit*. However, this limit consequently affects the amount of secondary ions produced for detection.[48] Another pitfall observed by static SIMS is known as the matrix effect. As long as the species in the surface are found in the same chemical environment, there will be no difference in the ionisation potentials and transformation probabilities, as is shown by the single species, i ,in Eqn. 1. If the species differ there would need to be multiple coefficients to represent this. However, once the chemical environment changes between surface species, as does the transformation probability of the species. Therefore, direct quantitative analysis requires matrix-matched standards. A good way of mitigating this affect is by using internal standards or internal calibrations.[51]

1.6.2.5.Dynamic SIMS

As the ion beam dose increases and breaches the static limit, this will cause an erosion effect on the sample to reveal lower layers, therefore causing much more destruction of the sample. This is known as dynamic SIMS, which has shown to be particularly useful in

characterisation of interfaces of samples as well as molecular depth profiling of biological samples. An increase in the ion beam dose will cause deeper layers of the sample to become exposed allowing for profiling of internal regions for analysis. Dynamic SIMS mode has shown a significant amount of benefit when depth profiling biological samples as it allows for more signal to be acquired, providing the sample is not sensitive to amplified damage as a result of the increased ion beam dose.[58]

1.6.3. Instrumentation

1.6.3.1.J105 3D Chemical imager

One of the SIMS instruments that will be utilised during this project was developed by the Surface Analysis Research Centre based at the University of Manchester in collaboration with Ionoptika Ltd. This is the J105 ToF-SIMS 3D chemical imager instrument equipped with a C_{60} cluster ion gun and an argon gas cluster ion beam (GBIC) (Figure 1.7).

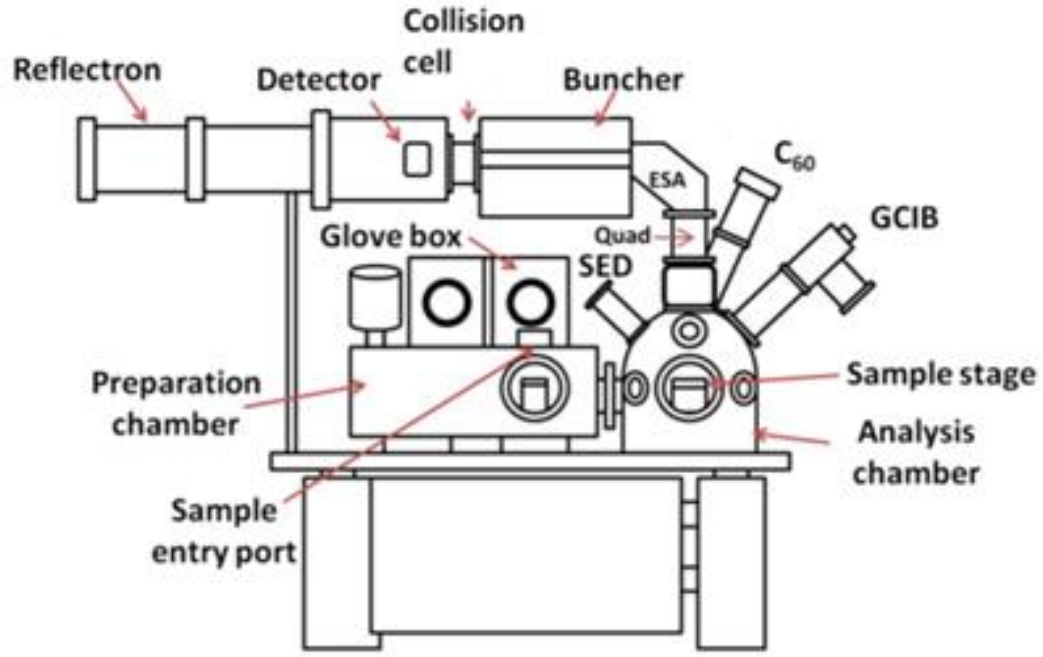

Figure 1.7: Schematic diagram of the J105 3D Chemical Image [59]

The sample is inserted into the analysis chamber *via* the preparation chamber. Once the sample has been brought down to vacuum, it moves to the stage where the position is optimised according to the sample. It is here where ionisation occurs. The produced ions will be extracted through the mass spectrometer to the buncher-ToF for analysis. The buncher-ToF is a linear system of plates and electrodes which collect secondary ions for 85 µs, and allows for pulsed extraction of the ions every 15 µs. This results in a compression of the ion packet and the spatial dimension of these determine the mass resolution.[60] The ions exiting the buncher then pass through the reflectron analyser twice before hitting the detector with a flight time dependent on their *m/z*.

1.6.3.2. Time of Flight Analysers

ToF analysers have been described since 1946.[61] The nature of the ToF analyser is suited to the pulsed nature of SIMS. The liberated secondary ions are accelerated at a fixed potential towards 2 and 8 keV allowing for all SI's to have equivalent kinetic energy. These are then

passed through a free field region, known as the flight tube, and the *m/z* spectrum is determined by the flight time of the ions through the flight tube as heavier ions will take longer to reach the detector than those with smaller masses (Figure 1.8).

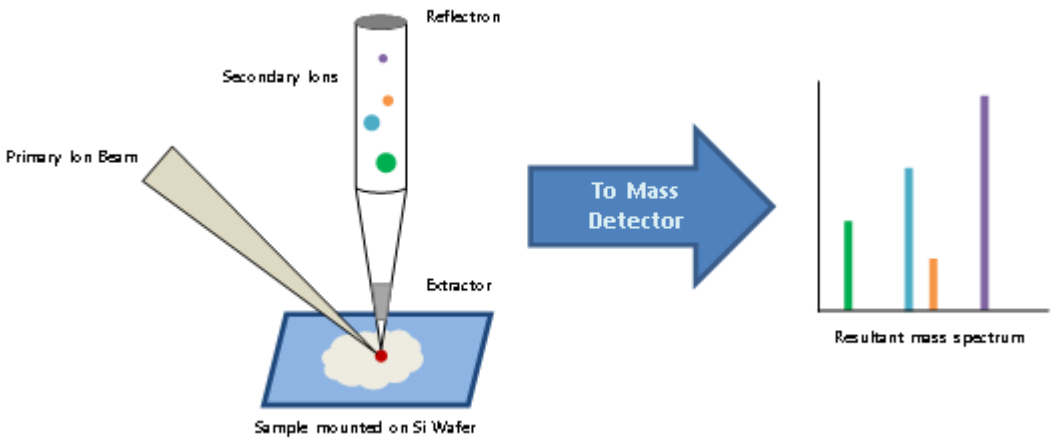

Figure 1.8: A schematic diagram of secondary ion mass spectrometry (SIMS) from production of ions to detection and analysis.

The time of flight of the ions can be determined using the following equation:

Equation 3

$$t^2 = \frac{m}{z}\left(\frac{L^2}{2eV_s}\right)$$

Above, the relationship between the flight tube and the ions respective mass is described, where:

t is the time of the ions in the flight tube;

m/z is the mass to charge ratio of the species;

L is the defined length of the flight tube;

V_s is the velocity of the ions through the free field

This equation rearranged (Equation 4) allows for the calculation of the *m/z* values of the ions, hence production of spectra.

Equation 4

$$(m/z)^{1/2} = \left(\frac{\sqrt{2eV_S}}{L}\right) t$$

1.6.4. SIMS Sample Preparation

Sample preparation methods must be considered when obtaining SIMS images. Due to the high vacuum, without appropriate fixing methods, mobile species could migrate causing biological differences to the sample.[62] As this technique is focused on analysing the top most monolayers, any water molecules situated on the surface of the sample will also be a major source of interference. As a result, if the sample is not fixed appropriately, this will cause cell components to relocate during the drying process and therefore limit the chemical information that is specific to the cell.[63] Careful sample fixation is necessary before qualitative analysis as it must be ensured that the preparation method preserves the native structural and chemical integrity of the species as far as possible.[64] Ideally, sample preparation should leave the sample in its native state whilst also satisfying any instrumentation requirements. However, these problems associated with sample preparation are entirely case reliant. No single method can be used globally as the optimal method is sample and instrument dependent.[65] A number of different methods are published which allow the reader to tailor these specifically to the samples desired. These include; freeze drying, chemical fixation[66] and frozen hydrated[67] methods.[65] Although no single technique has been marked as the golden standard for SIMS imaging, these methods each come with their own advantages and disadvantages which can be exploited depending on the biological question.

1.6.5. Ambient ionisation techniques

Ambient ionisation is a relatively new range of approaches in MS involving the analysis of samples in their native state with minimum to no sample preparation.[49,68] Ionisation of the sample occurs at ambient temperatures and pressures, external to the mass analyser, therefore only the subsequent ions are introduced to the mass spectrometer. As there is no need for additional preparation steps, the overall sample workflow is reduced as well as the possibility for any unwanted chemical modifications to the sample.[69]

1.6.5.1. Desorption electrospray ionisation

Ambient ionisation methods have shown great potential in the area of MSI. This is due to the ability to acquire molecularly specific images without the need for additional modification such as staining, matrix application, or dehydration as well as high chemical specificity and the relative ease of application. Desorption electrospray ionisation (DESI) is one of the most thoroughly explored ambient MSI techniques.[49]

DESI ionisation combines electrospray technology with desorption techniques (Figure 1.9). This is achieved *via* a stream of charged droplets and solvent ions, generated by electrospray ionisation (ESI), being directed onto a surface of a biological sample. This fast nebulising gas jet impacts on the sample surface causing desorption of analytes into secondary gas phase droplets. These are generated in the open air before being drawn into the inlet of the mass spectrometer.[49] DESI-MS imaging has the potential to be implemented in clinical situations as an imaging technique as it allows for direct mapping of lipids, and other potentially diagnostic biological molecules, from thin histological sections of tissue.[71]

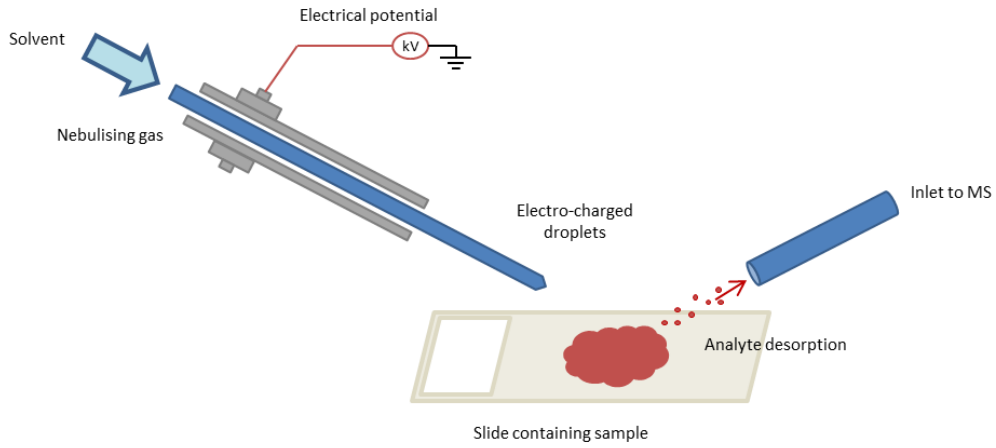

Figure 1.9: A schematic diagram showing the process of ionisation using desorption electrospray ionisation (DESI).

The major advantage of this technique is that desorption occurs at ambient pressure and temperature, therefore little to no sample preparation is required, however, the detector and mass spectrometer will still need to be kept under vacuum. The ions formed are transported to the detector *via* a heated ion transfer tube. This ensures a large pressure differential whilst ensuring little neutralisation of the ions. DESI does not have the high spatial capability as observed with SIMS ion beams or even MALDI lasers, with laser spot sizes typically observed around 15-150 µm.[72] Typical spatial resolution observed for DESI experiments is witnessed in the 100 µm range. However, if operating conditions have been optimised then this value can be seen as low as 20 µm.[65] Despite this, DESI-MS can be considered complementary to the other MS methods as it avoids constraints of the vacuum.

1.6.6. Optimisation

For DESI, optimisation of experimental parameters is key in ensuring the greatest sensitivity is achieved and thereby yielding high quality MS images. Firstly, the solvent system needs to be considered as different chemical information can be acquired by changing the choice of solvent. It has been shown that using solvents such as DMF or ACN, tends to enhance

signals of low molecular weight compounds.[73] However, one of the most important considerations to factor into solvent choice is how the it changes the morphology of the sample. For most biological applications, a mixture of 98:2 MeOH:H_2O is the most morphologically friendly in extracting lipids without causing any significant changes to the sample on the microscopic scale.[49] As a result, for the purposes of any further experimentation, the use of 98:2 MeOH:H_2O solvent will be employed. Further optimisation includes adjusting the geometrical parameters of the ion source, comprising of the nebulisation capillary angle, distance of the emitter from the surface and the position of the inlet to the mass spectrometer. Other factors, including gas pressure and solvent flow are also important to consider during optimisation. Before experimentation, the mass spectrometer must be optimised for the sample type to ensure the greatest sensitivity and hence the highest quality images.[73]

1.6.7. Instrumentation

The instrument used for all ambient ionisation for this study is the Waters Xevo G2-XS quadrupole time of flight (QToF) mass spectrometer (Figure 1.10). The presence of the quadrupole allows for increased mass resolution as well as the ability to acquire tandem mass spectrometry experiments (MS/MS). The quadrupole can be set to a particular *m/z* value, in which, during the experiment, this species will be isolated and taken to a collision cell for fragmentation.[74] This method is particularly useful for identification of lipids, as these species tend to fragment in specific patterns. Typically, MS/MS experiments will reveal the loss of the lipid head group or fatty acyl chain, allowing for a more exact identification of the *m/z* value. [75]

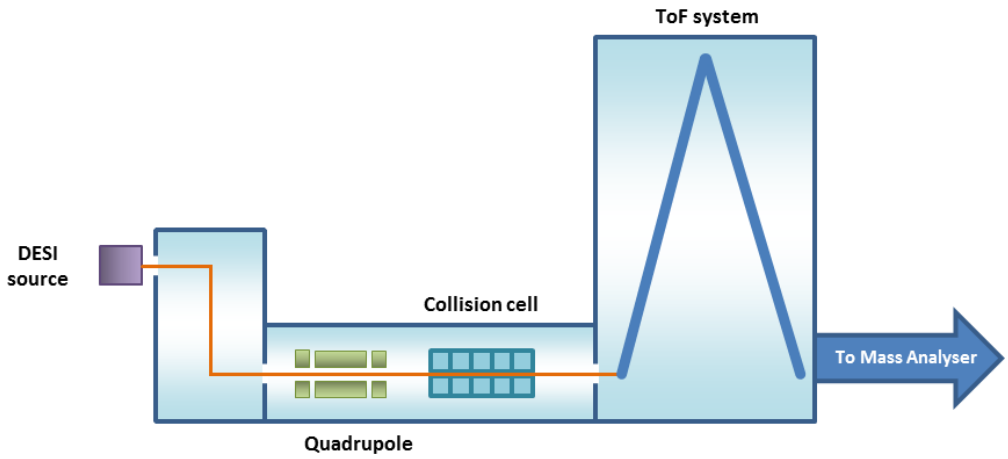

Figure 1.10: A schematic of the Xevo G2-XS QToF system, highlighting the ion path through the instrument (orange) and the key components of the mass spectrometer.

1.6.8. 3D imaging

DESI has the capability to produce 3D images based on a series of 2D images. If the tissue is sectioned with the same distance as spatial resolution you can create a 3D voxel from the acquired 2D data. This has many exciting prospects in the field of medical and clinical diagnosis as it can allow for the determination of heterogeneity within samples that previously may not have been detected. There is currently very little in the literature about 3D DESI imaging highlighting the potential for novel and ground breaking work.[76,77]

1.7. Rapid Evaporative Ionisation Mass Spectrometry

Rapid evaporative ionisation mass spectrometry (REIMS) is another example of an ambient ionisation method. It allows for rapid discrimination of biological tissues and can differentiate samples based on their lipidomic fingerprint. No sample preparation methods are required and therefore REIMS can be used to sample live cell colonies directly.[78] This holds a major advantage, as vacuum MSI methods cannot image live cell cultures. REIMS rapidly heats the sample by applying a radiofrequency electrical current to the biomass,

which henceforth forms a vapour. This vapour consists of gaseous ion forms of lipids and metabolites which are then extracted towards the mass detector for analysis.[79]

1.7.1. iKnife

One of the major applications in which this technique has been developed for, is for *in situ* analysis of tumour tissue, intraoperatively.[80] Many current studies using REIMS have been working on the development of a database of a number of different oncological samples to allow for the detection of certain cancers in real time.[81] The iKnife is a hand held sampling device that is designed to replicate a surgical knife (Figure 1.11). As with the REIMS system, a high frequency electrical current is applied to the tissue *via* a diathermic process. This causes the biological tissue to cauterise producing 'smoke' as the tissue is cut. This 'smoke' contains ionised gas phase clusters which are taken to the mass spectrometer *via* PTFE tubing. Currently, the iKnife is most popular in the field of food and environmental sciences in detecting authenticity in food samples.[82] However, more recently, this application is being expanded to be used in a surgical environment, helping the surgeon to discriminate between healthy and diseased tissue in real time.[83]

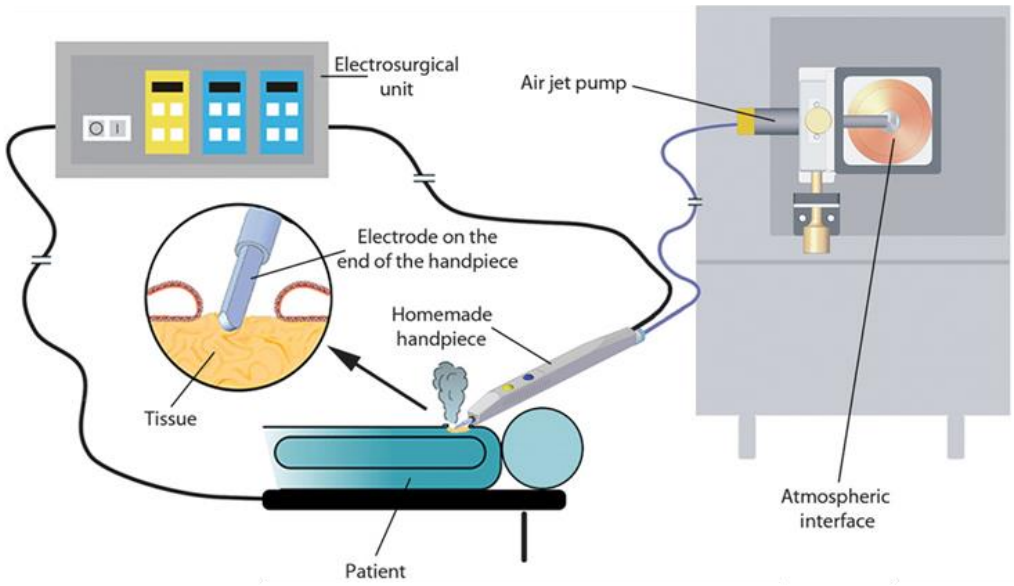

Figure 1.11: A schematic of the iKnife design. Shown is the how electrosurgical knife interacts with the tissue to produce a smoke plume followed by the path of the ions to the mass spectrometer.[80]

1.7.2. LASER REIMS

As this technique has progressed, so have the sample types that have been explored *via* REIMS. For some applications, such as cell culture samples, the large handheld forceps were discovered to be too bulky for analysis, therefore reducing the overall reproducibility of the data. Therefore, a more automatic LASER based system was developed to overcome this issue [85]. This will be discussed in more detail in later chapters.

1.8. Samples

1.8.1. Tissue Samples

Tissue samples are a highly valuable resource for a number of analytical applications. They allow for research into diseases on samples that best represent a human model. There are a large number of tissue banks that store collections of tissue samples which are available to researchers and biotech companies alike, from brain tissue to skin samples.[86] However,

these samples are typically fixed to ensure, biologically, they remain intact. In terms of histology and preservation of tissue, it is recommended that tissue samples undergo formalin fixation and paraffin embedding (FFPE).[87] This procedure prevents degradation of the sample and migration of metabolites. However, this method makes MS analysis very difficult as the paraffin suppresses lipid signal. Therefore, in order to analyse the sample a washing step must be implemented. However, most protocols recommend washing with an organic solvent such as hexane. Using this will strip the sample of any lipid species present on the surface of the tissue, not only changing the general composition of analytes, but also making lipidomic analysis particularly difficult. Therefore, optimisation of this washing step is crucial, in order to find a solvent that will allow for the removal of paraffin, without altering the chemical makeup of the sample.

1.8.2. Cell Culture

One of the main advantages of mass spectral imaging is the capability of single cell imaging. Using MSI approaches, this enables the detection of metabolites as a function of their spatial distribution across the surface of a cell. It is a powerful technique that can be used to map the distribution of endogenous bio-molecular species down to subcellular resolution. Currently, one of the main platforms used for single cell imaging is SIMS due to its high spatial resolution. However, more recently, ambient techniques such as DESI and REIMS have been used in the analysis of cell cultures. One major advantage of single cell imaging is its ability to elucidate intercellular heterogeneities by connecting chemical distributions with the overall cell morphology.[88] In general, it is considered that cell culture methods are the easiest in terms of acquiring samples. This is because there are a large number of stocks worldwide for a range of cells, allowing for a number of human and animal models alike, to be replicated. However, it is thought that they are a simplified

model of a number of diseases, and therefore are not fully comparable to *in-vivo* states. Nevertheless, using these models can allow for better characterised and more controlled analysis before moving onto spheroid cultures or tissue samples, which will provide much more information that can be compared to human tissues.

1.9. Data Analysis

Mass spectrometry imaging experiments produce large quantities of data, containing thousands of spectra, and therefore potential *m/z* species and as such, MSI datasets contain a large number of variables. As a result, data analysis methods that reduce the dimensionality of the data sets are vital to handle such large quantities of complex data. Multivariate analysis techniques (MVA) have become common place for the analysis of MSI datasets.[89] MVA allows for both data analysis and classification to be undertaken by the reduction of dimensionality of the data and as a result, allow comparisons to be made between the corresponding data sets. This therefore, makes MVA essential for the overall MSI analysis workflow.[90]

Principal component analysis (PCA) is the most widely used MVA analysis type for imaging data, due to its ease of use and versatility. The mass spectrometry dataset is broken down into a number of principal components, reducing the dimensionality of the data into more manageable principal components. Depending on whether the analysis is supervised or unsupervised, the *m/z* species or samples will be grouped against each other along these linear principal components to show how closely they are related to one another. A principal component (PC) is a linear expression of the original variables and each PC will account for an amount of the data variance that they can explain. Each data point in a PCA plot is awarded a loading and score which represents the contribution this variable makes to the PC and how much of the PC there is in the variable respectively.[91] The results in this

work are visualised as 2D plots that highlight the weighting of each variable across two principal components.

Another useful MVA technique that allows for the reduction of dimensionality of the data is clustering techniques. Cluster methods such as k-means clustering are particularly useful for uncovering separations and groups from within imaging dataset. K-means clustering is often used for image segmentation, rather than looking at individual samples do to the ability to separate the components of the image in space.[92] K-means clustering will find the largest differences and separate the dataset into groups, a process that can be repeated multiple times to provide distinct groups within the mass spectrometry images. Further analysis of these individual groups can reveal chemical species and *m/z* values that differ between the groups, and as such is useful in biomarker analysis.[93] As a result, these data analysis methods will be utilised to allow for the reduction of dimensionality of the data and thus, the most relevant data to be extracted.

1.10. References

(1) Cancer Research Society - CRS - Cancer Research Society https://www.crs-src.ca/ (accessed Jan 9, 2017).

(2) Rucci, N.; Angelucci, A. Prostate Cancer and Bone: The Elective Affinities. *BioMed Res. Int.* **2014**, *2014*. https://doi.org/10.1155/2014/167035.

(3) Hall, J. E.; Guyton, A. C. *Guyton and Hall Textbook of Medical Physiology*, 12th ed.; Saunders/Elsevier: Philadelphia, Pa, 2011.

(4) McNeal, J. E. M. D. Normal Histology of the Prostate. *J. Surg. Pathol.* **1988**, *12* (8), 619–633.

(5) Fine, S. W.; Reuter, V. E. Anatomy of the Prostate Revisited: Implications for Prostate Biopsy and Zonal Origins of Prostate Cancer. *Histopathology* **2012**, *60* (1), 142–152. https://doi.org/10.1111/j.1365-2559.2011.04004.x.

(6) Tai, S.; Sun, Y.; Squires, J. M.; Zhang, H.; Oh, W. K.; Liang, C.-Z.; Huang, J. PC3 Is a Cell Line Characteristic of Prostatic Small Cell Carcinoma. *The Prostate* **2011**, *71* (15), 1668–1679. https://doi.org/10.1002/pros.21383.

(7) Abate-Shen, C.; Shen, M. M. Molecular Genetics of Prostate Cancer. *Genes Dev.* **2000**, *14* (19), 2410–2434. https://doi.org/10.1101/gad.819500.

(8) Kristiansen, G.; Epstein, J. I. Immunohistochemistry in Prostate Pathology. *DAKO Available Online Httpwww Dako Comdeihc-Prostatepathology Pdf* **2014**.

(9) Chu, P. G.; Weiss, L. M. Expression of Cytokeratin 5/6 in Epithelial Neoplasms: An Immunohistochemical Study of 509 Cases. *Mod. Pathol. Off. J. U. S. Can. Acad. Pathol. Inc* **2002**, *15* (1), 6–10. https://doi.org/10.1038/modpathol.3880483.

(10) Oesterling, J. E.; Jacobsen, S. J.; Chute, C. G.; Guess, H. A.; Girman, C. J.; Panser, L. A.; Lieber, M. M. Serum Prostate-Specific Antigen in a Community-Based Population of Healthy Men: Establishment of Age-Specific Reference Ranges. *JAMA* **1993**, *270* (7), 860–864. https://doi.org/10.1001/jama.1993.03510070082041.

(11) Signoretti, S.; Loda, M. Defining Cell Lineages in the Prostate Epithelium. *Cell Cycle Georget. Tex* **2006**, *5* (2), 138–141. https://doi.org/10.4161/cc.5.2.2340.

(12) Research OMICS Group | The Science Search Engine http://research.omicsgroup.org/ (accessed Jan 9, 2017).

(13) Tindall, D.; Mohler, J. *Androgen Action in Prostate Cancer*; Springer Science & Business Media, 2009.

(14) Russell, P. J.; Kingsley, E. A. Human Prostate Cancer Cell Lines. *Prostate Cancer Methods Protoc.* **2003**, 21–39.

(15) McNeal, J. E. M. D.; Redwine, E. A. B. S.; Freiha, F. S. M. D.; Stamey, T. A. M. D. Zonal Distribution of Prostatic Adenocarcinoma: Correlation with Histologic Pattern and Direction of Spread. *J. Surg. Pathol.* **1988**, *12* (12), 897–906.

(16) McDougal, W. S.; Wein, A. J.; Kavoussi, L. R.; Novick, A. C.; Partin, A. W.; Peters, C. A.; Ramchandani, P. *Campbell-Walsh Urology 10th Edition Review*; Elsevier Health Sciences, 2011.

(17) Brawer, M. K. Prostatic Intraepithelial Neoplasia: An Overview. *Rev. Urol.* **2005**, *7* (Suppl 3), S11–S18.

(18) Montironi, R.; Mazzucchelli, R.; Algaba, F.; Lopez-Beltran, A. Morphological Identification of the Patterns of Prostatic Intraepithelial Neoplasia and Their Importance. *J. Clin. Pathol.* **2000**, *53* (9), 655–665. https://doi.org/10.1136/jcp.53.9.655.

(19) Bostwick, D. G.; Qian, J. High-Grade Prostatic Intraepithelial Neoplasia. *Mod. Pathol.* **2004**, *17* (3), 360–379. https://doi.org/10.1038/modpathol.3800053.

(20) Horoszewicz, J. S.; Leong, S. S.; Kawinski, E.; Karr, J. P.; Rosenthal, H.; Chu, T. M.; Mirand, E. A.; Murphy, G. P. LNCaP Model of Human Prostatic Carcinoma. *Cancer Res.* **1983**, *43* (4), 1809–1818.

(21) van Steenbrugge, G. J.; van Uffelen, C. J.; Bolt, J.; Schröder, F. H. The Human Prostatic Cancer Cell Line LNCaP and Its Derived Sublines: An in Vitro Model for the Study of Androgen Sensitivity. *J. Steroid Biochem. Mol. Biol.* **1991**, *40* (1–3), 207–214.

(22) Schuurmans, A. L.; Bolt, J.; Veldscholte, J.; Mulder, E. Regulation of Growth of LNCaP Human Prostate Tumor Cells by Growth Factors and Steroid Hormones. *J. Steroid Biochem. Mol. Biol.* **1991**, *40* (1–3), 193–197.

(23) MuraliKrishna, P. S.; Gondi, C. S.; Lakka, S. S.; Julta, A.; Estes, N.; Gujrati, M.; Rao, J. S. RNA Interference-Directed Knockdown of Urokinase Plasminogen Activator and Urokinase Plasminogen Activator Receptor Inhibits Prostate Cancer Cell Invasion, Survival and Tumorigenicity In Vivo. *J. Biol. Chem.* **2005**, *280* (43), 36529–36540. https://doi.org/10.1074/jbc.M503111200.

(24) Cussenot, O.; Berthon, P.; Berger, R.; Mowszowicz, I.; Faille, A.; Hojman, F.; Teillac, P.; Le Duc, A.; Calvo, F. Immortilization of Human Adult Normal Prostatic Epithelial Cell by Liposomes Containing Large T-SV40 Gene. *J. Urol.* **1991**, *143*, 881–886.

(25) Lilja, H.; Oldbring, J.; Rannevik, G.; Laurell, C. B. Seminal Vesicle-Secreted Proteins and Their Reactions during Gelation and Liquefaction of Human Semen. *J. Clin. Invest.* **1987**, *80* (2), 281–285.

(26) Flatley, B.; Malone, P.; Cramer, R. MALDI Mass Spectrometry in Prostate Cancer Biomarker Discovery. *Biochim. Biophys. Acta* **2014**, *1844* (5), 940–949. https://doi.org/10.1016/j.bbapap.2013.06.015.

(27) Heidenreich, A.; Bastian, P. J.; Bellmunt, J.; Bolla, M.; Joniau, S.; van der Kwast, T.; Mason, M.; Matveev, V.; Wiegel, T.; Zattoni, F.; Mottet, N. EAU Guidelines on Prostate Cancer. Part 1: Screening, Diagnosis, and Local Treatment with Curative Intent—Update 2013. *Eur. Urol.* **2014**, *65* (1), 124–137. https://doi.org/10.1016/j.eururo.2013.09.046.

(28) Duraiyan, J.; Govindarajan, R.; Kaliyappan, K.; Palanisamy, M. Applications of Immunohistochemistry. *J. Pharm. Bioallied Sci.* **2012**, *4* (Suppl 2), S307–S309. https://doi.org/10.4103/0975-7406.100281.

(29) Gleason, Donald. F. Histologic Grading of Prostate Cancer: A Perspective. *Hum. Pathol.* **1992**, *23* (3), 273–279.

(30) Gordetsky, J.; Epstein, J. Grading of Prostatic Adenocarcinoma: Current State and Prognostic Implications. *Diagn. Pathol.* **2016**, *11*. https://doi.org/10.1186/s13000-016-0478-2.

(31) Gleason, Donald. F.; Mellinger, G. Prediction of Prognosis for Prostatic Adenocarcinoma by Combined Histological Grading and Clinical Staging. *J. Urol.* **1974**, *111* (1), 58–64.

(32) Humphrey, P. A. Gleason Grading and Prognostic Factors in Carcinoma of the Prostate. *Mod. Pathol.* **2004**, *17* (3), 292–306. https://doi.org/10.1038/modpathol.3800054.

(33) Leng, E.; Henriksen, J. C.; Rizzardi, A. E.; Jin, J.; Nam, J. W.; Brassuer, B. M.; Johnson, A. D.; Reder, N. P.; Koopmeiners, J. S.; Schmechel, S. C.; Metzger, G. J. Signature Maps for Automatic Identification of Prostate Cancer from Colorimetric Analysis of H&E- and IHC-Stained Histopathological Specimens. *Sci. Rep.* **2019**, *9* (1), 1–12. https://doi.org/10.1038/s41598-019-43486-y.

(34) When Tissue Antigens and Antibodies Get Along: Revisiting the Technical Aspects of Immunohistochemistry—The Red, Brown, and Blue Technique - J. A. Ramos-Vara, M. A. Miller, 2014 https://journals.sagepub.com/doi/10.1177/0300985813505879 (accessed Jan 13, 2020).

(35) Quehenberger, O.; Armando, A. M.; Brown, A. H.; Milne, S. B.; Myers, D. S.; Merrill, A. H.; Bandyopadhyay, S.; Jones, K. N.; Kelly, S.; Shaner, R. L.; Sullards, C. M.; Wang, E.; Murphy, R. C.; Barkley, R. M.; Leiker, T. J.; Raetz, C. R. H.; Guan, Z.; Laird, G. M.; Six, D. A.; Russell, D. W.; McDonald, J. G.; Subramaniam, S.; Fahy, E.; Dennis, E. A. Lipidomics Reveals a Remarkable Diversity of Lipids in Human Plasma. *J. Lipid Res.* **2010**, *51* (11), 3299–3305. https://doi.org/10.1194/jlr.M009449.

(36) Wenk, M. R. The Emerging Field of Lipidomics. *Nat. Rev. Drug Discov.* **2005**, *4* (7), 594–610. https://doi.org/10.1038/nrd1776.

(37) LIPID | meaning in the Cambridge English Dictionary https://dictionary.cambridge.org/dictionary/english/lipid (accessed Jan 13, 2020).

(38) Fahy, E.; Cotter, D.; Sud, M.; Subramaniam, S. Lipid Classification, Structures and Tools. *Biochim. Biophys. Acta* **2011**, *1811* (11), 637–647. https://doi.org/10.1016/j.bbalip.2011.06.009.

(39) Butler, L. M.; Perone, Y.; Dehairs, J.; Lupien, L. E.; de Laat, V.; Talebi, A.; Loda, M.; Kinlaw, W. B.; Swinnen, J. V. Lipids and Cancer: Emerging Roles in Pathogenesis, Diagnosis and Therapeutic Intervention. *Adv. Drug Deliv. Rev.* **2020**. https://doi.org/10.1016/j.addr.2020.07.013.

(40) Kuhajda, F. P.; Jenner, K.; Wood, F. D.; Hennigar, R. A.; Jacobs, L. B.; Dick, J. D.; Pasternack, G. R. Fatty Acid Synthesis: A Potential Selective Target for Antineoplastic Therapy. *Proc. Natl. Acad. Sci. U. S. A.* **1994**, *91* (14), 6379–6383.

(41) Baenke, F.; Peck, B.; Miess, H.; Schulze, A. Hooked on Fat: The Role of Lipid Synthesis in Cancer Metabolism and Tumour Development. *Dis. Model. Mech.* **2013**, *6* (6), 1353–1363. https://doi.org/10.1242/dmm.011338.

(42) Chen, M.; Huang, J. The Expanded Role of Fatty Acid Metabolism in Cancer: New Aspects and Targets. *Precis. Clin. Med.* **2019**, *2* (3), 183–191. https://doi.org/10.1093/pcmedi/pbz017.

(43) Sorvina, A.; Bader, C. A.; Caporale, C.; Carter, E. A.; Johnson, I. R. D.; Parkinson-Lawrence, E. J.; Simpson, P. V.; Wright, P. J.; Stagni, S.; Lay, P. A.; Massi, M.; Brooks, D. A.; Plush, S. E. Lipid Profiles of Prostate Cancer Cells. *Oncotarget* **2018**, *9* (85), 35541–35552. https://doi.org/10.18632/oncotarget.26222.

(44) Denbigh, J. L.; Lockyer, N. P. ToF-SIMS as a Tool for Profiling Lipids in Cancer and Other Diseases. *Mater. Sci. Technol.* **2015**, *31* (2), 137–147. https://doi.org/10.1179/1743284714Y.0000000648.

(45) Sharpening the focus on cancer tumours | Elsevier Enhanced Reader https://reader.elsevier.com/reader/sd/pii/S1359644619301886?token=7F8F493259CAD15969CEC7DFDC0E7926395179F46B1E0CF3314D40A248AD4BA2BCD2DC33CDDE5008CA95AF6E869D06BC (accessed Sep 22, 2020). https://doi.org/10.1016/j.drudis.2019.07.003.

(46) Chaurand, P.; Schwartz, S. A.; Reyzer, M. L.; Caprioli, R. M. Imaging Mass Spectrometry: Principles and Potentials. *Toxicol. Pathol.* **2005**, *33* (1), 92–101. https://doi.org/10.1080/01926230590881862.

(47) Beynon, J., H.; Morgan, R., P. The Development of Mass Spectroscopy: An Historical Account. *Int. J. Mass Spectrom. Ion Phys.* **1977**, *27*, 1–30.

(48) Wiley: Introduction to Mass Spectrometry: Instrumentation, Applications, and Strategies for Data Interpretation, 4th Edition - J. Throck Watson, O. David Sparkman http://www.wiley.com/WileyCDA/WileyTitle/productCd-0470516348.html (accessed Jan 8, 2017).

(49) Wu, C.; Dill, A. L.; Eberlin, L. S.; Cooks, R. G.; Ifa, D. R. Mass Spectrometry Imaging under Ambient Conditions. *Mass Spectrom. Rev.* **2013**, *32* (3), 218–243. https://doi.org/10.1002/mas.21360.

(50) Fearn, S. Characterisation of Biological Material with ToF-SIMS: A Review. *Mater. Sci. Technol.* **2015**, *31* (2), 148–161. https://doi.org/10.1179/1743284714Y.0000000668.

(51) Paruch, R. J.; Garrison, B. J.; Postawa, Z. Computed Molecular Depth Profile for C_{60} Bombardment of a Molecular Solid. *Anal. Chem.* **2013**, *85* (23), 11628–11633. https://doi.org/10.1021/ac403035a.

(52) Benninghoven, A. Surface Investigation of Solids by the Statical Method of Secondary Ion Mass Spectroscopy (SIMS). *Surf. Sci.* **1973**, *35*, 427–457.

(53) Delcorte, A.; Segda, B. G.; Garrison, B. J.; Bertrand, P. Inferring Ejection Distances and a Surface Energy Profile in KeV Particle Bombardment Experiments. *Nucl. Instrum. Methods Phys. Res. Sect. B Beam Interact. Mater. At.* **2000**, *171* (3), 277–290. https://doi.org/10.1016/S0168-583X(00)00263-9.

(54) Brunelle, A.; Touboul, D.; Laprévote, O. Biological Tissue Imaging with Time-of-Flight Secondary Ion Mass Spectrometry and Cluster Ion Sources. *J. Mass Spectrom.* **2005**, *40* (8), 985–999. https://doi.org/10.1002/jms.902.

(55) Fletcher, J. S.; Henderson, A.; Biddulph, G. X.; Vaidyanathan, S.; Lockyer, N. P.; Vickerman, J. C. Uncovering New Challenges in Bio-Analysis with ToF-SIMS. *Appl. Surf. Sci.* **2008**, *255* (4), 1264–1270. https://doi.org/10.1016/j.apsusc.2008.05.253.

(56) Matsuo, J.; Ninomiya, S.; Yamada, H.; Ichiki, K.; Wakamatsu, Y.; Hada, M.; Seki, T.; Aoki, T. SIMS with Highly Excited Primary Beams for Molecular Depth Profiling and Imaging of Organic and Biological Materials. *Surf. Interface Anal.* **2010**, *42* (10–11), 1612–1615. https://doi.org/10.1002/sia.3585.

(57) Enhanced Ion Yields Using High Energy Water Cluster Beams for Secondary Ion Mass Spectrometry Analysis and Imaging | Analytical Chemistry https://pubs.acs.org/doi/10.1021/acs.analchem.9b01390 (accessed Jan 11, 2021).

(58) Fletcher, J. S.; Rabbani, S.; Henderson, A.; Blenkinsopp, P.; Thompson, S. P.; Lockyer, N. P.; Vickerman, J. C. A New Dynamic in Mass Spectral Imaging of Single Biological Cells. *Anal. Chem.* **2008**, *80* (23), 9058–9064. https://doi.org/10.1021/ac8015278.

(59) Lanni, E. J.; Rubakhin, S. S.; Sweedler, J. V. Mass Spectrometry Imaging and Profiling of Single Cells. *J. Proteomics* **2012**, *75* (16), 5036–5051. https://doi.org/10.1016/j.jprot.2012.03.017.

(60) Hill, R.; Blenkinsopp, P.; Thompson, S.; Vickerman, J.; Fletcher, J. S. A New Time-of-Flight SIMS Instrument for 3D Imaging and Analysis. *Surf. Interface Anal.* **2011**, *43* (1–2), 506–509. https://doi.org/10.1002/sia.3562.

(61) Wiley, W. C.; McLaren, I. H. Time-of-Flight Mass Spectrometer with Improved Resolution. *Rev. Sci. Instrum.* **1955**, *26* (12), 1150–1157. https://doi.org/10.1063/1.1715212.

(62) Passarelli, M. K.; Winograd, N. Lipid Imaging with Time-of-Flight Secondary Ion Mass Spectrometry (ToF-SIMS). *Biochim. Biophys. Acta BBA - Mol. Cell Biol. Lipids* **2011**, *1811* (11), 976–990. https://doi.org/10.1016/j.bbalip.2011.05.007.

(63) Colliver, T. L.; Brummel, C. L.; Pacholski, M. L.; Swanek, F. D.; Ewing, A. G.; Winograd, N. Atomic and Molecular Imaging at the Single-Cell Level with TOF-SIMS. *Anal. Chem.* **1997**, *69* (13), 2225–2231. https://doi.org/10.1021/ac9701748.

(64) Chandra, S.; Morrison, G. H. Sample Preparation of Animal Tissues and Cell Cultures for Secondary Ion Mass Spectrometry (SIMS) Microscopy. *Biol. Cell* **1992**, *74* (1), 31–42.

(65) Chandra, S. Challenges of Biological Sample Preparation for SIMS Imaging of Elements and Molecules at Subcellular Resolution. *Appl. Surf. Sci.* **2008**, *255* (4), 1273–1284. https://doi.org/10.1016/j.apsusc.2008.05.073.

(66) Malm, J.; Giannaras, D.; Riehle, M. O.; Gadegaard, N.; Sjövall, P. Fixation and Drying Protocols for the Preparation of Cell Samples for Time-of-Flight Secondary Ion Mass

Spectrometry Analysis. *Anal. Chem.* **2009**, *81* (17), 7197–7205. https://doi.org/10.1021/ac900636v.

(67) Piwowar, A. M.; Keskin, S.; Delgado, M. O.; Shen, K.; Hue, J. J.; Lanekoff, I.; Ewing, A. G.; Winograd, N. C60-ToF SIMS Imaging of Frozen Hydrated HeLa Cells. *Surf. Interface Anal. SIA* **2013**, *45* (1), 302–304. https://doi.org/10.1002/sia.4882.

(68) Weston, D. J. Ambient Ionization Mass Spectrometry: Current Understanding of Mechanistic Theory; Analytical Performance and Application Areas. *The Analyst* **2010**, *135* (4), 661. https://doi.org/10.1039/b925579f.

(69) Eugenia Monge, M.; M. Fernández, F. Chapter 1 An Introduction to Ambient Ionization Mass Spectrometry. **2014**, 1–22. https://doi.org/10.1039/9781782628026-00001.

(70) Meetani, M. A.; Shin, Y.-S.; Zhang, S.; Mayer, R.; Basile, F. Desorption Electrospray Ionization Mass Spectrometry of Intact Bacteria. *J. Mass Spectrom. JMS* **2007**, *42* (9), 1186–1193. https://doi.org/10.1002/jms.1250.

(71) Wiseman, J. M.; Ifa, D. R.; Song, Q.; Cooks, R. G. Tissue Imaging at Atmospheric Pressure Using Desorption Electrospray Ionization (DESI) Mass Spectrometry. *Angew. Chem. Int. Ed.* **2006**, *45* (43), 7188–7192. https://doi.org/10.1002/anie.200602449.

(72) Römpp, A.; Spengler, B. Mass Spectrometry Imaging with High Resolution in Mass and Space. *Histochem. Cell Biol.* **2013**, *139* (6), 759–783. https://doi.org/10.1007/s00418-013-1097-6.

(73) Bodzon-Kulakowska, A.; Drabik, A.; Ner, J.; Kotlinska, J. H.; Suder, P. Desorption Electrospray Ionisation (DESI) for Beginners--How to Adjust Settings for Tissue Imaging. *Rapid Commun. Mass Spectrom. RCM* **2014**, *28* (1), 1–9. https://doi.org/10.1002/rcm.6755.

(74) Yost, R. A.; Boyd, R. K. [7] Tandem Mass Spectrometry: Quadrupole and Hybrid Instruments. *Methods Enzymol.* **1990**, *193*, 154–200. https://doi.org/10.1016/0076-6879(90)93415-H.

(75) Isaac, G. Electrospray Ionization Tandem Mass Spectrometry (ESI-MS/MS)-Based Shotgun Lipidomics. In *Metabolic Profiling*; Metz, T. O., Ed.; Methods in Molecular Biology; Humana Press, 2011; pp 259–275. https://doi.org/10.1007/978-1-61737-985-7_16.

(76) Oetjen, J.; Veselkov, K.; Watrous, J.; McKenzie, J. S.; Becker, M.; Hauberg-Lotte, L.; Kobarg, J. H.; Strittmatter, N.; Mróz, A. K.; Hoffmann, F.; Trede, D.; Palmer, A.;

Schiffler, S.; Steinhorst, K.; Aichler, M.; Goldin, R.; Guntinas-Lichius, O.; von Eggeling, F.; Thiele, H.; Maedler, K.; Walch, A.; Maass, P.; Dorrestein, P. C.; Takats, Z.; Alexandrov, T. Benchmark Datasets for 3D MALDI- and DESI-Imaging Mass Spectrometry. *GigaScience* **2015**, *4*. https://doi.org/10.1186/s13742-015-0059-4.

(77) Inglese, P.; S. McKenzie, J.; Mroz, A.; Kinross, J.; Veselkov, K.; Holmes, E.; Takats, Z.; K. Nicholson, J.; C. Glen, R. Deep Learning and 3D-DESI Imaging Reveal the Hidden Metabolic Heterogeneity of Cancer. *Chem. Sci.* **2017**. https://doi.org/10.1039/C6SC03738K.

(78) Yan, C.; Parmeggiani, F.; Jones, E. A.; Claude, E.; Hussain, S. A.; Turner, N. J.; Flitsch, S. L.; Barran, P. E. Real-Time Screening of Biocatalysts in Live Bacterial Colonies. *J. Am. Chem. Soc.* **2017**, *139* (4), 1408–1411. https://doi.org/10.1021/jacs.6b12165.

(79) Bolt, F.; Cameron, S. J. S.; Karancsi, T.; Simon, D.; Schaffer, R.; Rickards, T.; Hardiman, K.; Burke, A.; Bodai, Z.; Perdones-Montero, A.; Rebec, M.; Balog, J.; Takats, Z. Automated High-Throughput Identification and Characterization of Clinically Important Bacteria and Fungi Using Rapid Evaporative Ionization Mass Spectrometry. *Anal. Chem.* **2016**, *88* (19), 9419–9426. https://doi.org/10.1021/acs.analchem.6b01016.

(80) Balog, J.; Sasi-Szabó, L.; Kinross, J.; Lewis, M. R.; Muirhead, L. J.; Veselkov, K.; Mirnezami, R.; Dezs\Ho, B.; Damjanovich, L.; Darzi, A.; others. Intraoperative Tissue Identification Using Rapid Evaporative Ionization Mass Spectrometry. *Sci. Transl. Med.* **2013**, *5* (194), 194ra93-194ra93.

(81) Genangeli, M.; Heeren, R. M. A.; Porta Siegel, T. Tissue Classification by Rapid Evaporative Ionization Mass Spectrometry (REIMS): Comparison between a Diathermic Knife and CO2 Laser Sampling on Classification Performance. *Anal. Bioanal. Chem.* **2019**, *411* (30), 7943–7955. https://doi.org/10.1007/s00216-019-02148-8.

(82) waters. REIMS Research System with iKnife Sampling brochure http://www.waters.com/waters/library.htm?cid=134846529&lid=134846772 (accessed Jan 9, 2017).

(83) Phelps, D. L.; Balog, J.; Gildea, L. F.; Bodai, Z.; Savage, A.; El-Bahrawy, M. A.; Speller, A. V.; Rosini, F.; Kudo, H.; McKenzie, J. S.; Brown, R.; Takáts, Z.; Ghaem-Maghami, S. The Surgical Intelligent Knife Distinguishes Normal, Borderline and Malignant Gynaecological Tissues Using Rapid Evaporative Ionisation Mass Spectrometry

(REIMS). *Br. J. Cancer* **2018**, *118* (10), 1349–1358. https://doi.org/10.1038/s41416-018-0048-3.

(84) Cameron, S. J. S.; Bodai, Z.; Temelkuran, B.; Perdones-Montero, A.; Bolt, F.; Burke, A.; Alexander-Hardiman, K.; Salzet, M.; Fournier, I.; Rebec, M.; Takáts, Z. Utilisation of Ambient Laser Desorption Ionisation Mass Spectrometry (ALDI-MS) Improves Lipid-Based Microbial Species Level Identification. *Sci. Rep.* **2019**, *9* (1), 1–8. https://doi.org/10.1038/s41598-019-39815-w.

(85) Jones, E. A.; Simon, D.; Karancsi, T.; Balog, J.; Pringle, S. D.; Takats, Z. Matrix Assisted Rapid Evaporative Ionization Mass Spectrometry. *Anal. Chem.* **2019**, *91* (15), 9784–9791. https://doi.org/10.1021/acs.analchem.9b01441.

(86) Andrews, L. B. Harnessing the Benefits of Biobanks. *J. Law. Med. Ethics* **2005**, *33* (1), 22–30.

(87) Canene-Adams, K. Preparation of Formalin-Fixed Paraffin-Embedded Tissue for Immunohistochemistry. *Methods Enzymol.* **2013**, *533*, 225–233. https://doi.org/10.1016/B978-0-12-420067-8.00015-5.

(88) Passarelli, M. K.; Ewing, A. G. Single-Cell Imaging Mass Spectrometry. *Curr. Opin. Chem. Biol.* **2013**, *17* (5). https://doi.org/10.1016/j.cbpa.2013.07.017.

(89) Muir, E. R.; Ndiour, I. J.; Goasduff, N. A.; Moffitt, R.; Liu, Y.; Sullards, M. C.; Merrill, A. H.; Chen, Y.; Wang, M. *Multivariate Analysis of Imaging Mass Spectrometry Data*; 2007; p 479. https://doi.org/10.1109/BIBE.2007.4375603.

(90) Tyler, B. Interpretation of TOF-SIMS Images: Multivariate and Univariate Approaches to Image de-Noising, Image Segmentation and Compound Identification. *Appl. Surf. Sci.* **2003**, *203–204*, 825–831. https://doi.org/10.1016/S0169-4332(02)00835-8.

(91) Ivosev, G.; Burton, L.; Bonner, R. Dimensionality Reduction and Visualization in Principal Component Analysis. *Anal. Chem.* **2008**, *80* (13), 4933–4944. https://doi.org/10.1021/ac800110w.

(92) Konicek, A. R.; Lefman, J.; Szakal, C. Automated Correlation and Classification of Secondary Ion Mass Spectrometry Images Using a K-Means Cluster Method. *The Analyst* **2012**, *137* (15), 3479. https://doi.org/10.1039/c2an16122b.

(93) Sarkari, S.; Kaddi, C. D.; Bennett, R. V.; Fernández, F. M.; Wang, M. D. Comparison of Clustering Pipelines for the Analysis of Mass Spectrometry Imaging Data. In *2014 36th Annual International Conference of the IEEE Engineering in Medicine and Biology Society*; 2014; pp 4771–4774. https://doi.org/10.1109/EMBC.2014.6944691.

Chapter 2

Distinguishing Between Aggression in Prostate Cancer Using Mass Spectrometry Imaging Techniques

2. Distinguishing Between Aggression in Prostate Cancer Using Mass Spectrometry Imaging Techniques

Danielle J McDougall[1], Irma Berrueta Razo[1], Emrys Jones[2], Alex Henderson[1], Claire Hart[3], Michael Brown[3], Kaye Williams[5], Adam McMahon[4], Nicholas Lockyer[1]

1. Department of Chemistry, Photon Science Institute, Alan Turing Building, University of Manchester, Manchester, UK
2. Waters, Department of Research and Development, Wilmslow, UK
3. Manchester Cancer Research Centre, University of Manchester, Manchester, UK
4. Division of Informatics, Imaging and Data Sciences, Wolfson Molecular Imaging Centre, University of Manchester, Manchester, UK
5. Division of Pharmacy and Optometry, Faculty of Biology, Medicine and Health, Stopford Building, University of Manchester, Manchester, UK

2.1. Abstract

Certain types of prostate cancer, such as prostatic adenocarcinoma, are slow growing and mild. However, a small percent of prostate cancer cases are extreme and come with a small life expectancy of 1 year. There is currently no distinct method in distinguishing between the indolent and aggressive form; and as a result the patient is treated as if it is the latter. This as a result comes with a series of side effects which decrease the patient's quality of life. This study successfully demonstrated the potential of using MSI methods, desorption electrospray ionisation (DESI) and time of flight secondary ion mass spectrometry (ToF-SIMS) to distinguish between biological regions of interest. A range of cell based models were used from cell monolayers to mixed cell pellet samples. The cell lines utilised in this study were PNT2-C2, LNCaP, and PC3. These were selected due to their differing aggression profiles. Using the lipid profile, the MSI techniques were able to distinguish between cell types. Alongside MSI, more conventional methods such immunohistochemical staining was used as a reference to support our findings.

2.2. Introduction

Prostate cancer (PCa) is the second highest cause of cancer related death in Western males and accounts for 1 in 5 new diagnoses of cancer, globally.[1] It typically occurs in males over 65 years of age and it has been shown that there are two primary categories of this cancer; that which is slow growing and typically don't concern a risk of death, and that which is fast growing and highly invasive.[2] Currently the primary detection method is monitoring the levels of PSA in the blood serum of the patient.[3] However, a rise in the level of this protein could also be indicative of benign prostate ailments. It is estimated that only 25% of those patients with an elevated PSA level of 3- 4 ng/ml had cancer associated with the prostate.[4]

One of the major problems with the detection and treatment of PCa is the difficulty in distinguishing indolent versus aggressive forms.[5] There is currently no distinct method in detecting the more aggressive form; and as a result the patient is often treated as if it is the malignant strain. The current treatment involves a full radical prostatectomy, which involves laparoscopic surgeries to remove the prostate and all surrounding tissue. Although the surgical procedure is considered relatively low risk, the major concern is following side-effect related problems,[6] which ultimately lead to a decrease in patient quality of life as well as aggressive treatment to those who do not need it.[7] Over the years cell lines have been derived from a number of prostate carcinomas and the consequential metastasis. These cells lines enable experimentation into the causes, treatment and potential prevention of prostate cancer. Extensive studies have been performed over the past few decades using these cell lines, providing a better understanding of the biology, aetiology, and pathology of the disease.[8] The current gold standard method in characterising and distinguishing maligancies within multi-cellular samples in a clinical setting is immunohistochemistry.[8] However this technique comes with a number of pitfalls, the

primary disadvantage being that it is all down to the individual pathologists' interpretation.[10]

Over the past decade MSI has been used extensively to profile and give *ex vivo* molecular analysis of cancer types.[11] One of the major advantages of MSI is the overall combination of mass spectrometry methods with the benefits of histological tissue analysis, in terms of defining spatial distribution of cellular compounds.[12] Due to the increasing popularity in using mass spectral imaging (MSI) techniques in clinical settings, this paper aims to explore the usefulness of these methods *via* the analysis of a number of prostate cancer cell lines, which differ in aggression, specifically observing the lipidomic fingerprint using mass spectrometry methods

2.3. Methods and Materials

2.3.1. Chemicals

All solvents and culture media, unless specified, were obtained from Sigma-Aldrich (Poole, UK). The solvents utilised were of HPLC grade or purer.

2.3.2. Cell Lines

2.3.2.1.LNCaP

The LNCaP cell line is one derived from culture explants from a needle biopsy from a patient suffering with lymph node adenocarcinoma of the prostate.[8] The LNCaP model grows readily *in vitro* and maintains malignant properties, therefore showing the potential usage of these cells, not only *in vitro,* but also as a potential for xenograft models they develop tumours *in vivo*.[8] LNCaP has been demonstrated to be androgen dependent and offers the possibility to study the involvement of hormone therapy.[13] LNCaP cells contain a

number of androgen receptors and the presence of these hormones directly affects the growth *in vitro.*[14] Overall, LNCaP has proven to be an ideal model for lymph node metastatic prostate cancer.[15]

2.3.2.2. PC3

PC-3 cells were derived from bone metastasis of a grade IV prostate cancer patient.[16] Unlike LNCaP, PC-3 lacks the androgen receptor, demonstrating that this cell line is androgen insensitive, as witnessed by more aggressive forms of PCa. The metastatic potential of PC-3 is much higher than that of LNCaP, which is considered to be moderately metastatic. PC-3 has been demonstrated as a more aggressive and invasive cancer type of prostatic small cell carcinoma.[17]

2.3.2.3. PNT2-C2

PNT2-C2 is used here as a biological control as it is a normal human epithelial cell line and primarily non-tumorigenic. This cell line was derived and immortalised in the early 1990s and holds many characteristics that are unique to healthy tissue.[18] This cell line naturally secretes PSA protein and expresses the androgen receptor, despite being androgen insensitive, as is typical for normal prostatic tissue. Therefore this cell line provides a good biological control for this study.

Table 2-1: Properties of the cell lines used for this study

Cell line	Metastatic potential	Androgen sensitivity	PSA secretion	Model
LNCaP	Mild	+	+	Prostatic Adenocarcinoma
PC3	Moderate	-	-	Small cell adenocarcinoma
PNT2	N/A	-	-	Normal tissue

2.3.3. Preparation of Cell pellet Samples

In order to fully explore the lipidomic differences observed within these cell lines, pellets were created, sectioned, and analysed. Pellets were primarily used as the sample type, due to their ease of access and their fast growth rates. The samples therefore allowed for a pseudo 3D tumour model comprised of these established cell lines. The gradient of aggression of the LNCaP, PC3, and PNT2-C2 cell lines offered the potential of understanding the metastatic nature of PCa.

2.3.3.1. Cell Culture

The LNCaP strain (LNCaP-ATCC) was cultured under optimum conditions as described on the ATCC product sheet[19] using Roswell park memorial institute (RPMI) media (Dulbecco's - Thermo Fischer) with additional growth factors. These included foetal calf serum (FCS) (10%, HyClone), HEPES buffer (Sigma Aldrich, 1M, 1%, pH 7.1), sodium pyruvate (1%, 100 mM) and 1% L-glutamine. For this cell line, it is important that the FCS is non-heat inactivated to allow for the cells to adhere to the flasks. For the PC3 and PNT2 cell line, RMPI media (Dulbecco's - Thermo Fischer) was also implemented. However, this media only needed the addition of FCS (10%Thermo Fischer). Each cell line was split approximately every 4 days which equated to 80% confluence. To allow for a higher cell count, the cells were passaged into a T175 flask, with approximately twice the surface area.

Once at 80% confluent, trypsin-EDTA solution (4 mL) was added to detach the cells from the flask and incubated for 5 minutes, to ensure all cells were removed. Following this, the corresponding media (6 mL) was added and the total volume was added to a 15 mL falcon tube. This was centrifuged (14,000 rpm, 5 minutes) to create a pellet. The media was decanted and each pellet was re-suspended in 1 mL of PBS (1x Sigma) and centrifuged again. This was repeated once more using PBS, and again using ammonium formate (150 mM, 1 mL). Finally, the supernatant was removed and the cells were re-suspended in PBS and centrifuged once more. The remaining PBS was aspirated, and the pellets were centrifuged for a final time. The addition of ammonium formate allowed for a final fixation step[20] prior to flash freezing. The pellets were then stored at -80˚C until sectioning. In order to explore the use of mass spectrometry imaging on samples with multiple cellular regions, mixed cell pellets were created by combining two or more of the cell lines. The mixtures created were; LNCaP + PC-3, PC-3 + PNT2-C2, PNT2-C2 + LNCaP, and LNCaP + PC-3 + PNT2-C2. These pellets were created the same way as described using a mix of 1:1 of each cell line.

2.3.3.2. Section Preparation

Prior to analysis, the cell pellets were sectioned and attached to appropriate substrates. In order to do this without disrupting or thawing the pellet, all further steps were performed within the -20 ˚C chamber of the cryostat (Leica CM3050 S). In order to easily remove the pellets from the falcon tube, a metal pencil sharpener was used to discard the plastic from the bottom of the tube. This dislodges the pellet, allowing it to be removed easily and quickly. Using carboxymethyl cellulose (CMC, 2%), the pellets were adhered to the cryostat chuck. Once the setup of the cryostat was optimum, and the pellet fully adhered, 14 µm thick sections were cut and attached to the appropriate substrate for analysis. For SIMS

analysis, the samples were mounted onto indium tin oxide (ITO) coated glass slides. The use of a conductive surface prevents charging occurring across the sample.

2.3.4. Immunofluorescence Staining

2.3.4.1.Materials

Prior to staining, the following reagents were prepared.

- PBS Stock: Into a Schott bottle, 20 PBS tablets were dissolved into 2 L of distilled water to create a PBS stock.
- PBST: To 1 L of PBS, 1 mL TWEEN-20 to create a 0.1% PBST solution
- PBST/BSA: 200 mg BSA was dissolved into PBST
- Blocking Agent: A solution of 10% normal horse serum was created by adding 50 µl of NHS to 450 µl PBST/BSA.
- Primary Antibody: The primary antibody used was the Androgen Receptor clone (AR441, DAKO). This antibody was diluted in PBST to a ratio of 1:50, making a total volume of 500 µL.
- Secondary Antibody: The secondary antibody was a FITC-labelled rabbit anti-mouse. A solution of 1:100 antibody:PBST/BSA was made up to a volume of 500 µL.

2.3.4.2.Methods

Immunofluorescence staining uses the location of antibodies and other genetic information within the sample to highlight regions of interest. By exploiting the genetic differences between each cell line, this allowed for a biological control to confirm that the differences observed using MSI techniques are in fact due to changing cell types.

Once sectioned, the samples for IF were fixed in ice cold acetone for 10 minutes. Following this, the slides were allowed to dry at room temperature and then the individual pellet sections were drawn around using a barrier marker (DAKO pen), creating a waterproof barrier. To each section, blocking agent (70 µL) was added and incubated for 15 minutes under ambient conditions. Each slide was washed using PBST/BSA twice for 5 minutes. To the damp slides, the primary antibody was added to each section (70 µL). Wet paper towels were placed around the slides in a suitable container to create a damp atmosphere, and the slides were incubated at 4 ˚C overnight. The damp atmosphere ensured minimum evaporation of the antibody during this time. Post-incubation, each slide was washed with PBS on a shaker for 4 minutes. This was repeated 3 times to ensure removal of the primary antibody. The secondary antibody (70 µL) was added to each section, and the slides were placed in the dark for 60 minutes under ambient conditions. Following incubation, the slides were once again washed 3 times with PBS on a shaker for 4 minutes. To each slide, coverslips were mounted using fluorescent mounting media with 0.0002% DAPI (ABCAM, ab104139). The addition of DAPI allows for an additional counter stain which binds strongly to adenine-thymine rich regions within the DNA.[21] Post staining, the slides were submitted to the Manchester Bioimaging facility for scanning using the Zeiss Axioimager upright fluorescence microscopes.

2.3.5. MS analysis

2.3.5.1. Desorption Electrospray Ionisation

Analysis of the cell samples on glass cover slips was performed on a Xevo G2-XS (Waters Corp.) QToF instrument with an attached DESI source. The DESI sprayer used was a prototype with heated capillary and fixed geometry, optimised for imaging applications. The fixed geometry of the sprayer allowed for higher consistancy between various data

aquisitions.[22] The solvent of choice was 98:2 methanol:H_2O which was used for optimum lipid sensitivity and the selected mass range is typical for a lipidomics experiment, at 50-1200 Da. This allowed for a full coverage of the species of interest. The instrument was operated with a solvent flow rate of 1.5 µL/min using the heated capilary set to 12,000 V to give an overall temperature of the capillary ~500 ˚C. The spot size used ranged from 250 µm down to 20 µm, depending on the sample of interest. The instrument ran at a typical rate of 4 scans per second. The data was aquired in both polarities.

2.3.5.2.Secondary Ion Mass Spectrometry

The instrument used for SIMS analysis was the J105 3D chemical imager (Ionoptika Ltd, Chandler's Ford, UK) described previously.[23] The primary ion beam employed was a 60 keV $(H_2O)_n$ cluster source. The use of the water cluster beam, allowed for detection of intact lipid species allowing for direct comparison with the DESI analysis. The water cluster beam was optimised to give a cluster size of approximately 27,000 water molecules. Using a field of view of 650 x 650 µm, and a raster of 128x128 pixels, optimisation enabled a pixel size of 5 µm. The mass range acquired was 95-1072 Da. The ion dose used was $1.26x10^{12}$ ions/cm^2 which allowed for etching of the sample to show species just below the surface. The pellet samples were analysed in both positive and negative mode.

2.3.6. Data Analysis

For all experiments, each pellet was repeated at in triplicate during the growth phase, then sectioned and analysed in technical replicates. For DESI and ToF-SIMS analysis, each sample was analysed and three individual regions were selected and extracted, allowing for technical repeats. The error bars were calculated using standard deviation. Multivariate analysis used was principal component analysis (PCA). For DESI experiments, regions of

interest (ROI) were selected and normalised to total ion count (TIC) using the HD imaging software (HDI v1.4, Waters Corporation, Wilmslow). The information from the mass range 500-900 was then extracted into a .csv format and uploaded into Metabolanalyst V4.0[24] for PCA analysis. MS/MS spectra were produced using collision energy between 30-40 V in negative mode.

In order to analyse the ToF-SIMS data, images were opened and examined using Ionoptika Image Analyser (v2, Ionoptika, Southampton). The pellets were analysed using an in-house Matlab (Mathworks) code which allowed for both PCA and K-means hierarchical clustering analysis. The selected pixels were sum normalised before undergoing multivariate analysis. All graphs were created using the GraphPad Prism 8.3 software (GraphPad Software, La Jolla California USA).

2.4. Results and Discussion

2.4.1. Desorption Electrospray Ionisation Mass Spectrometry Imaging

2.4.1.1. Control Cell Pellets

For each cell line, three individual pellets were used to allow for biological repeats, and within each pellet multiple regions were defined to give technical repeats. As a result, each cell line has an *n* value >9. The overall section was defined by mapping *m/z* 885.57, a value that has been shown in literature to be highly abundant in cellular material (Figure 2.1). For each cell line, a colour was arbitrarily selected to allow for identification of each throughout the data. These were; red, green and blue for LNCaP, PC-3 and PNT2-C2, respectively. Following this regions were extracted using the ROI tool within the HDI software (v1.4, Waters). Regions of 9 pixels were selected randomly throughout the cell

pellet to ensure a full coverage of the tissue on the slide. From each ROI, the corresponding spectra were extracted and subjected to multivariate analysis using MetaboAnalyst.[13]

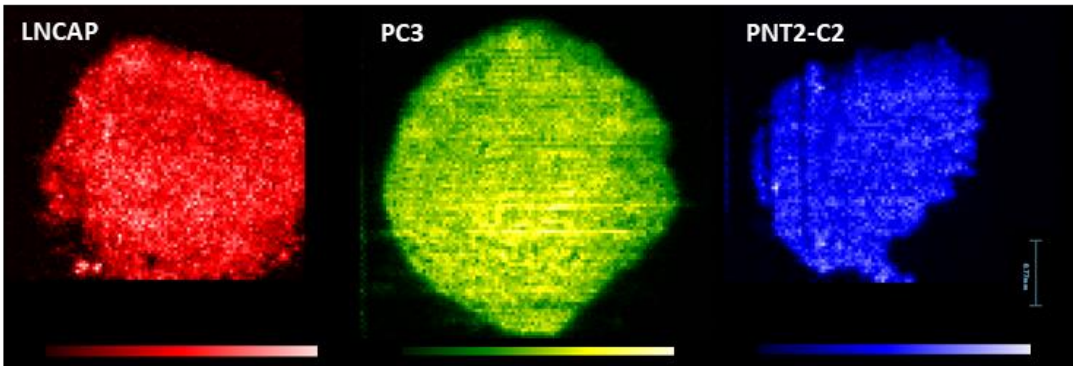

Figure 2.1 : Ion images of *m/z 887.57,* red, green and blue for each labelled cell line LNCaP, PC-3 and PNT2-C2 respectively.. Each image was acquired using the DESI- Xevo G2-XS with the pixel size set to 40 µm, The image was acquired with 20 scans a second in negative polarity.

The MVA primarily used for this study was principal component analysis (PCA) which converts the data provided orthogonally into sets of correlated variables, called principal components.[26] To first observe the differences within the cell lines, PCA was applied to the control cell pellets. Shown by the PCA plot (Figure 2.2) cell lines differentiate significantly across the 2 components which is expected due to their large biological differences.

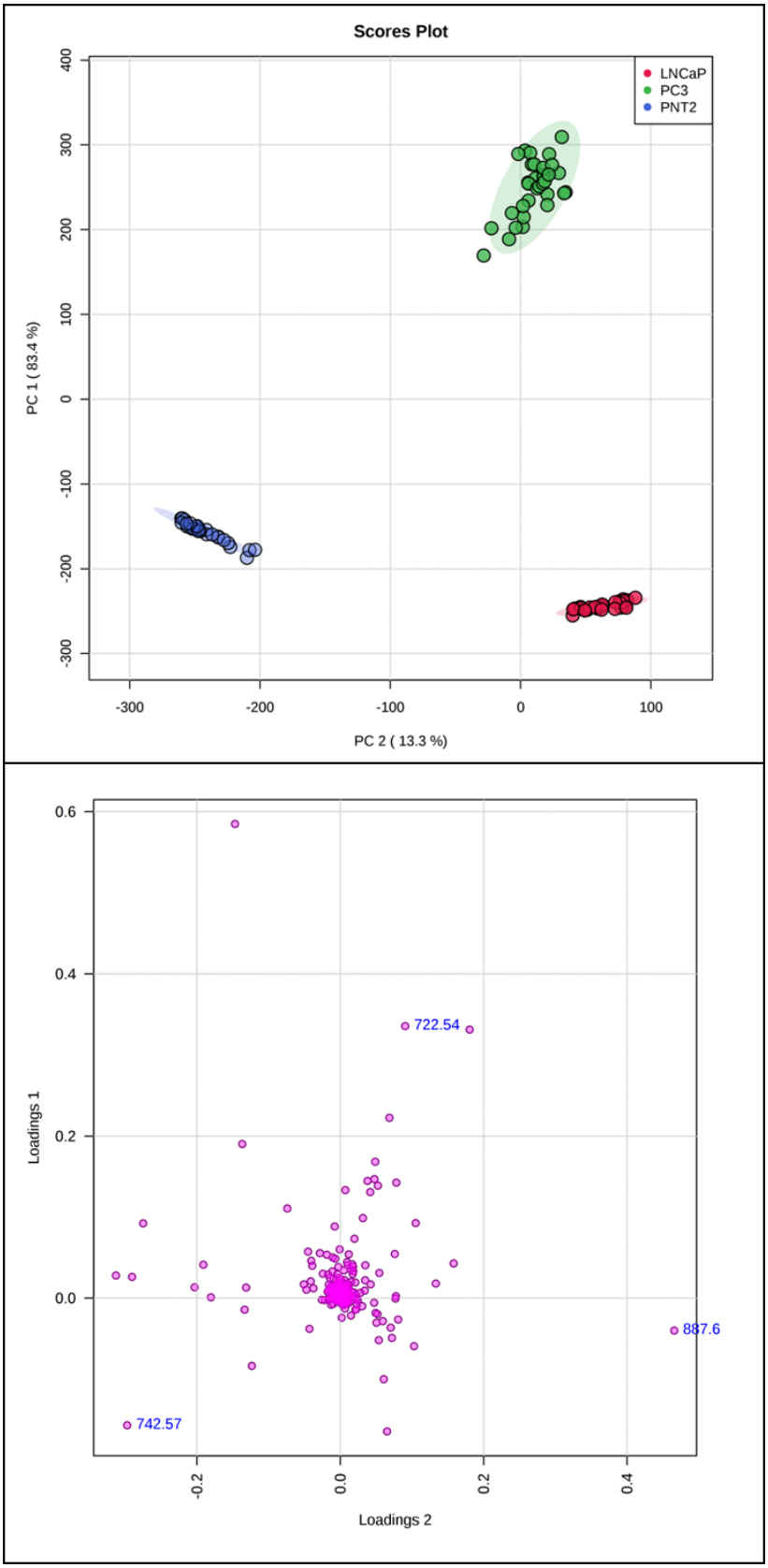

Figure 2.2: Above the extracted PCA plot produced using MetoboAnalyst software. The top figure shows the corresponding PCA plot for the ROI within the cell lines for both component 1 and 2. The bottom image shows the extracted loadings plot with the selected *m/z* species highlighted.

Following PCA, the corresponding loadings were extracted to determine the mass to charge values creating the primary differences within the cell lines (Figure 2.2). The *m/z* values that are significantly positively loaded in PC1 and PC2, correlate directly to the PC-3 cell line. The main value causing this discrimination is *m/z* 722.54. Using the corresponding loadings values for the remaining cell lines, *m/z* 887.6 was highly correlated to LNCaP and *m/z* 742.45, corresponded to cell line PNT2-C2. In order to validate the use of the *m/z* species as potential markers, corresponding boxplots were created. These boxplots demonstrate the spread of intensity for each *m/z* value from each region of interest selected for each cell line (Figure 2.3).

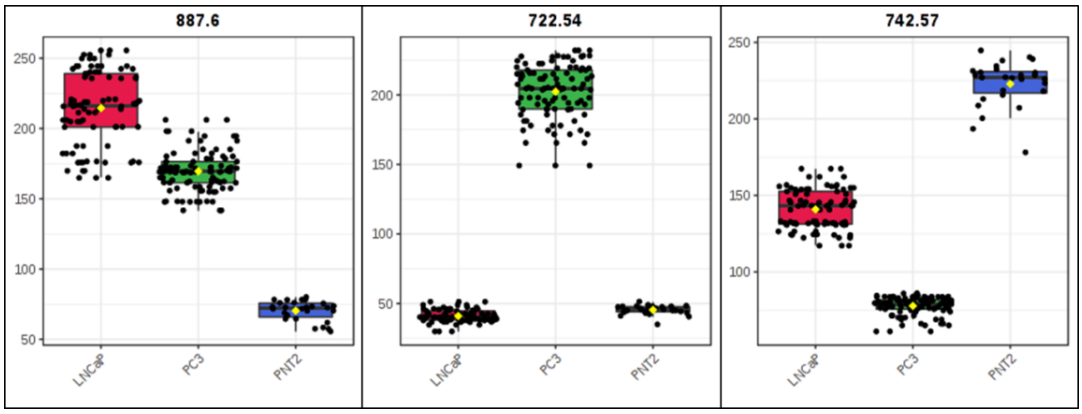

Figure 2.3: Boxplots for each *m/z* species. This exhibits distribution of the intensities for each ROI selected from the corresponding pellets for each of the labelled *m/z* species. The yellow dot indicates the average intensity for each cell line for the corresponding *m/z* species. The plots were created using MetoboAnalyst software.

As observed from the bloxplots (Figure 2.3), each *m/z* value selected is most abundant for the corresponding cell line. This highlights the potential of using these *m/z* values to differentiate within the cell lines. From the above results, a clear defined list of *m/z* values allowing for discrimination of the selected cell lines. In order to determine the lipid species that correspond to this mass, MS/MS experiments were employed.

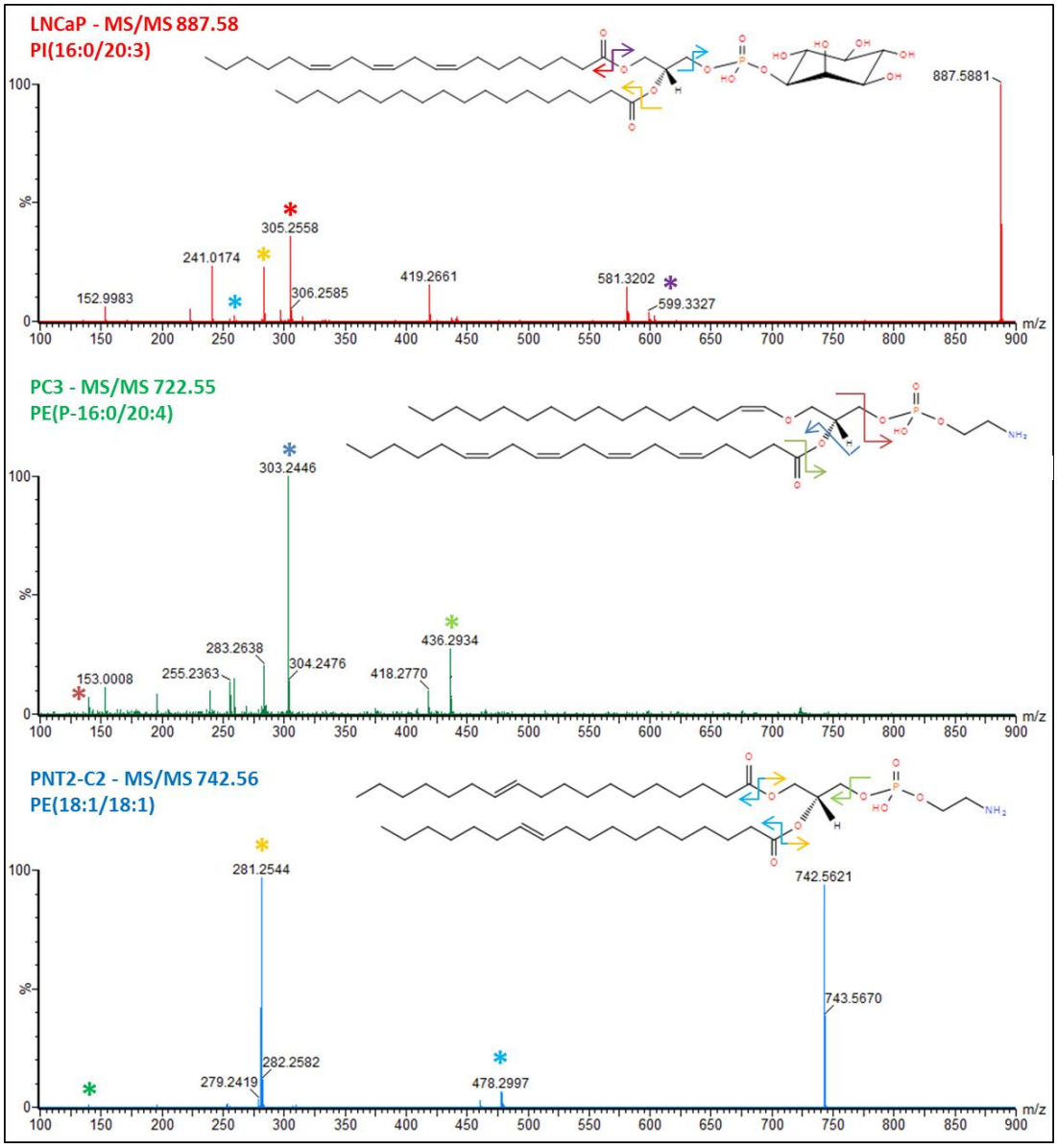

Figure 2.4: MS/MS spectra for the selected *m/z* species defined to distinguish each cell line. The suggested structure for each is placed above the corresponding spectra. The coloured arrows on each structure correspond to the fragment peak labelled with an asterisk of the same colour. The DESI spectra were acquired in negative mode with a *m/z* range from 100-900 Daltons and a collision energy between 15-30 kV.

The MS/MS spectra were compared to standard samples used on the LIPID MAPS online MS/MS predictor tool (https://www.lipidmaps.org/). This allowed for an initial degree of confidence for the lipid assignment for each species (Figure 2.4), (Supplementary; Table 2.2).

2.4.1.2. Mixed Cell Lines

Once the *m/z* species were selected to discriminate each cell line, the mixed cell pellet samples were analysed.

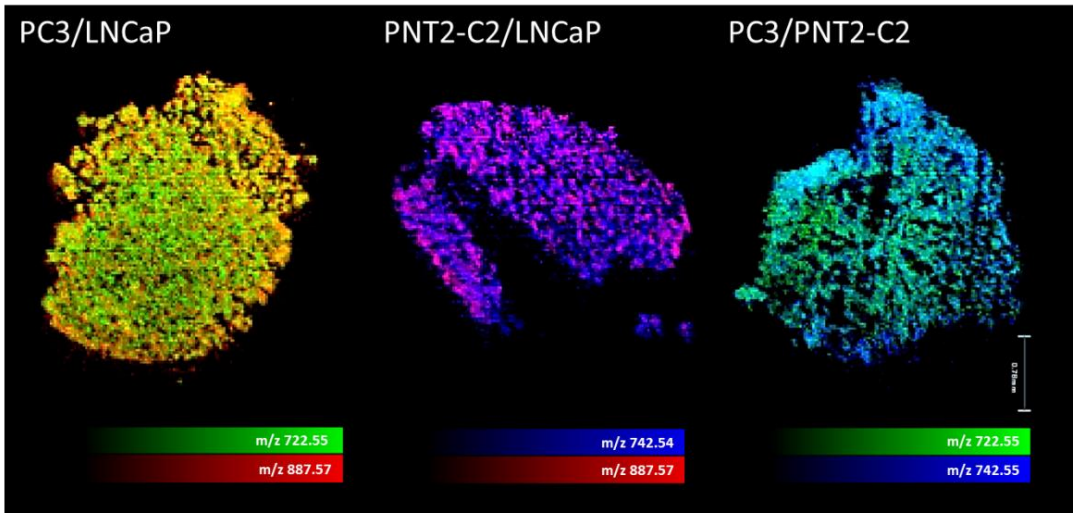

Figure 2.5: The above images show the distribution of the corresponding coloured *m/z* species for each labelled pellet section. The images were acquired using the Xevo G2-XS mass spectrometer coupled to a DESI source in negative mode with 10 scans per second. The pixel size was set to 25 µm.

Shown above (Figure 2.5), using the previously determined *m/z* values, it was possible to observe defined regions within the tissue. This suggests that the corresponding lipid species are potentially highlighting differing regions of cellular material within the pellet. In order to confirm that the variations detected are in fact due to changing cell types, immunofluorescent staining was performed on adjacent pellet sections. Using immunohistochemistry is the typical method used for distinguishing regions of interest within clinical samples.

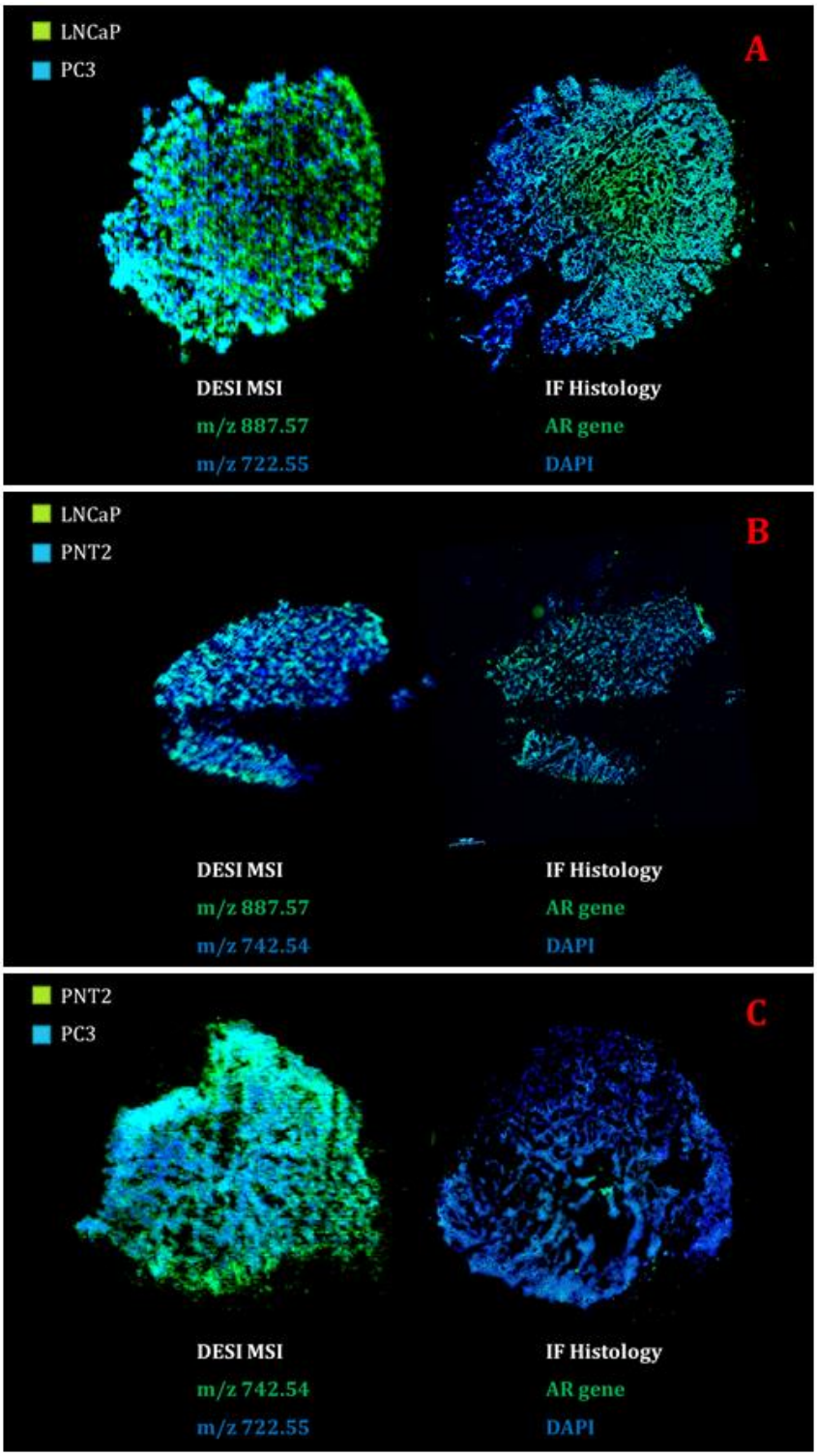

Figure 2.6: For each pellet (A-C), the DESI image is on the left hand side and the adjacent immunohistochemically stained section is on the right hand side. Each DESI image shows an overlay of the selected two *m/z* values creating discrimination, coloured to enable direct comparison with the IF image. The *m/z* values have been labelled with the suggested cell type it represents. The IHC image shows the distribution of the AR gene across the pellet section. The DESI image was acquired using the Xevo G2-XS mass spectrometer coupled to a DESI source in negative mode with 10 scans per second with the pixel size was set to 25 µm. The IHC images were created using the Zeiss Axioimager upright fluorescence microscope.

For the immunohistochemistry, the AR gene targeted within the staining protocol. This gene is only present in the LNCaP cell line allowing for distinction between the LNCaP cell line and the PC-3 and PNT2-C2 cell lines. However, staining with this method cannot differentiate between the PC-3 and PNT2-C2 cell line. Above, (Figure 2.6), comparison of the IF stained sections and the corresponding DESI image shows that the differences observed using the defined *m/z* values are due to the difference in cell types. It also highlights that DESI imaging is able to differentiate between the PNT2-C2 and PC-3 cell lines, whereas this isn't possible for the IHC with the selected antibody. This demonstrates the potential in moving to a mass spectrometry imaging based screening system.

2.4.2. Secondary Ion Mass Spectrometry Imaging

The data shown thus far has shown great potential in using MSI techniques within the clinic. However, the major limitation of using DESI is the spatial resolution is much larger than that observed using high resolution light microscopes, typically used within the clinic. The smallest pixel size typically used within DESI experiments is between 20-50 µm. Conversely, the standard microscope resolution used for analysis of biopsies can range from 200 – 500 nm. SIMS has the potential to image tissue down to submicron spatial resolution. Therefore, in order to explore the difference in spatial resolution in more detail, the experimental was continued using the SIMS as the MSI platform.

2.4.2.1.Mixed Cell Line

Using k-means clustering, the mixed cell line images were processed. This allowed for segmentation of the largest differing regions in the image.

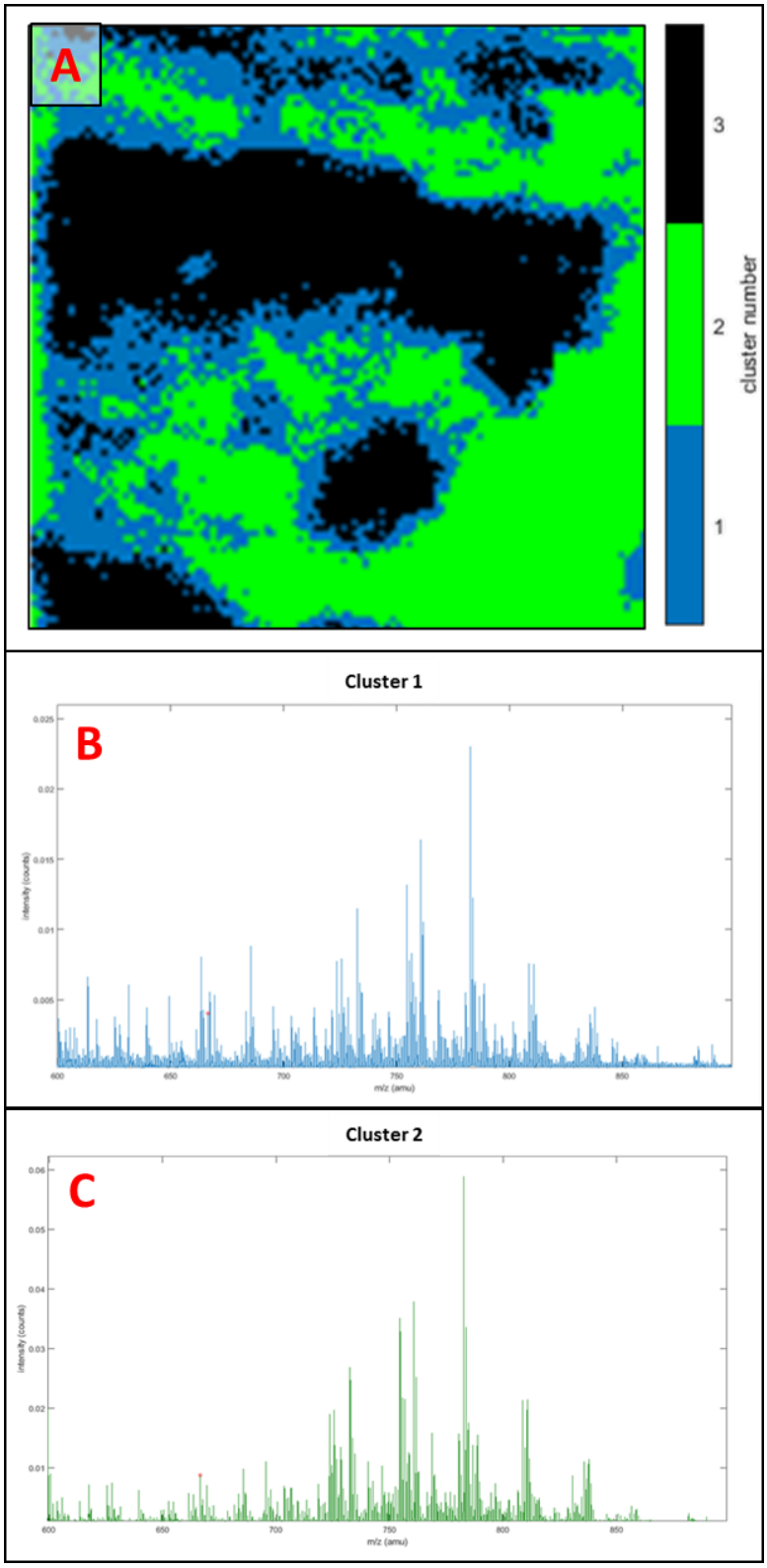

Figure 2.7: K-means cluster analysis (A) for the PC-3/PNT2-C2 mixed cell pellet, where clusters 1 and 2 show biological material and cluster 3 shows background. B and C show the corresponding spectra for the clusters containing biological material. The data was acquired using ToF-SIMS J105 instrument utilising the (H2O)27K ion beam in positive mode and the image analysed using an in-house Matlab code.

The k-mean analysis, Figure 2.7, allowed for separation between the biological material of the pellet and the background with clusters 1 and 2 versus cluster 3 (Supplementary; Figure 2.11). A spectral overlay of clusters 1 and 2 was produced to allow for investigation into *m/z* values responsible for the k-means segregation. From the k-means cluster overlay the *m/z* values that were significantly different for each cluster were selected. These were then compared to an overlay of control spectra to confirm the differences observed within the cluster and therefore tentatively assign the cell line to the corresponding cluster.

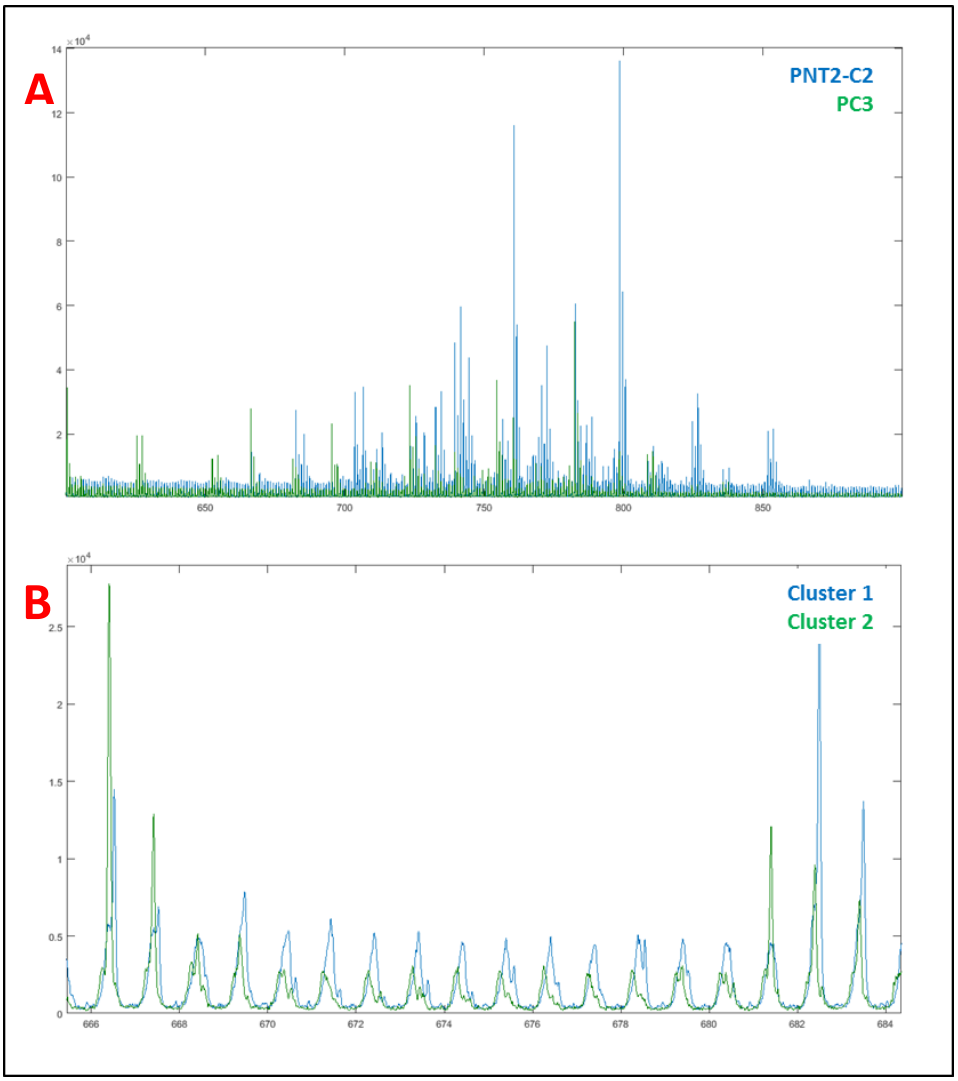

Figure 2.8: The overlap of the control spectra (A) for PNT2-C2 and PC-3. B shows the k-means cluster analysis spectral overlay for the clusters 1 and 2 mixed cell pellet in the zoomed region of interest. The data was acquired using ToF-SIMS J105 instrument utilising the (H2O)27K ion beam in positive mode and the image analysed using an in-house Matlab code.

The selected *m/z* species from the cluster overlay were compared to the control spectra, Figure 2.8. This enabled a depiction of the changes occurring from the cluster map using the ratios of *m/z* 666.5 and 683.5. For the PC-3 cell line, *m/z* 666.5 was higher in intensity and *m/z* 683.5 was lower. For the PNT2-C2 this trend was reversed. In order to explore this further, these *m/z* values were imaged.

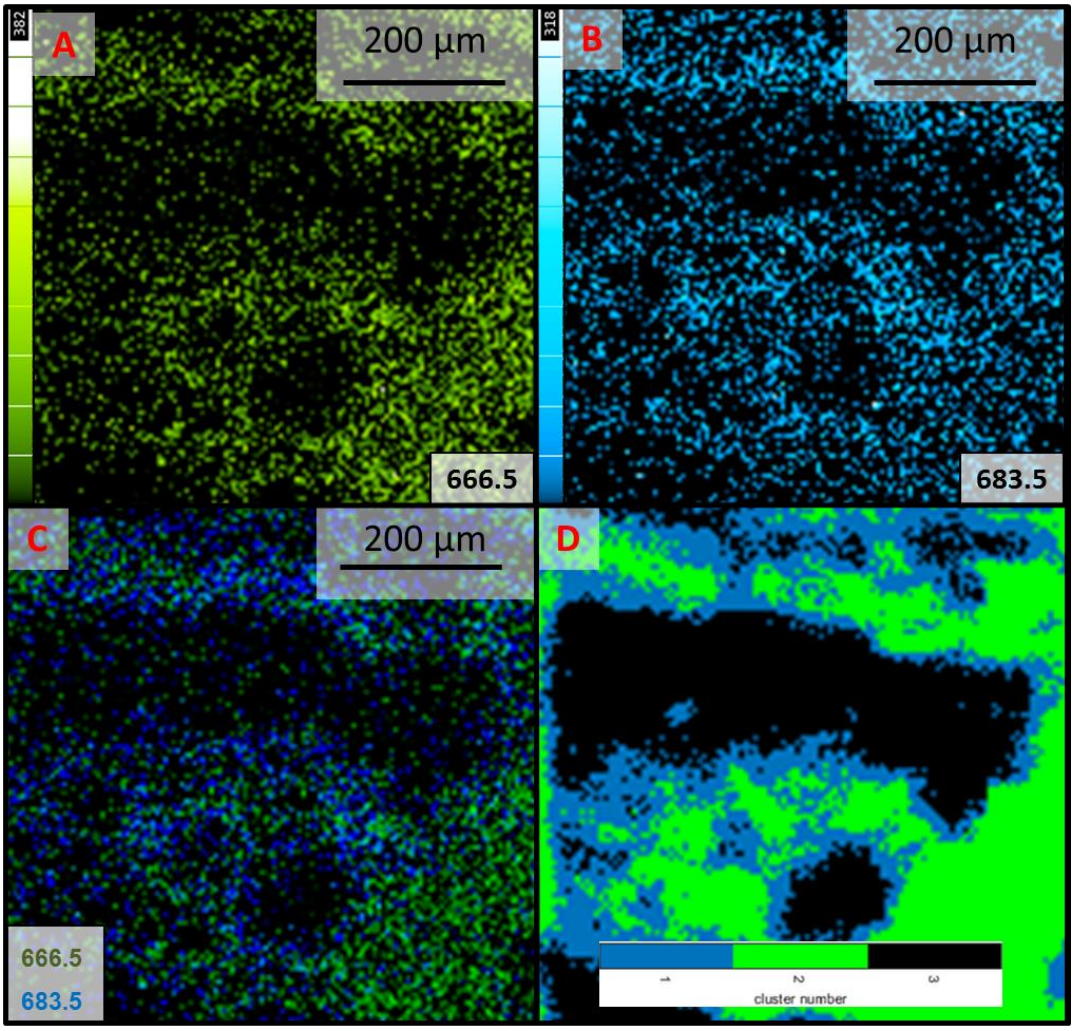

Figure 2.9: A and B show the distribution of the selected lipids *m/z* 666.5 and *m/z* 683.5, respectively. C is an overlay image of the two *m/z* values. D shows the k-means cluster analysis for the PC-3/PNT2-C2 mixed cell pellet The data was acquired using ToF-SIMS J105 instrument utilising the (H2O)27K ion beam in positive mode and the image analysed using an in-house Matlab code.

As demonstrated in Figure 2.9, the overlay of these two *m/z* values matches the k-means cluster map. This highlights the ability of ToF-SIMS to allow for potential differentiation between cell lines. Further work will look at confirming the identity of these species causing

the diversities. Also, using staining techniques such as IF described earlier to confirm that the differences observed are due to changing cell lines. This analysis was repeated for the remaining mixed pellets and observed, (Supplementary; 2.12-2.17), ToF-SIMS was able to distinguish between the cluster regions.

Although the data was acquired in a different polarity for the ToF-SIMS data versus the DESI data, what is clear that you get a complementary data set. Both instrumentations have highlighted the ability to distinguish cell lines in a mixed media, as well as define these cell types with a series of *m/z* values. Looking at the raw spectra for the control cell line PNT2-C2, what is observed is that for ToF-SIMS, there is a different set of lipids that are observed with DESI due to the differing ionisation method.

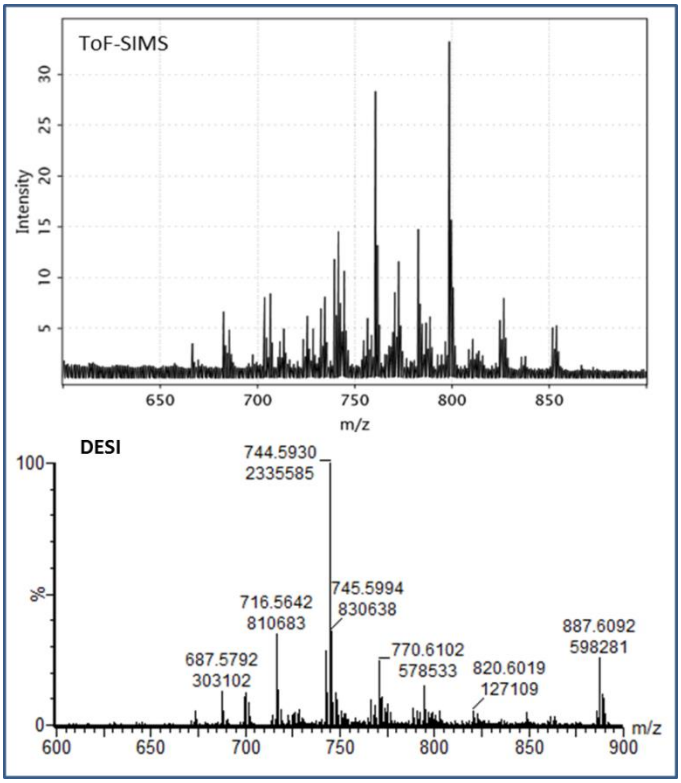

Figure 2.10: A comparison of the lipid region, *m/z* 600-900, of the spectra for the PNT2-C2 cell line acquired for ToF-SIMS and DESI. The ToF-SIMS data was acquired using J105 instrument utilising the (H2O)27K ion beam in positive mode and the image analysed using an in-house Matlab code. The DESI data was acquired using the Xevo G2-XS mass spectrometer coupled to a DESI source in negative mode with 10 scans per second.

As observed (Figure 2.10), the lipid profile obtained in the two polarities is very different for both techniques, allowing for a more comprehensive coverage of the lipid species within the sample. This again highlights how useful these techniques are when used together as it allows for an expanded set of *m/z* values to be investigated. Further work will explore the spectral differences between instruments in each polarity mode.

2.5. Conclusions

These results have demonstrated the potential of using the MSI method to differentiate closely related cell types within a mixed cell pellet. Furthermore, where IF failed to separate the PC-3 and PNT2-C2 cell regions, DESI imaging has succeed. This has further highlighted the potential of using MSI methods on clinical samples. Although DESI provides us with the benefits of analysis under ambient conditions, using higher spatial resolution instrumentation such as ToF-SIMS provided an image which can correlate better with the resolution of the immunohistochemically stained images. This allows for a more comprehensive overview of what is happening within the tissue samples on a cellular scale, and would be important for example in identifying small populations of aggressive cells infiltrating healthy tissue regions. Future work will expand upon this technique to explore negative mode ToF-SIMS, as well as increase the spatial resolution to match that of the immunohistochemistry. Analysis of the pseudo tissue allowed for confirmation that mass spectrometry imaging can be used for a large variety of cell types.

2.6. Acknowledgments

The author acknowledges and gives thanks for the work and services provided by the following departments

- Manchester Bioimaging Facility for analysis of the IHC slides.
- Cancer Research UK, targeted therapy and oncology group at the University of Manchester for access to the xenograft models.
- EPSRC and Waters for funding of a studentship to the author
- ToF-SIMS instrument EPSRC grant EP/S019863/1

2.7. References

(1) Siegel, R. L.; Miller, K. D.; Jemal, A. Cancer Statistics, 2019. *CA. Cancer J. Clin.* **2019**, *69* (1), 7–34. https://doi.org/10.3322/caac.21551.

(2) Chodak, G. Prostate Cancer: Epidemiology, Screening, and Biomarkers. *Rev. Urol.* **2006**, *8* (Suppl 2), S3–S8.

(3) Velonas, V. M.; Woo, H. H.; Remedios, C. G. dos; Assinder, S. J. Current Status of Biomarkers for Prostate Cancer. *Int. J. Mol. Sci.* **2013**, *14* (6), 11034–11060. https://doi.org/10.3390/ijms140611034.

(4) Thompson, I. M.; Pauler, D. K.; Goodman, P. J.; Tangen, C. M.; Lucia, M. S.; Parnes, H. L.; Minasian, L. M.; Ford, L. G.; Lippman, S. M.; Crawford, E. D.; Crowley, J. J.; Coltman, C. A. J. Prevalence of Prostate Cancer among Men with a Prostate-Specific Antigen Level ≤4.0 ng per Milliliter https://www.nejm.org/doi/10.1056/NEJMoa031918?url_ver=Z39.88-2003&rfr_id=ori%3Arid%3Acrossref.org&rfr_dat=cr_pub%3Dwww.ncbi.nlm.nih.gov (accessed Nov 27, 2019). https://doi.org/10.1056/NEJMoa031918.

(5) BARRY, M. J. Early Detection and Aggressive Treatment of Prostate Cancer. *J. Gen. Intern. Med.* **2000**, *15* (10), 749–751. https://doi.org/10.1046/j.1525-1497.2000.00816.x.

(6) Steentjes, L.; Siesling, S.; Drummond, F. J.; Manen, J. G. van; Sharp, L.; Gavin, A. Factors Associated with Current and Severe Physical Side-Effects after Prostate Cancer Treatment: What Men Report. *Eur. J. Cancer Care (Engl.)* **2018**, *27* (1), e12589. https://doi.org/10.1111/ecc.12589.

(7) Jonas Hugosson, Johan Stranne, Sigrid V. Carlsson. Radical Retropubic Prostatectomy: A Review of Outcomes and Side-Effects. *Acta Oncol. 50*, 92–97.

(8) Horoszewicz, J. S.; Leong, S. S.; Kawinski, E.; Karr, J. P.; Rosenthal, H.; Chu, T. M.; Mirand, E. A.; Murphy, G. P. LNCaP Model of Human Prostatic Carcinoma. *Cancer Res.* **1983**, *43* (4), 1809–1818.

(9) Titford, M. The Long History of Hematoxylin. *Biotech. Histochem.* **2005**, *80* (2), 73–78. https://doi.org/10.1080/10520290500138372.

(10) Alturkistani, H. A.; Tashkandi, F. M.; Mohammedsaleh, Z. M. Histological Stains: A Literature Review and Case Study. *Glob. J. Health Sci.* **2016**, *8* (3), 72–79. https://doi.org/10.5539/gjhs.v8n3p72.

(11) McDonnell, L. A.; Angel, P. M.; Lou, S.; Drake, R. R. Chapter Eleven - Mass Spectrometry Imaging in Cancer Research: Future Perspectives. In *Advances in*

Cancer Research; Drake, R. R., McDonnell, L. A., Eds.; Applications of Mass Spectrometry Imaging to Cancer; Academic Press, 2017; Vol. 134, pp 283–290. https://doi.org/10.1016/bs.acr.2016.11.010.

(12) Arentz, G.; Mittal, P.; Zhang, C.; Ho, Y.-Y.; Briggs, M.; Winderbaum, L.; Hoffmann, M. K.; Hoffmann, P. Applications of Mass Spectrometry Imaging to Cancer. *Adv. Cancer Res. 134*, 27–66.

(13) van Steenbrugge, G. J.; van Uffelen, C. J.; Bolt, J.; Schröder, F. H. The Human Prostatic Cancer Cell Line LNCaP and Its Derived Sublines: An in Vitro Model for the Study of Androgen Sensitivity. *J. Steroid Biochem. Mol. Biol.* **1991**, *40* (1–3), 207–214.

(14) Schuurmans, A. L.; Bolt, J.; Veldscholte, J.; Mulder, E. Regulation of Growth of LNCaP Human Prostate Tumor Cells by Growth Factors and Steroid Hormones. *J. Steroid Biochem. Mol. Biol.* **1991**, *40* (1–3), 193–197.

(15) MuraliKrishna, P. S.; Gondi, C. S.; Lakka, S. S.; Julta, A.; Estes, N.; Gujrati, M.; Rao, J. S. RNA Interference-Directed Knockdown of Urokinase Plasminogen Activator and Urokinase Plasminogen Activator Receptor Inhibits Prostate Cancer Cell Invasion, Survival and Tumorigenicity In Vivo. *J. Biol. Chem.* **2005**, *280* (43), 36529–36540. https://doi.org/10.1074/jbc.M503111200.

(16) Kaighn, M. E.; Narayan, K. S.; Ohnuki, Y.; Lechner, J. F.; Jones, L. W. Establishment and Characterization of a Human Prostatic Carcinoma Cell Line (PC-3). *Invest. Urol.* **1979**, *17* (1), 16–23.

(17) Tai, S.; Sun, Y.; Squires, J. M.; Zhang, H.; Oh, W. K.; Liang, C.-Z.; Huang, J. PC3 Is a Cell Line Characteristic of Prostatic Small Cell Carcinoma. *The Prostate* **2011**, *71* (15), 1668–1679. https://doi.org/10.1002/pros.21383.

(18) Cussenot, O.; Berthon, P.; Berger, R.; Mowszowicz, I.; Faille, A.; Hojman, F.; Teillac, P.; Le Duc, A.; Calvo, F. Immortilization of Human Adult Normal Prostatic Epithelial Cell by Liposomes Containing Large T-SV40 Gene. *J. Urol.* **1991**, *143*, 881–886.

(19) LNCaP clone FGC ATCC ® CRL-1740™ Homo sapiens prostate; deri https://www.lgcstandards-atcc.org/products/all/CRL-1740.aspx?geo_country=gb#documentation (accessed Jun 24, 2017).

(20) Malm, J.; Giannaras, D.; Riehle, M. O.; Gadegaard, N.; Sjövall, P. Fixation and Drying Protocols for the Preparation of Cell Samples for Time-of-Flight Secondary Ion Mass Spectrometry Analysis. *Anal. Chem.* **2009**, *81* (17), 7197–7205. https://doi.org/10.1021/ac900636v.

(21) Kapuscinski, J. DAPI: A DNA-Specific Fluorescent Probe. *Biotech. Histochem.* **1995**, *70* (5), 220–233. https://doi.org/10.3109/10520299509108199.

(22) Investigation of the Impact of Desorption Electrospray Ionization Sprayer Geometry on Its Performance in Imaging of Biological Tissue | Analytical Chemistry https://pubs.acs.org/doi/abs/10.1021/acs.analchem.6b00345 (accessed Jan 11, 2021).

(23) Fletcher, J. S.; Rabbani, S.; Henderson, A.; Blenkinsopp, P.; Thompson, S. P.; Lockyer, N. P.; Vickerman, J. C. A New Dynamic in Mass Spectral Imaging of Single Biological Cells. *Anal. Chem.* **2008**, *80* (23), 9058–9064. https://doi.org/10.1021/ac8015278.

(24) Chong, J.; Wishart, D. S.; Xia, J. Using MetaboAnalyst 4.0 for Comprehensive and Integrative Metabolomics Data Analysis. *Curr. Protoc. Bioinforma.* **2019**, *68* (1), e86. https://doi.org/10.1002/cpbi.86.

(25) Chong, J.; Soufan, O.; Li, C.; Caraus, I.; Li, S.; Bourque, G.; Wishart, D. S.; Xia, J. MetaboAnalyst 4.0: Towards More Transparent and Integrative Metabolomics Analysis. *Nucleic Acids Res.* **2018**, *46* (W1), W486–W494. https://doi.org/10.1093/nar/gky310.

(26) Jolliffe, I. T.; Cadima, J. Principal Component Analysis: A Review and Recent Developments. *Philos. Transact. A Math. Phys. Eng. Sci.* **2016**, *374* (2065). https://doi.org/10.1098/rsta.2015.0202.

2.8. Supplementary

Table 2.2: The associated fragments and their assignments and theoretical masses for the selected *m/z* species acquired with DESI in negative ion mode

Parent Ion *m/z*	Daughter Ion *m/z*	Fragment theoretical mass	Fragment Assignment	Putative Assignment
887.5881	152.9983	152.9958	Glycerol-3-phosphate ion with loss of H2O	PI(18:0/20:3)
	223.0056	223.0013	Inositol phosphate ion - 2 H2O	
	241.0174	241.0119	Inositol phosphate ion - H2O	
	283.2708	283.2643	FA 18:0 sn1 RCOO- ion	
	305.2558	305.2486	FA 20:3 sn2 RCOO- ion	
	419.2703	419.2568	Neutral loss of sn2 RCOOH group and inositol from [M-H]-	
	581.3251	581.3096	Neutral loss of sn2 RCOOH group from [M-H]-	
	599.3427	599.3202	Loss of sn2 acyl chain as ketene (RCH=C=O) from [M-H]-	
722.55	140.0095	140.0118	Ethanolamine phosphate ion	PE(P-16:0/20:4)
	303.2446	303.233	FA 20:4 sn2 RCOO- ion	
	418.277	418.2728	Neutral loss of sn2 RCOOH group from [M-H]-	
	436.2934	436.2834	Loss of FA 20:4 sn2 acyl chain as ketene (RCH=C=O) from [M-H]-	
742.5621	140.0095	140.0118	Ethanolamine phosphate ion	PE(18:1/18:1)
	281.2544	281.2486	FA 18:1 sn1/sn2 RCOO- ion	
	478.2997	478.2939	Loss of sn2 acyl chain as ketene (RCH=C=O) from [M-H]-	

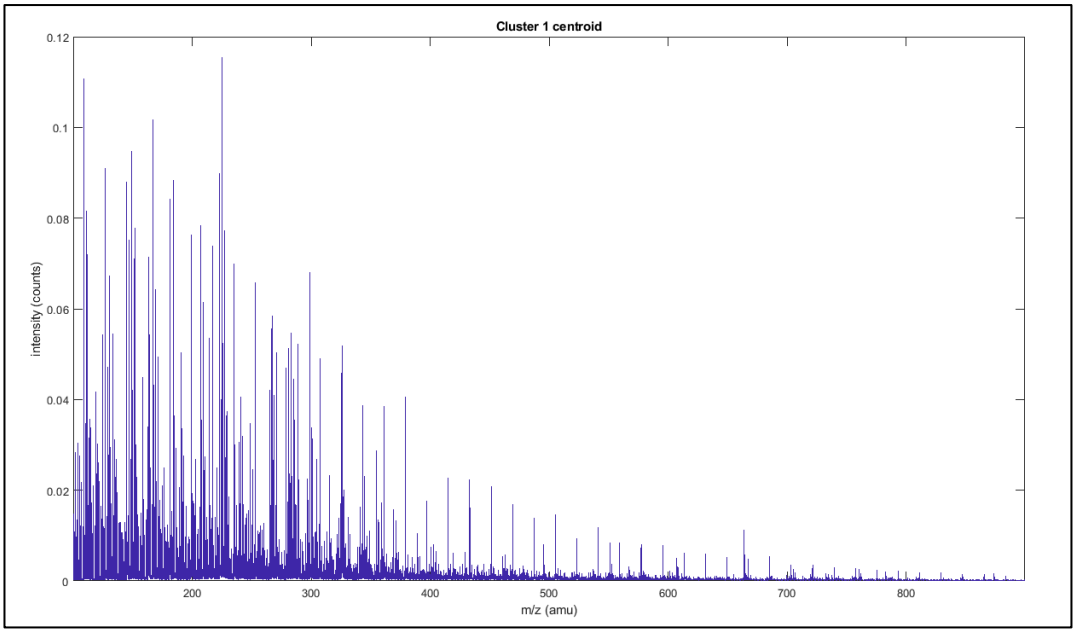

Figure 2.11: The spectra from cluster 1 following k-means segmentation analysis on the PC-3/PNT2-C2 mixed cell line pellet.

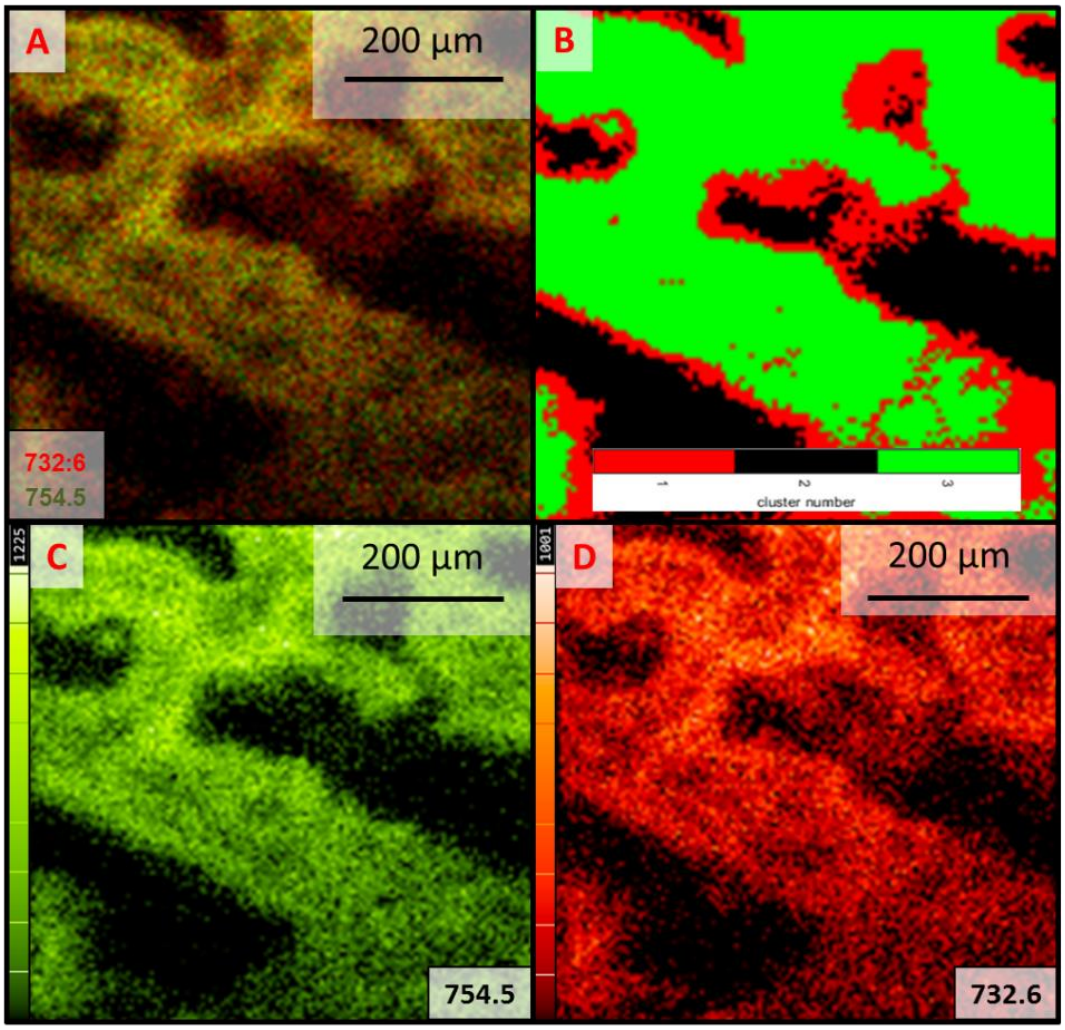

Figure 2.12: An overlay image (A) of the two *m/z* values defined, *m/z* 754.5 and *m/z* 732.6. B shows the k-means cluster analysis for the PC-3/LNCaP mixed cell pellet C and D show the distribution of the selected lipids *m/z* 754.5 and *m/z* 732.6, respectively. The data was acquired using ToF-SIMS J105 instrument utilising the (H2O)27K ion beam in positive mode and the image analysed using an in-house Matlab code.

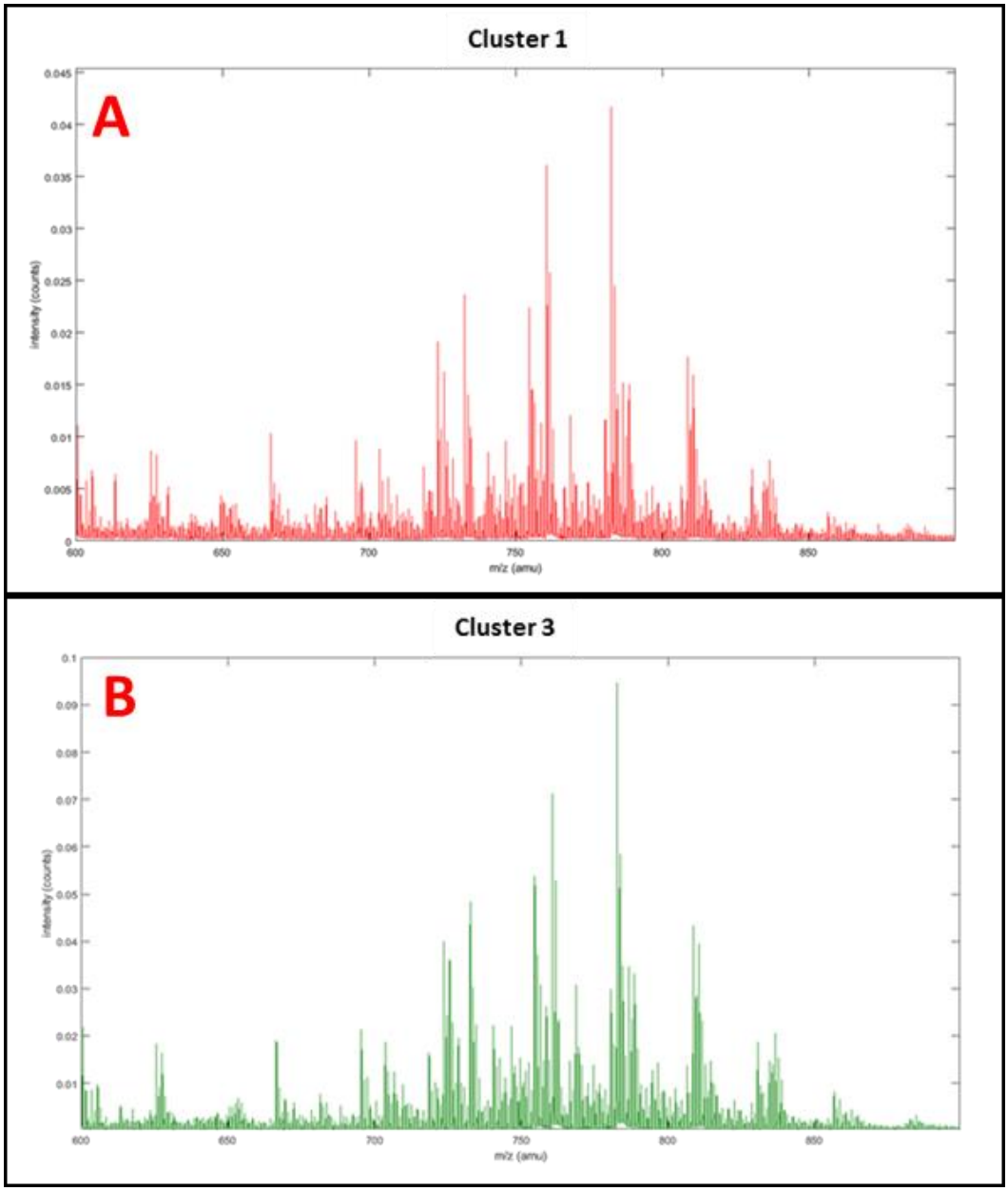

Figure 2.13: A and B show the corresponding spectra for the clusters containing biological material following the k-means cluster analysis for the PC-3/LNCaP mixed cell pellet. The data was acquired using ToF-SIMS J105 instrument utilising the (H2O)27K ion beam in positive mode and the image analysed using an in-house Matlab code

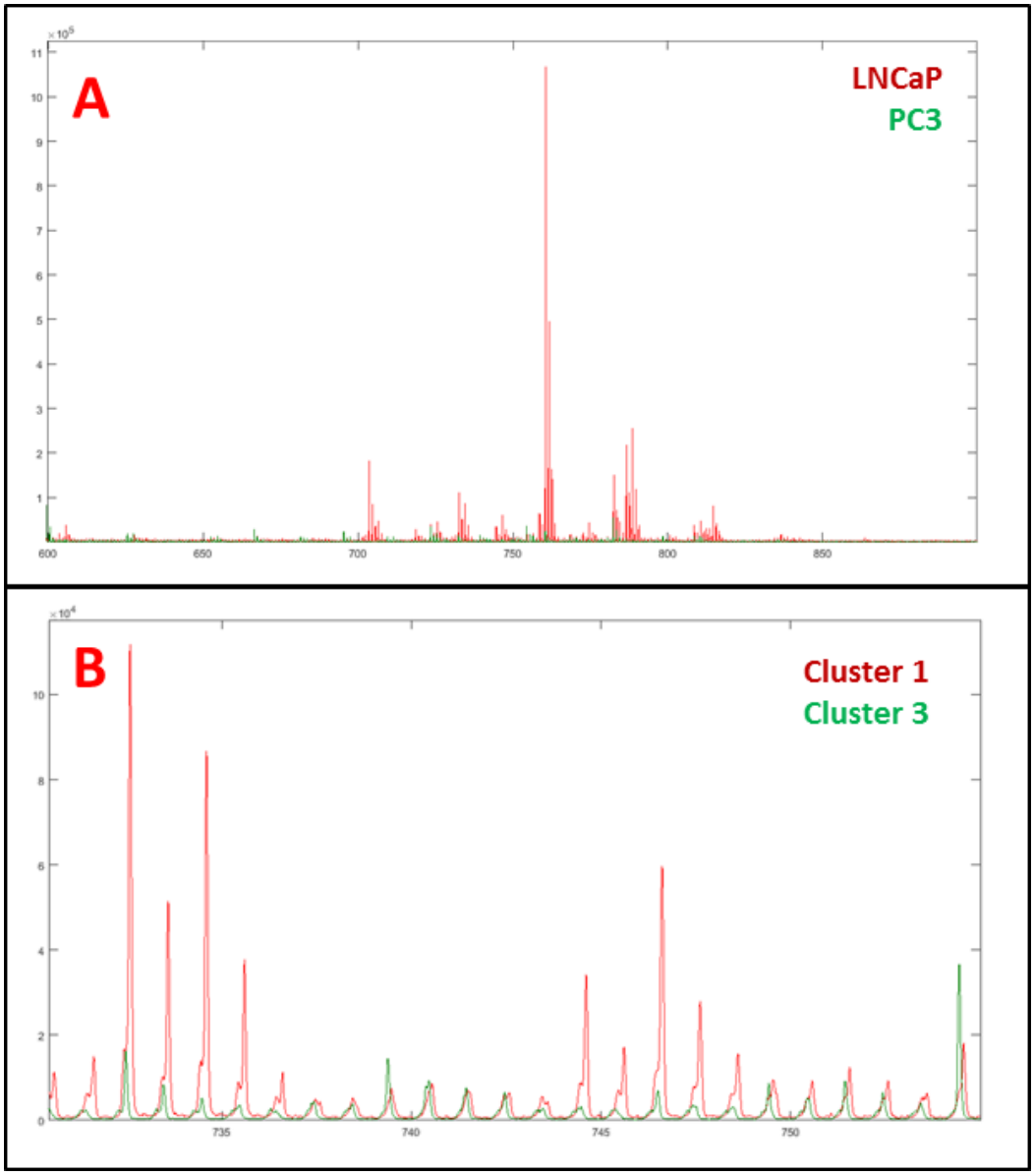

Figure 2.14: A shows the overlap of the control spectra for LNCaP and PC-3 cell line. B shows the k-means cluster analysis overlapped spectra for clusters 1 and 3 in the zoomed region of interest. The data was acquired using ToF-SIMS J105 instrument utilising the (H2O)27K ion beam in positive mode and the image analysed using an in-house Matlab code

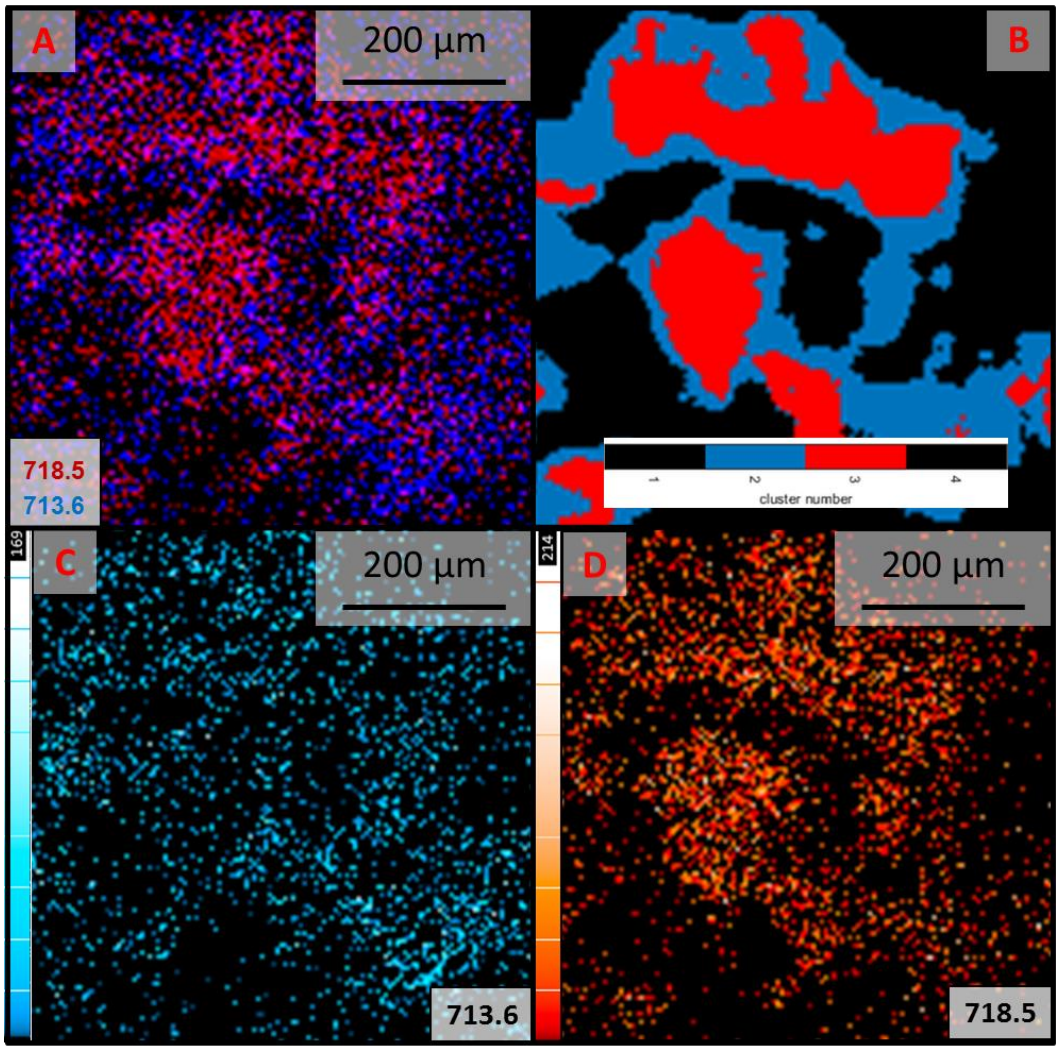

Figure 2.15: A is an overlay image of the two *m/z* values defined, *m/z* 718.5 and *m/z* 713.6. B shows the k-means cluster analysis for the PNT2-C2/LNCaP mixed cell pellet C and D show the distribution of the selected lipids *m/z* 718.5 and *m/z* 713.6 respectively. The data was acquired using ToF-SIMS J105 instrument utilising the (H2O)27K ion beam in positive mode and the image analysed using an in-house Matlab code.

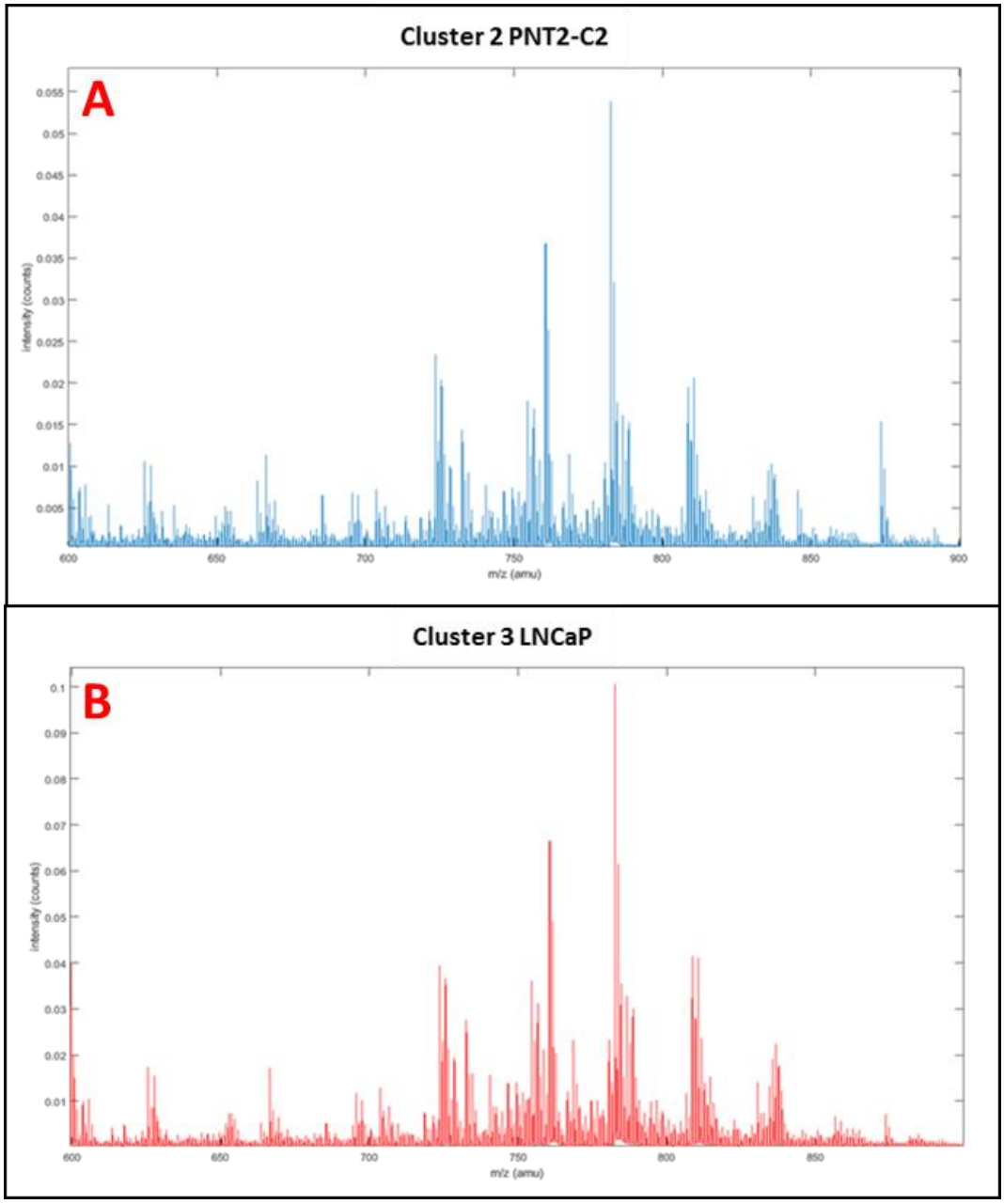

Figure 2.16: A and B show the corresponding spectra for the clusters containing biological material following the k-means cluster analysis for the PNT2-C2/LNCaP mixed cell pellet. The data was acquired using ToF-SIMS J105 instrument utilising the (H2O)27K ion beam in positive mode and the image analysed using an in-house Matlab code

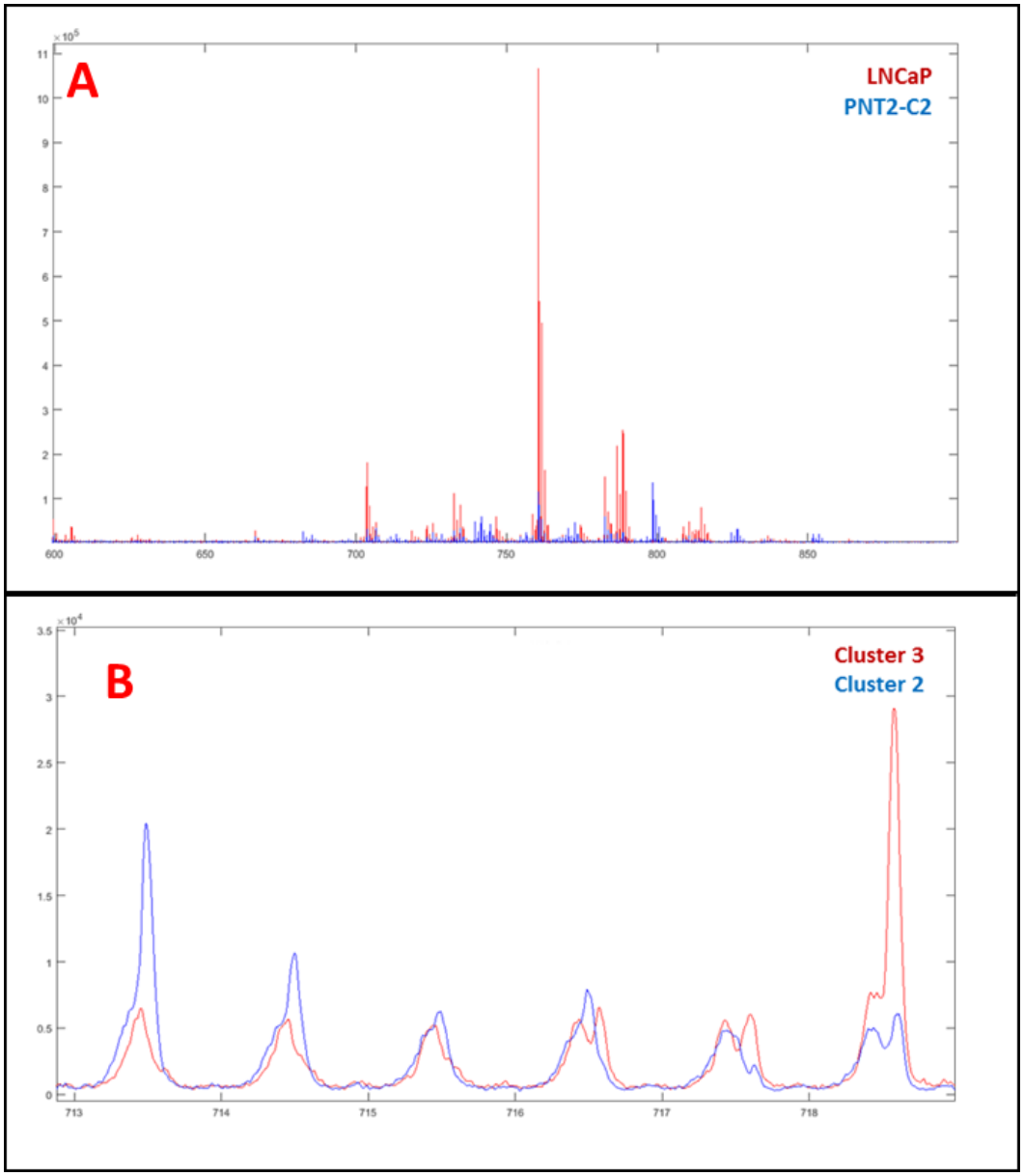

Figure 2.17: A shows the overlap of the control spectra for LNCaP and PNT2-C2 cell line. B shows the k-means cluster analysis overlapped spectra for clusters 2 and 3 in the zoomed region of interest. The data was acquired using ToF-SIMS J105 instrument utilising the (H2O)27K ion beam in positive mode and the image analysed using an in-house Matlab code

Chapter 3

Optimisation of Laser-REIMS for lipidomics cell based analysis

3. Optimisation of Laser-REIMS for lipidomics cell based analysis

Danielle J McDougall[1,2],, Emrys Jones[2], Adam McMahon[3], Kaye Williams[4], Nicholas Lockyer[1]

1. Department of Chemistry, Photon Science Institute, Alan Turing Building, University of Manchester, Manchester, UK
2. Waters, Department of Research and Development, Wilmslow, UK
3. Wolfson Molecular Imaging Centre, University of Manchester, Manchester, UK
4. Division of Pharmacy and Optometry, Faculty of Biology, Medicine and Health, Stopford Building, University of Manchester, Manchester, UK

3.1. Abstract

Rapid evaporative ionisation mass spectrometry (REIMS) is a relatively new technique within the ambient analysis mass spectrometry field. Over recent years this technique has evolved, highlighting its potential as a rapid screening technique. Therefore, a more versatile method was developed in order to be able to increase efficiency and enable high throughput profiling of cell culture samples in 96 well plates. This study explored the experimental parameters such as cell culture sample preparation, as well as optimisation of fundamental mechanisms that occur within the technique. These included; laser power, dwell time, and solvent flow rates. This allowed for optimisation from benchtop to mass spectrometry analysis, allowing for a streamlined and optimised workflow for a lipidomic profile of cellular screening using the Laser REIMS system. In order to expand this further, a range of species were targeted to allow for detection of a wider molecular coverage. Overall, this paper demonstrates the optimum experimental set up to ensure rapid analysis of cell culture samples.

3.2. Introduction

Rapid evaporative ionisation mass spectrometry (REIMS) is a method developed in 2009,[1] initially using a surgical knife set up. This method of ionisation is defined as truly ambient due to it being able to acquire a mass spectrum of a species in the native state. An aerosol generated from evaporation of the sample is introduced to the mass spectrometer *via* an inlet allowing for the mass spectrometry profile to be observed.[2] Ionisation occurs *via* a localised thermal conduct to the surface of the sample. This rapid heating leads to precipitation of the proteins and metabolites within the sample, and boiling of the water causing formation of an evaporation plume.[3] This method of generating ions has since demonstrated its use in rapidly profiling a huge range of sample types. The original method of evaporation utilised surgical instruments, such as hand held forceps and surgical knives. These surgical methods have shown to be very useful in a range of applications such as; tissue identification[4] in surgery, food analysis[5], and identifying microcolonies.[6] Within the clinic the most efficient way of cell screening and drug testing, is using multiple well plates to analyse samples in bulk.[7] However, these surgical based methods are incompatible when it comes to analysing cell material within well plates due to the large size of the forceps, causing repeated burn events of material and even evaporation of the plastic of the well plate. Therefore a new laser based system was developed to allow for a streamlined method of analysis within the well plates. In this system, localised heating of the sample occurs *via* absorption of the laser energy by the water within the cellular material.[8]

Optimisation of sample preparation can allow for larger sample cohorts as well as more replicates being analysed in a practical amount of time. Applying this high throughput method to studies involving personalised medicine demonstrates a huge benefit. Currently, high throughput sequencing and personalised medicine is a very popular area of research, demonstrating the potential to sequence a patient's full clinical-pathological profile and

provide rapid information regarding the patient's genetic vulnerability, disease development, treatment response.[9] To allow for practicality and reduce cost limits per study, high throughput methods are crucial. As a result, optimisation of both the instrument set up, and cell culture workflow is essential. In order to create an optimised method for the analysis of cellular samples, a number of areas must be examined, including experimental, instrumentation, and sample preparation parameters. In order for the process to be streamlined from clinic to lab, it was important that preparation methods be as optimal as possible, allowing for a larger number of samples to be prepared for analysis. Thus, sample preparation steps in cell culture were examined to provide the most efficient method prior to REIMS analysis. Furthermore, it was important to test a variety of metabolites, with a range of *m/z* values to ensure that optimisation of the methods allowed for the comprehensive coverage of both smaller non-polar metabolites as well as larger multiple fatty acid chained lipid species. As a result, this paper describes a streamlined method for rapid analysis of cell based samples from clinic to instrument, incorporating a wide *m/z* window to allow for comprehensive metabolomics analysis.

3.3. Methods and Materials

3.3.1. Chemicals

All solvents, media, and reagents were purchased from Sigma-Aldrich (Poole, UK) unless otherwise stated. The solvents were of HPLC grade purity or higher.

3.3.2. Instrumentation

For this study, all experiments were performed on a Xevo G2-XS Q-ToF (Waters, UK) instrument equipped with a REIMS source containing a 20 cm inlet capillary with an

internal diameter of 0.7 mm. Following the inlet, the heated coil sits prior to the dual ion guide, which was heated to 900 ˚C, using a current of 3 A at 3.5 V. The laser system was the Opolette 2731 (Opotek, California) optical parametric oscillator (OPO), tuneable between 2.7 and 3.1µm, with a 200 µs pulse duration.

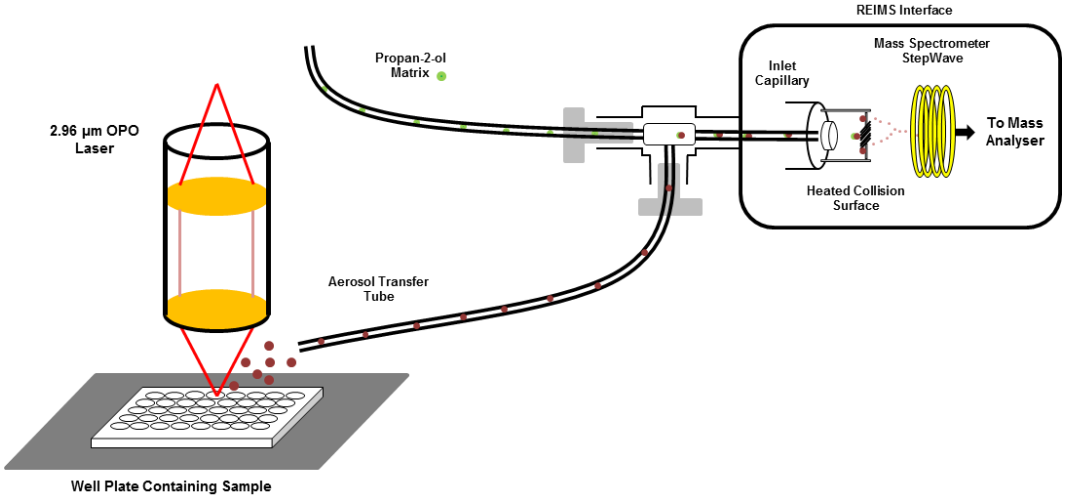

Figure 3.1: A schematic diagram of the laser REIMS system with the key features labelled.

Previous experimentation demonstrated the optimum setup used the OPO laser at 2.94 µm for relevant sample types.[10] Shown in the schematic, (Figure 3.1) the well plates were mounted on adapted an x-y-z stage (Thorlabs) with tubing connected to a Ventui pump for evacuation of the aerosol to the instrument inlet *via* nitrogen gas flow (2 bar, 20 L/min).

3.3.3. System Optimisation

Optimisation of the instrumental set up is crucial to ensure that the most information is being obtained from the sample in the shortest amount of time possible. It is imperative that not only the most information is being extracted, but that it is relevant and useful data for the sample study in question. As a result, a number of parameters were optimised for high throughput cell based analysis, including; laser power, dwell time, solvent flow, cone voltage and heater bias.

3.3.3.1.Laser Wavelength

Firstly, to ensure that the current laser system used is the ideal ablation source for cellular material, the laser wavelength was examined. Previous experiments demonstrate at 2.94 µm, this is the optimum wavelength for absorption of biological material due to the high absorption coefficient of water.[11]

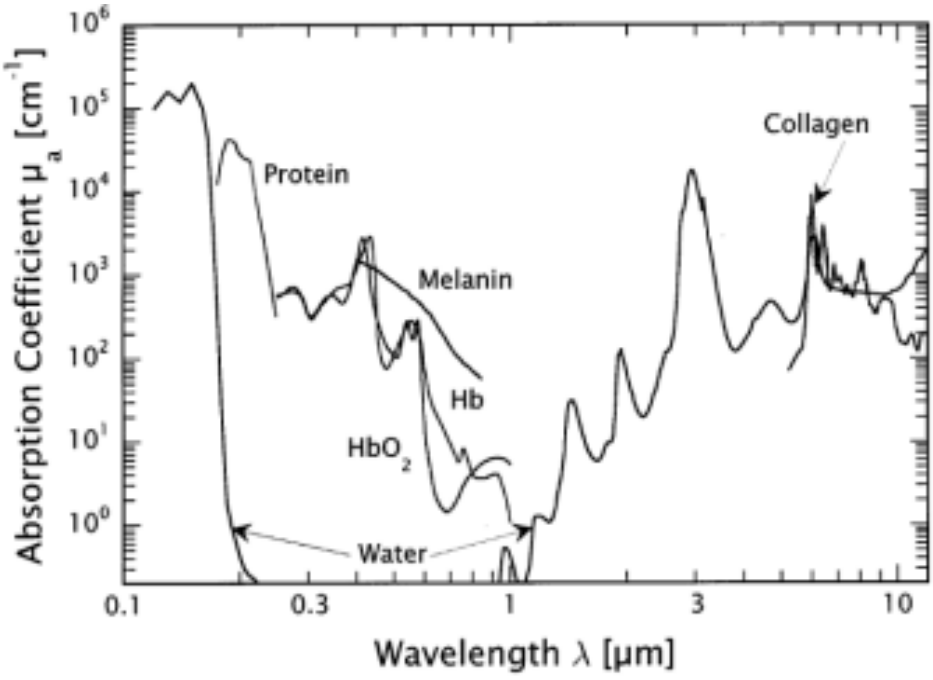

Figure 3.2: Optical absorption coefficients for the principal chromophores found in biological samples adapted from Vogel, A *et al* .[11]

At a wavelength of 2.94 µm, the power is sufficient to be able to create thermal fracturing and therefore ablation of the tissue (Figure 3.2). Human cell lines are typically composed of >70% water, making this an ideal wavelength for ablation.[12]

3.3.3.2.Laser Power

The higher the laser power, the more ablation is expected and thus, more signal. However, this is not necessarily a good thing. Higher laser powers can lead to increased fragmentation and breakdown of the analytes. As a result, this thermal degradation can

create contaminants which will dirty the instrument. Overall this causes two major results; contamination between samples, and instrument down time for cleaning and maintenance. As the overall goal of this study is to create a high throughput optimised method for analysis, this is not ideal. Therefore, the laser power was evaluated to yield the optimum balance of signal versus sample degradation.

3.3.3.3.Solvent Flow Rate

It has been demonstrated in literature that the addition of a matrix solvent to the REIMS system can increase the lipid signal from tissue samples by up to 3 orders of magnitude.[13] During the ionisation process, there is a breakdown in cell membranes causing a dispersion of phospholipid species. Due to the highly hydrophobic nature of these molecules, they form clustered macromolecules within the expelled droplets. Without the addition of a solvent, there is little chance of evaporation of these larger structures and they are therefore expelled as neutral clusters from the instrument. Introduction of a polar solvent like iso-propyl alcohol (IPA) helps dissolve the micelles and creates a better dispersion of charge across the lipid species. These smaller clusters can then hit the heated collision surface to help break these up further into individual charged lipids. This has all been theorised and proved for tissue work.[13] However, it is currently unknown if this will occur with cell suspensions as there is a differing water content. As a result, the addition of IPA at differing flow rates was examined to help optimise the overall workflow and increase the observed signal.

3.3.3.4.Cone Voltage and Heater Bias

After the addition of solvent, other parameters which aid the breakdown of larger clusters are the heater bias and cone voltage. The heater bias is a focusing voltage which provides a

potential offset between the collision surface and the front of the Stepwave whereas the cone voltage applies a bias across the Stepwave to the differential apature.[13] It has been previously discussed that for tissue samples, changing the heater bias voltage whilst using a solvent such as IPA to aid ionisation, has little effect.[13] Despite this, in order to explore this result with regard to cell material, these two parameters were adjusted to find the optimum set-up to allow for the highest signal to noise to be achieved.

3.3.4. Biological Samples

In order to fully explore the most efficient workflow for the analysis of cellular material, we must first start with the sample preparation. A range of cell population counts were tested to ensure that the best signal was obtained without pushing the boundaries of sample preparation. A typical cell count of approximately 5 million cells could be expected from one T75 flask. Anything above this value would need additional preparation steps therefore further risk of infection of the cells and can contribute to an increased cost per experiment. Accordingly, a range of cell counts from 100,000 to 12 million cells per plate were tested. The working volume of a 96 well plate ranges from 10 µl to 200 µl, thus a series of suspension volumes were tested (Table 3-1). This looked specifically at the reproducibility, chance of splash back and, rate of re-burn of material.

Table 3-1: Sample preparation optimisation parameters

Cell count / cells per 96 well plate	1e6	2e6	4e6	8e6	1.2e7
Suspension volume / µl	10	20	50	100	200

3.3.4.1.HeLa cell line

The samples used for this experiment were the HeLa cell line (ATCC) HeLa cells were derived from an aggressive adenocarcinoma of the cervix in 1951, and they are now known to be the most widely used cell line, globally.[14] The HeLa cell line is the standard cell line used in learning cell culture methods, as it is easy to culture and maintain. Due to the standardisation of this cell line and its thorough profiling, this cell line was selected to be used as a representation for all other potential cell lines as this cell line has been thoroughly examined using a variety of techniques.[15] This will allow for any results achieved to be compared to other more standard methods of analysis to ensure optimal set up of the REIMS system.

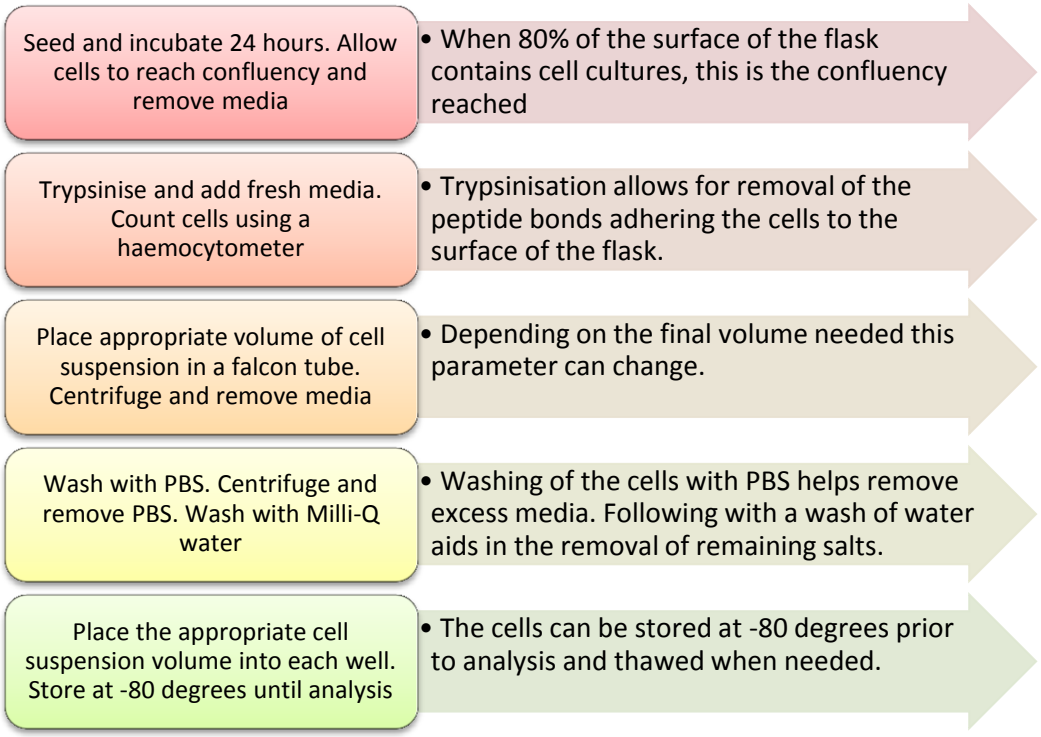

Figure 3.3: A schematic highlighting the key steps required for sample preparation.

As shown above (Figure 3.3), the standard workflow for cell culture based assays has multiple steps each of which increase the chance for contamination. Therefore it is vital to examine the workflow to ensure this can be kept as simple as possible. This will not only improve the overall workflow, it will also help to reduce overall costs. For this study, HeLa cells were initially cultured into T75 flasks, the larger cell numbers required more flasks to reach the appropriate cell count. When 80% confluency was reached, the cells were trypsinised and counted using a haemocytometer. The selected cell count was added to a corresponding labelled falcon tube containing medium (5 mL, RPMI 10% FCS) and centrifuged (5 minutes, 15,000 RPM). The resultant supernatant was decanted and the pellet was resuspended in PBS (1x, 5 mL). This solution was centrifuged again and once more the supernatant decanted. Finally, an appropriate volume of deionised water (MilliQ Millipore) was added and the cells suspended. To each corresponding 96 well plate, the appropriate cell count and suspension volume was added. Each well plate was then placed into a -80^{o}C freezer and stored prior to analysis.

3.3.4.2.LNCaP Cell Line

In order to test the developed optimisation method, it is imperative to use a different cell line to ensure that this protocol can be transferred to a range of cell types. As a result, the LNCaP cell line was cultured using the optimised protocol determined from this study. The LNCaP cell line was derived from a needle biopsy from a patient suffering with lymph node adenocarcinoma of the prostate.[16] This cell line is a slightly smaller in suspension than the HeLa cell, 18 µm compared to ~25 µm,[17] and thus provides information on how differing cell lines respond to this method, despite differing characteristics.

3.3.5. Metabolite Analysis

Although this work is targeted towards lipidomics experiments, it is also important to ensure this optimisation enables detection of a large molecular coverage. Integrated methods, such as lipidomics and metabolomics, offer a complete overview of the downstream mechanisms driving disease progression.[18] Amino acid species are the building blocks of biological samples and using these molecules we can look at the downstream interactions for the amino acid metabolism. These species have a range of biochemistries and differing characteristics which makes it a useful target to validate the ability to explore a large molecular range with this optimised method. As a result, using a standard amino acid mix, the intensities of each amino acid was studied, both pure and mixed into a biological matrix.

3.3.6. Data analysis

For each parameter optimised, a minimum of 4 burn events were used to allow for reproducibility information and error bars to be calculated using standard deviation. Each of the chromatograms produced by each burn was introduced to the abstract model builder software (Waters Corp, Hungary) allowing for each to be labelled accordingly. From this, the data matrix from *m/z* 50 - 1200 was exported to a .csv file. This was then imported to the Spectrum Quality Analyser (Waters Research Center, Budapest). This software determined the signal to noise ratio (S/N) to be calculated for the top 20 peaks for each sample. The signal was defined by the average of the top 20 peaks in the lipid mass range (600-900) for each sample. The noise was calculated by taking an array of points within the defined region (*m/z* 50 – 1200) every 50 Da which did not constitute a peak, and then the median of these values described the noise value. This data was then exported into Excel and the average S/N for each sample set was calculated, with the standard deviation being

used for the calculation of error bars. All plots were then created using the GraphPad Prism 8.3 software (GraphPad Software, La Jolla California USA).

3.4. Results and Discussion

3.4.1. Instrumentation and Experimental Parameter Optimisation

3.4.1.1.LASER power

The laser power was altered to observe the changes in S/N as a function of this parameter.

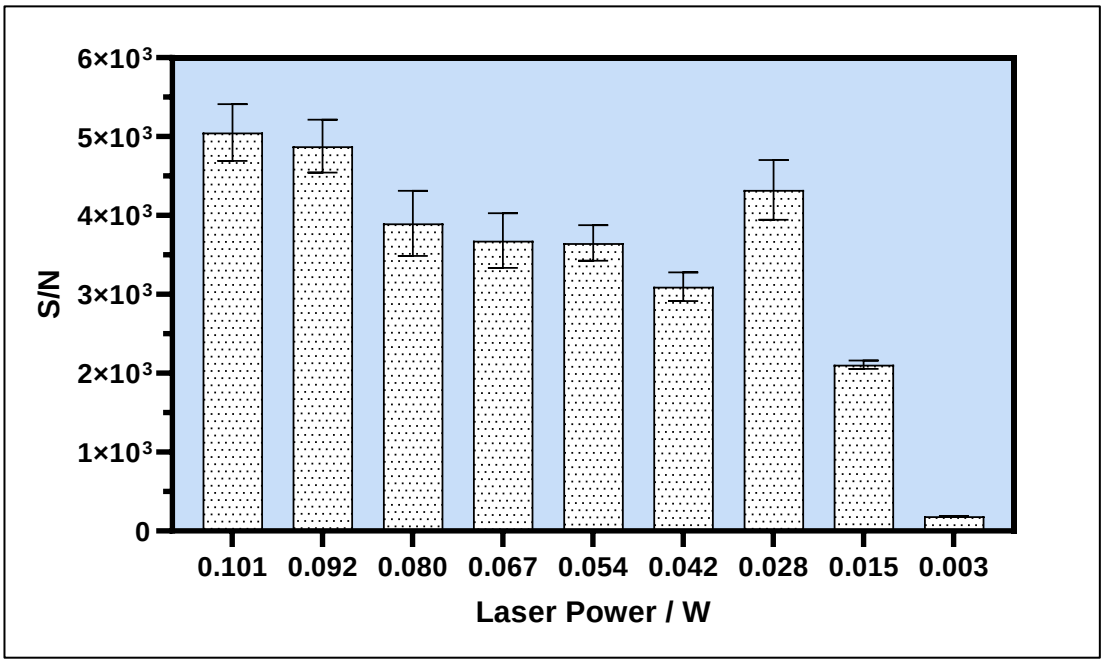

Figure 3.4: A plot showing the S/N acquired from the biological material from HeLa cells as a response to changing laser power. This data was acquired on the Xevo G2-SX using a LASER REIMS ionisation source.

The trend for the change in S/N as the laser power is changed, is mostly as expected (Figure 3.4). An overall decrease in the observed signal and the S/N is seen as the laser power is decreased. However, At 0.003 W, a large drop in intensity is witnessed.

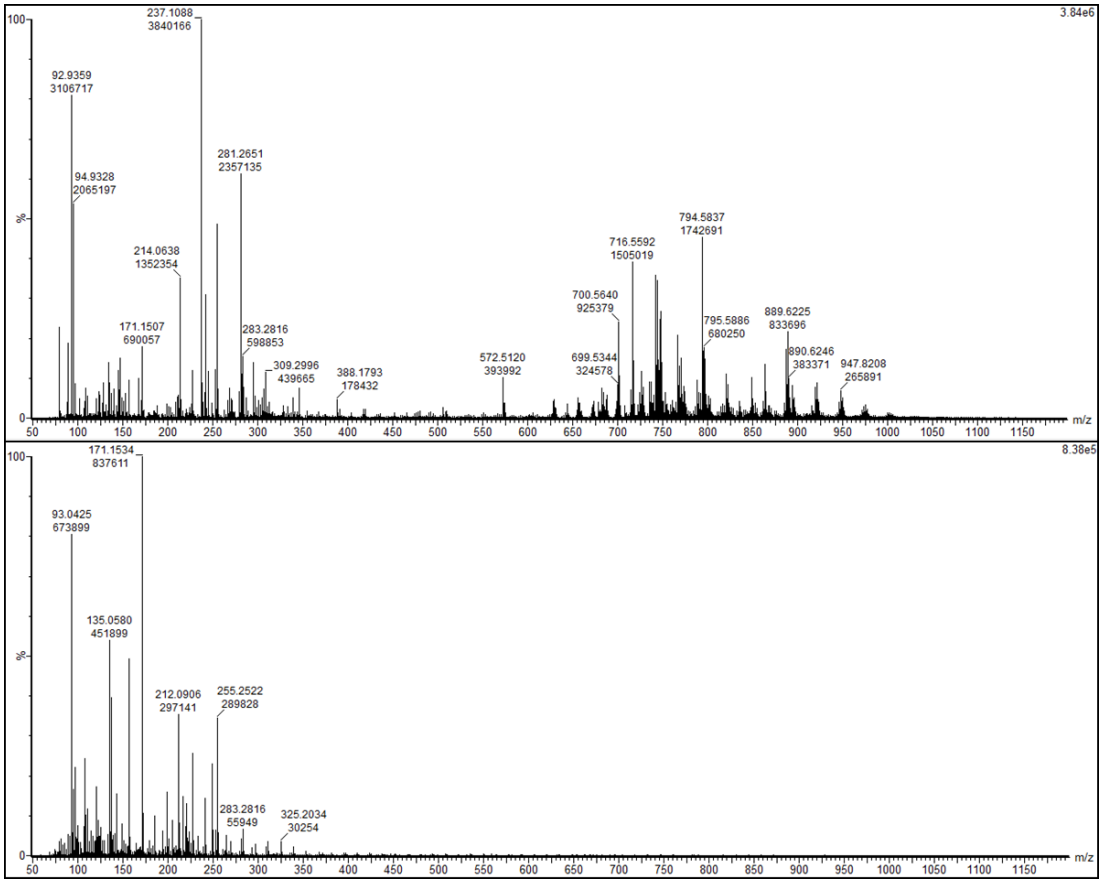

Figure 3.5: Background removed average spectra showing the highest and lowest laser power of 0.101 and 0.003 W. The data was acquired on the Xevo G2-SX using a LASER REIMS ionisation source in negative mode.

This is as a result of the activation threshold being reached. This is the energy in which there is not enough heat being dissipated from the laser to form droplets. This is emphasized when looking at the spectra shown, Figure 3.5. There is no signal observed for the lower limit of laser power other than the background and noise. This is also shown by the chromatogram as there are no peaks for each burn event created (supplementary, Figure 3.19). As shown on the plot (Figure 3.4), there appears to be a local maximum observed at a laser power of 0.028 W. To ensure this wasn't an outlier, the raw data was inspected.

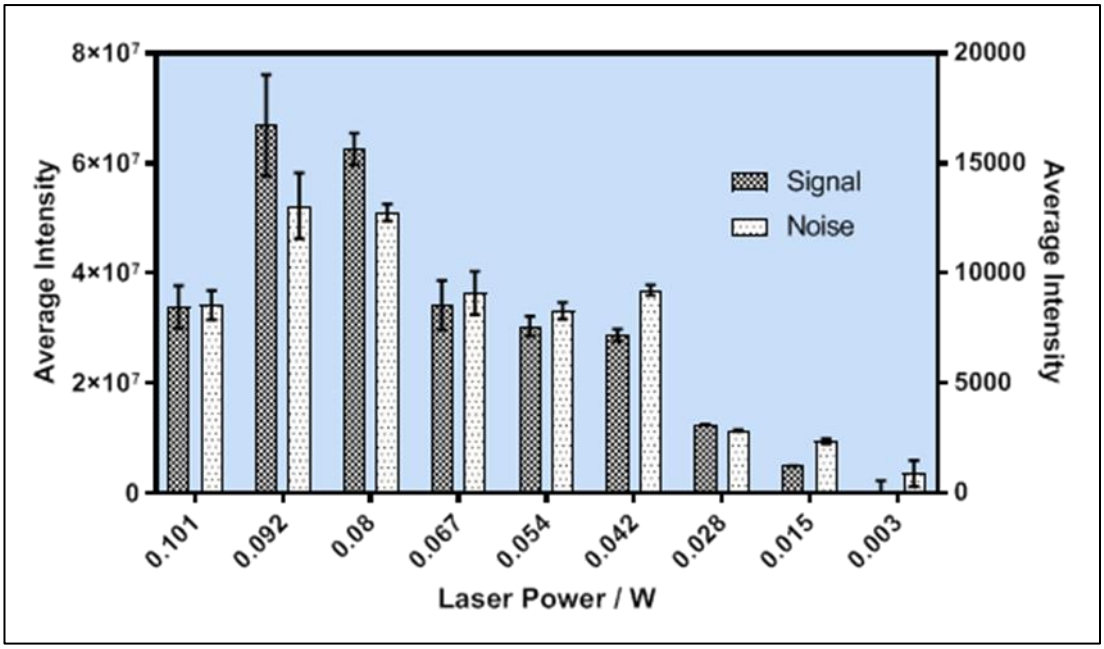

Figure 3.6: The comparison between the average signal using the left hand Y axis, and the noise intensities, using the right hand Y axis, for the selected laser powers.

Looking at the raw data (Figure 3.6), the signal at 0.028 W has an overall lower background than is exhibited with the lower end of the laser power. However, the signal is only slightly diminished as a result of the decreasing laser power. So although for this laser power, the overall signal is lower, the background is lower than the average therefore you observe a local maximum of S/N. Although this is beneficial, it is also important to explore each laser power further to ensure the ablation observed is of intact molecules rather than an increased fragmentation and loss of species due to thermal degradation. It was postulated that a higher laser power could lead to an overall increase in fragmentation therefore a comparison of the average intensity of a series of common fragment species was compared to the signal from a lipid species (PC(16:0/18:1), 794.58), supplementary; Table 3-4.

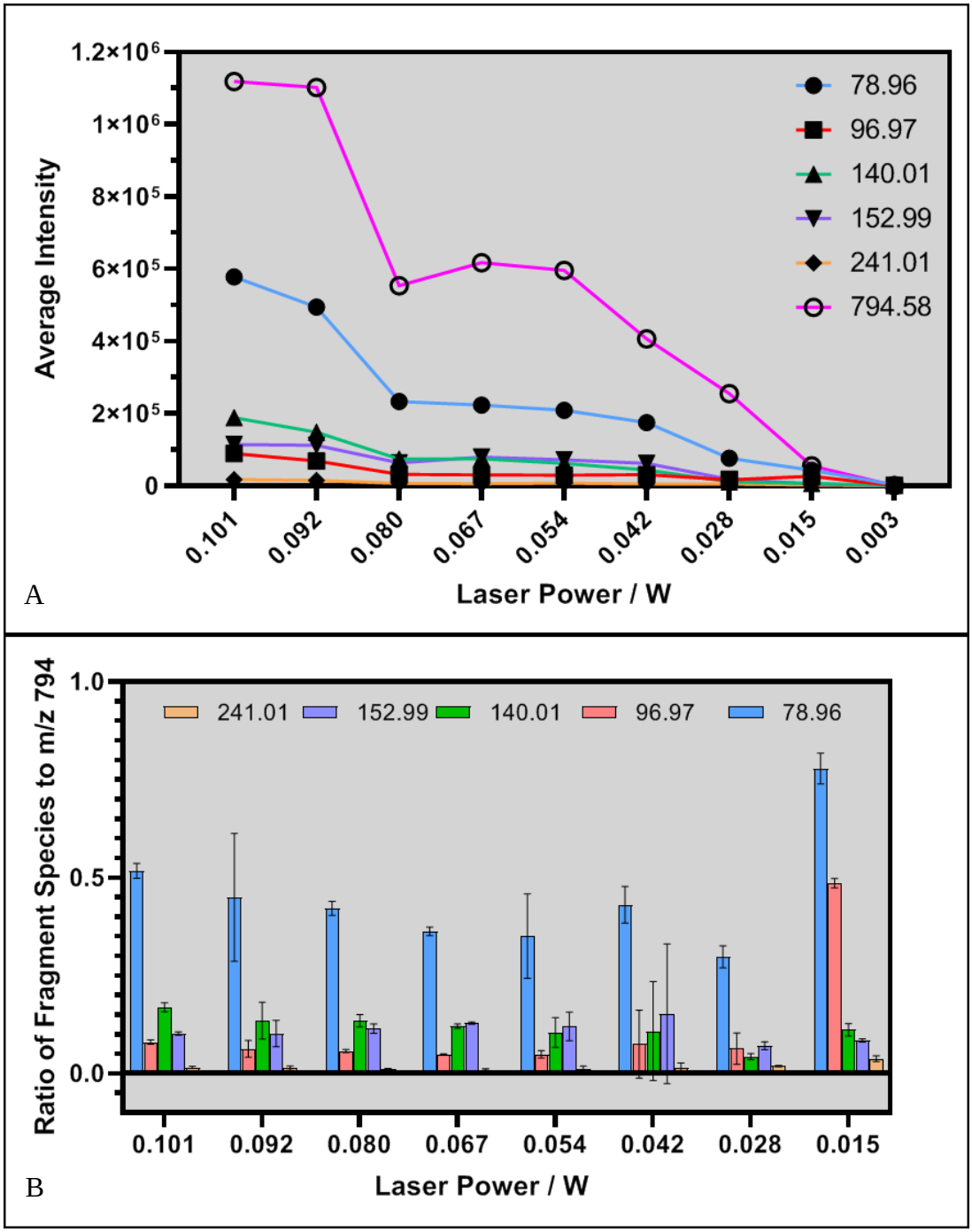

Figure 3.7: A shows the average intensity for each of the species involved for each selected laser power. B is a graphical representation of the ratio of the average signal of each of the fragment species to the average intensity of the lipid species (PC(16:0/18:1), *m/z* 794.58) at each laser power. The data was collected in negative mode on the Xevo G2-SX using a LASER REIMS ionisation source.

At higher laser powers, a high signal for the lipid species is observed. However, there is also large amounts of fragmentation (Figure 3.7, A). As the laser power is decreased, the overall trend of signal from both the fragmentation and the intact lipid decreases.

On the other hand, looking at the ratio between the average intact lipid signal and that of the each fragment (Figure 3.7, B) you can see that at 0.028 W, the lowest ratio is observed. Therefore demonstrating, at this laser power, the highest signal to the lowest fragmentation is acquired. As a result, 0.028 W was the selected laser power.

3.4.1.2.Dwell Time

Dwell time is defined as the time period that the laser is applied within each well for analysis of the sample. It is important to select a dwell time that can provide the most information without increasing the experimental time too greatly.

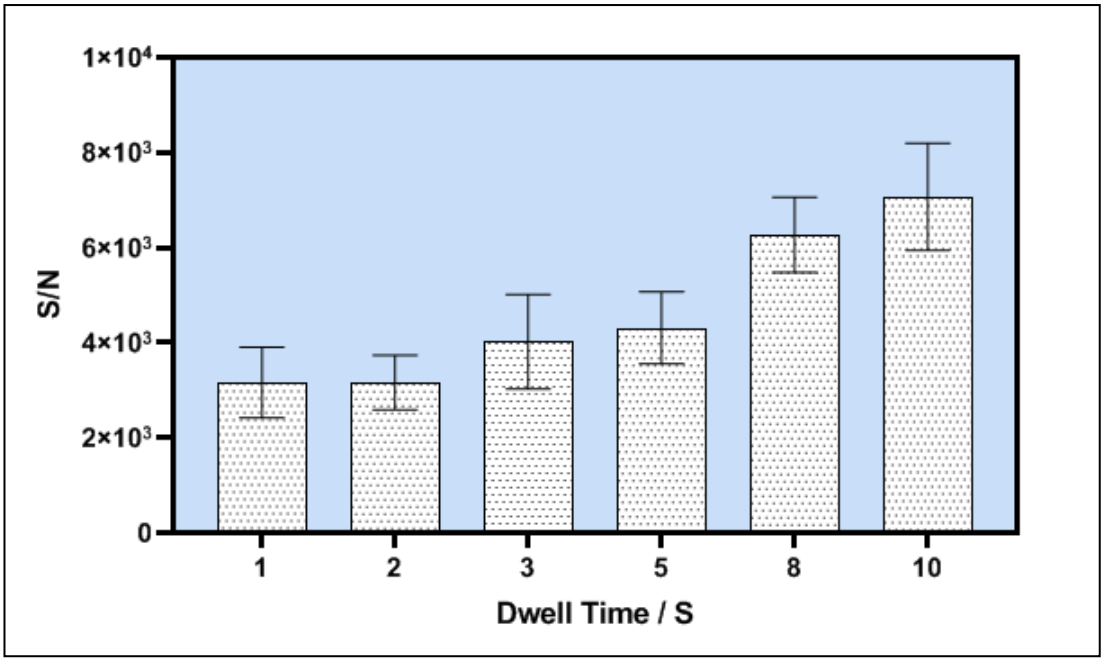

Figure 3.8: A plot showing the S/N acquired from the biological material from HeLa cells as a response to changing dwell time. This data was acquired on the Xevo G2-SX using a LASER REIMS ionisation source.

The above plot (Figure 3.8) follows the trend that the S/N is proportional to the increasing dwell time. Although at 10 second dwell time, the S/N is the highest, upon evaluation of the well post analysis, this prolonged dwell time causes damage to the plastic casing of the well for some of the lower volume cell suspensions, as observed by a physical burn. This may result in ions from the plastic being present in the spectra (Supplementary; Figure

3.19). It was also considered that above 5 seconds analysis of each well, would significantly increase the experiment time, which for large sample sets can drastically decrease the overall turnaround. It also must be taken into consideration, that longer dwell times cause significantly more splash, which will dirty lenses and create a potential for sample contamination and carry over. As a result, higher dwell times will lead to more frequent insturment cleaning and therefore longer downtimes. As we are focusing on rapid analysis, the selected dwell times for the remaining experiements was set to either 3 or 5 seconds, depending on the sample depth. This will be explored in greater detail later in the next section.

3.4.1.3.IPA Solvent Flow

It has been demonstrated previously in literature that having a solvent such as iso-propyl alcohol (IPA) co-aspirated with the sample aids in ionisation of the lipid species. As a result, the flow rate of IPA was examined to ensure the highest S/N was achieved.

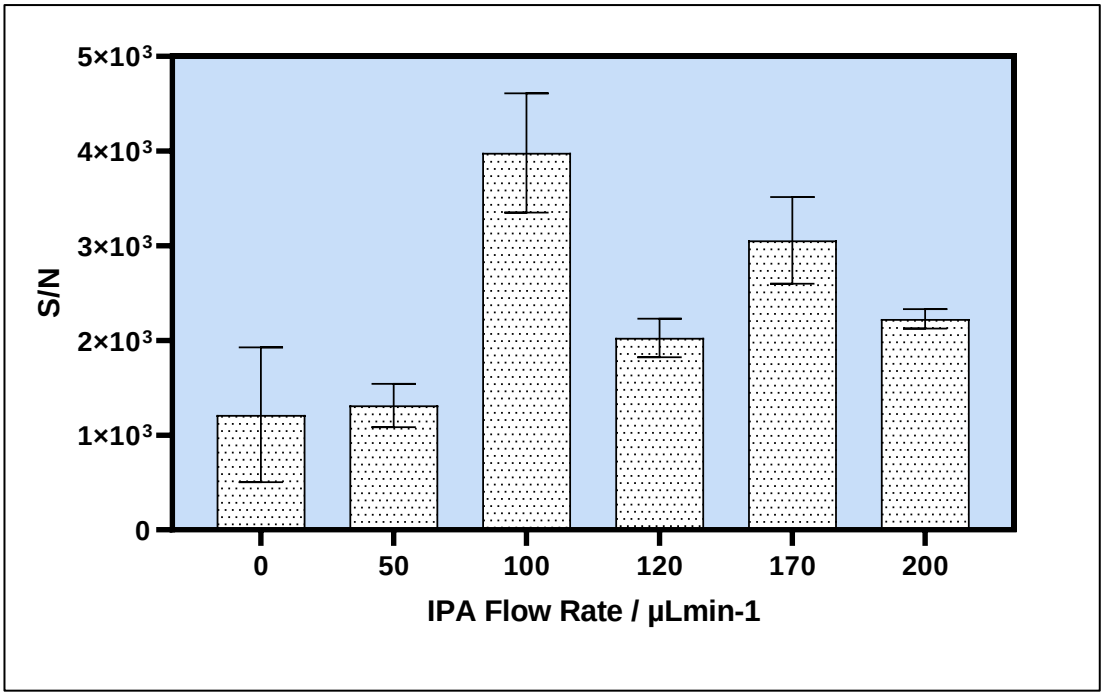

Figure 3.9: A plot showing the S/N acquired from the biological material from HeLa cells as a response to IPA solvent flow. This data was acquired on the Xevo G2-SX using a LASER REIMS ionisation source.

Based on the graph (Figure 3.9), the IPA flow rates that yield the highest S/N values are 100 and 170 µL/min. The flow rate of solvent can also aid in keeping the inlet cap clean and can prevent carry over. Therefore a higher flow rate is more preferable to ensure cleaner lines and less instrument downtime for cleaning and maintenance. Also, at higher flow rates, the aerosolisation effect of the IPA is more reproducible. At lower flow rates, or no IPA, the overall S/N is much more variable as observed by the error bar.

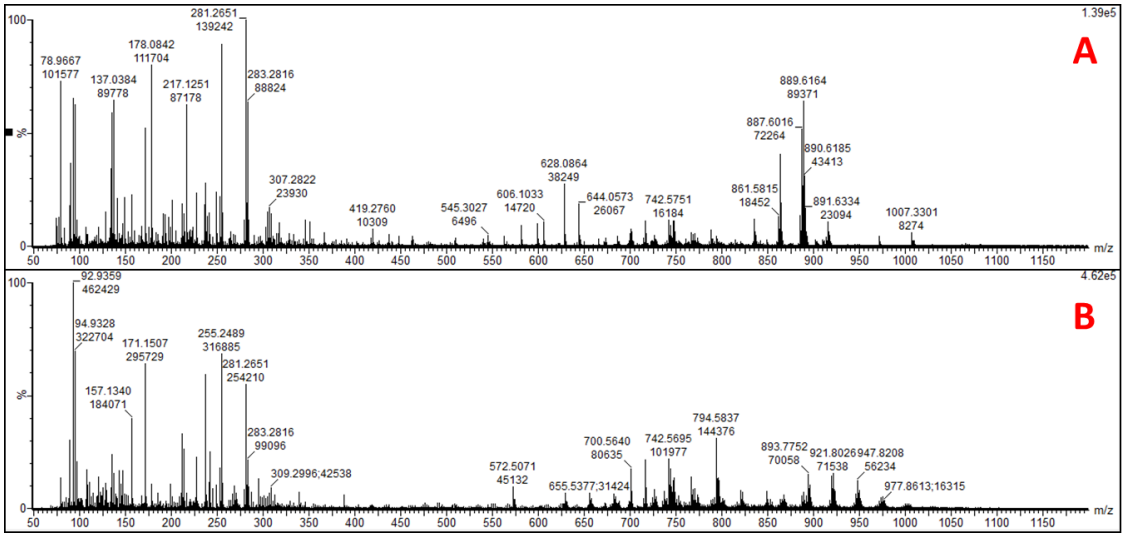

Figure 3.10: A is the average mass spectrum for no IPA present. B shows the average spectrum for 200 µL/min flow rate. Each spectrum is negative mode acquired on the Xevo G2-SX using a LASER REIMS ionisation source.

When there is no IPA present, as observed above (Figure 3.10), signal is still observed, however, the typical lipid species, such as *m/z* 794, that have been seen throughout are now not visible through the noise. This highlights the need of a solvent to aid in the ionisation of a number of lipids. Therefore, to ensure a good compromise between signal and downtime of the instrument, despite the 100 µL/min flow rate giving a higher overall signal, the addition considerations demonstrate that the higher flow rate of 170 µL/min is more favourable. Future work will study this effect in more detail, aiming to explore the lipid groups changing with the addition of solvent.

3.4.1.4.Cone Voltage versus Heater Bias

The cone voltage and heater bias further aid in the breakdown of the clusters generated from the droplets, it is therefore important to examine these parameters.

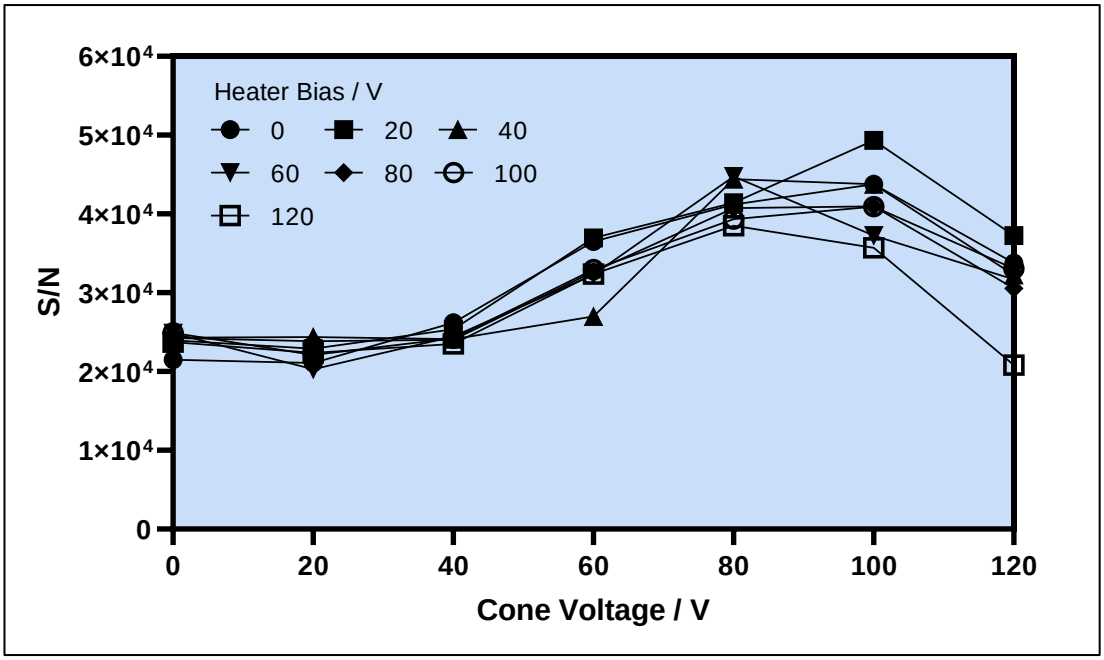

Figure 3.11: A plot showing the S/N acquired from the biological material from HeLa cells as a response to changing the cone voltage versus the heater bias. This data was acquired on the Xevo G2-SX using a LASER REIMS ionisation source.

It is evident from the data (Figure 3.11) that the heater bias does not change the S/N significantly for cell material. This can be explained by the hypothesis that once the IPA is in the system, the solvent does the job of declustering that would have been performed by the heater bias, therefore, with the presence of IPA, changing this voltage doesn't affect the overall S/N. Nonetheless, what is clear is that there is a maximum observed at a cone voltage at 100 V. Hence, this was the selected voltage applied to all further experiments.

3.4.2. Cell Culture Parameters

In order to maintain a high throughput approach to this work, it is also important to ensure rapid sample preparation allowing for the highest S/N to be achieved during analysis. Therefore as a result, a variety of sample preparation methods, from cell suspension volume to overall cell count, were explored using the laser REIMS system to ensure optimisation of the selected sample preparation method.

3.4.2.1.Cell Suspension volumes

The suspension volumes are vital in achieving rapid throughput. For this experiment, the multichannel pipettes available ranged from 50 – 200 µL. This enables a rapid turnover of sample preparation, as well as consistency throughout pipetting. However, larger cell suspensions risk a diluting effect on analysis of the cells. As a result, a variety of volumes were examined, from 10 – 200 µL.

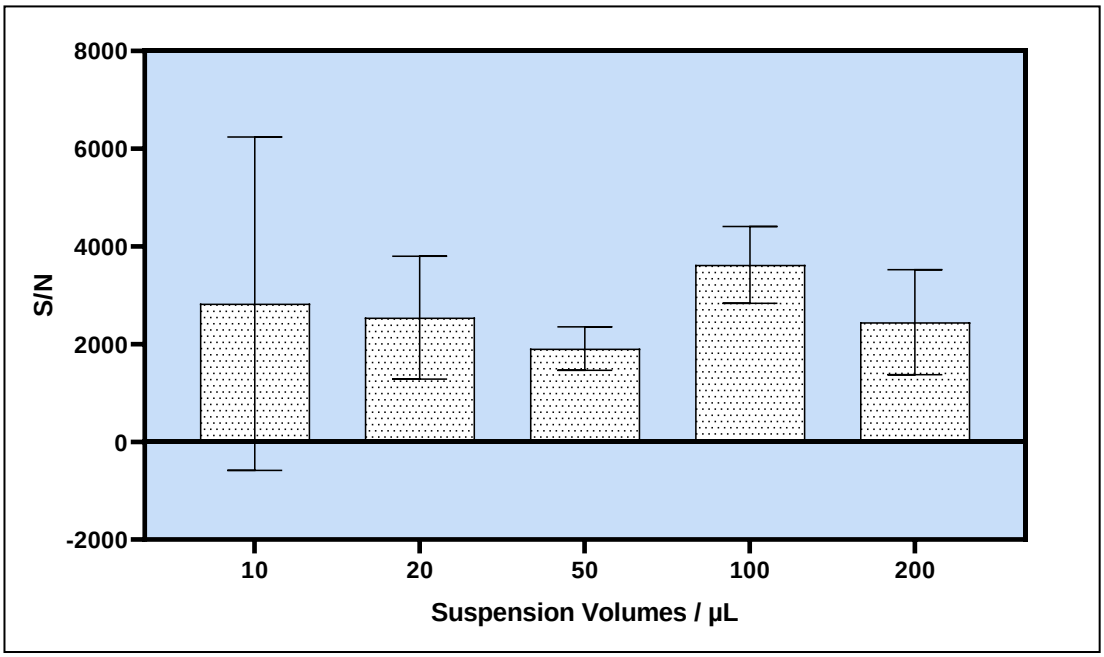

Figure 3.12: A plot showing the S/N acquired from the biological material from HeLa cells as a response to changing the suspension volume of water. This data was acquired on the Xevo G2-SX using a LASER REIMS ionisation source in negative mode.

As immediately observed by the error bars above (Figure 3.12), volumes below 50 µL are much more variable. At these volumes, multichannel pipetting was not an option; therefore each well was filled individually, resulting in increased inconsistency due to human error. Also, due to the low volumes, there is no guarantee of full coverage on the bottom of the plate. Therefore, it was decided that the acceptable volumes for use would be from 100 – 200 µL of cell suspension per well. As mentioned earlier, the dwell time would depend on the cell suspension volume. As a result, both 3 and 5 s dwell times were

tested for the selected volumes. It was determined that for 3 and 5 second dwell times, 100 µL and 200 µL suspension volumes were optimal, respectively.

3.4.2.2.Cell Count

Cell counting is a vital step in a lot of cell based assays so ensure that there is consistency within the assays and ensure there is an appropriate measure of material to achieve the results needed.

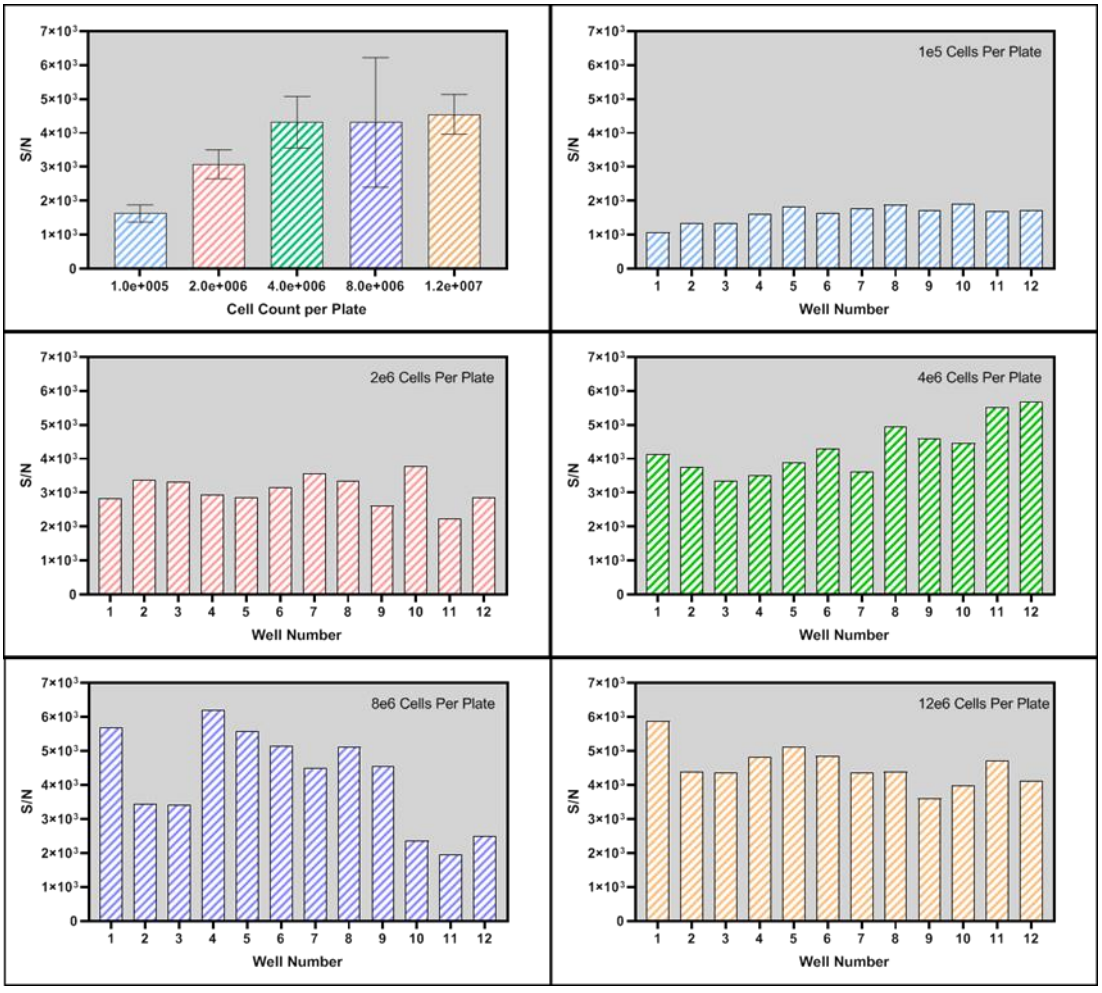

Figure 3.13: (A) the average signal to noise for each of the selected cell counts for all 12 wells, (B)-(F) the individual acquired signal to noise for each well for the selected cell count. This data was acquired on the Xevo G2-SX using a LASER REIMS ionisation source in negative mode.

As observed from the above graphs (Figure 3.13), it is immediately clear that from a cell count of 4 x 10^6 and above the S/N does not change significantly. The data demonstrates

that it is possible to get sufficient information from 4 million cells per well and above. The overall signal intensity does not increase enough to justify the additional work and cost to achieve the higher cell counts. However, it is important to look at the overall reproducibility for each cell count. Therefore, in order to maintain a high throughput workflow with the best reproducibility, it was determined that the cell count best suited for this application was 4 x 10^6 cells per 96 well plate.

3.5. Metabolite Analysis

The above study has demonstrated the most appropriate Laser-REIMS method for analysis of lipids from cell suspension samples. This is highly beneficial for lipidomics research. However, it is common for the lipid data to be applied to biological pathways, in which case information from small molecule metabolite species would also be valuable. Using this optimised method, common small metabolite amino acid species were examined to ensure a large molecular coverage could be extracted using this workflow.

Table 3-2: A table showing the amino acids analysed and the stock concentration, highlighting the *m/z* value observed and the corresponding adduct.

Amino Acid	Concentration	*m/z*	Adduct
L-Alanine	2.50 µM	89.0621	$[M+H]^+$
L-Asparagine	2.50 µM	132.059	$[M+H]^+$
L-Cysteine	1.25 µM	148.0777	$[M+H]^+$
L-Glutamine	2.50 µM	146.0778	$[M+H]^+$
L-Histidine	2.50 µM	155.0988	$[M+H]^+$
L-Leucine	2.50 µM	131.1097	$[M+H]^+$
L-Lysine	2.50 µM	146.11	$[M+H]^+$
L-Serine	2.50 µM	105.0605	$[M+H]^+$
L-Threonine	2.50 µM	119.0779	$[M+H]^+$
L-Tyrosine	2.50 µM	181.1103	$[M+H]^+$
L-Valine	2.50 µM	117.0435	$[M+H]^+$

Using a standard mix of amino acids (AA), the *m/z* values observed in the raw mix were measured (Table 3-2). Thus far, the sample was introduced at concentrations of 1.25 µM and above into the instrument, but most metabolites will be in much lower concentrations within the biological sample. As a result, a dilution series was run to explore this further.

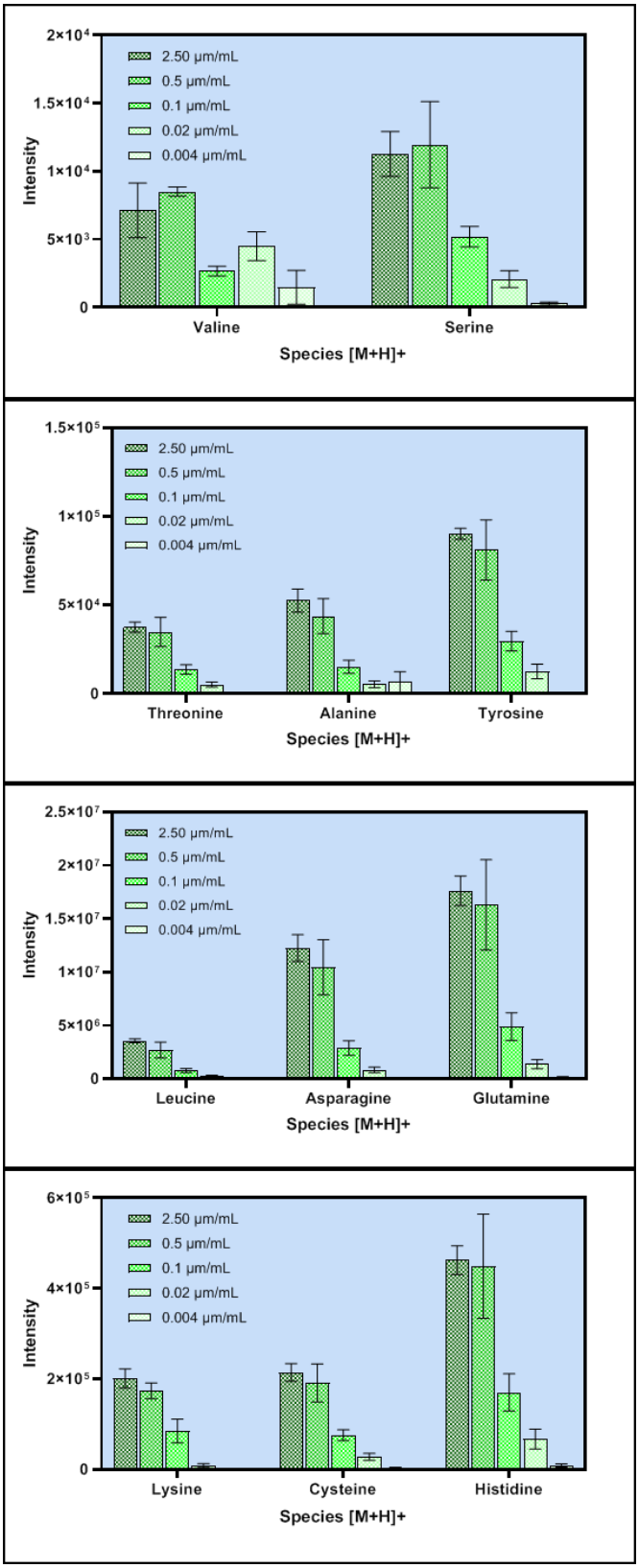

Figure 3.14: A series of graphs showing the observed intensity for each amino acid at a range of concentrations. This data was acquired on the Xevo G2-SX using a LASER REIMS ionisation source in negative mode.

The overall trend observed, followed the expected, in which decreasing concentrations decreases the overall signal observed (Figure 3.14). For most species, the signal is still observable down to the minimum range of 0.004 µM. However, in looking at the raw spectra, the overall signal is very low, and therefore each burn event is hard to distinguish in the chromatogram. (Supplementary; Figure 3.18, Figure 3.20). Therefore, data has demonstrated that the majority of the listed amino acids are visible using REIMS down to concentrations of 0.02 µM. Consequently, amino acid analysis by laser REIMS should be observable within a biological matrix.

3.5.1. LNCaP cell line analysis

These optimised parameters were applied and tested using a different cell line, LNCaP (Figure 3.15).

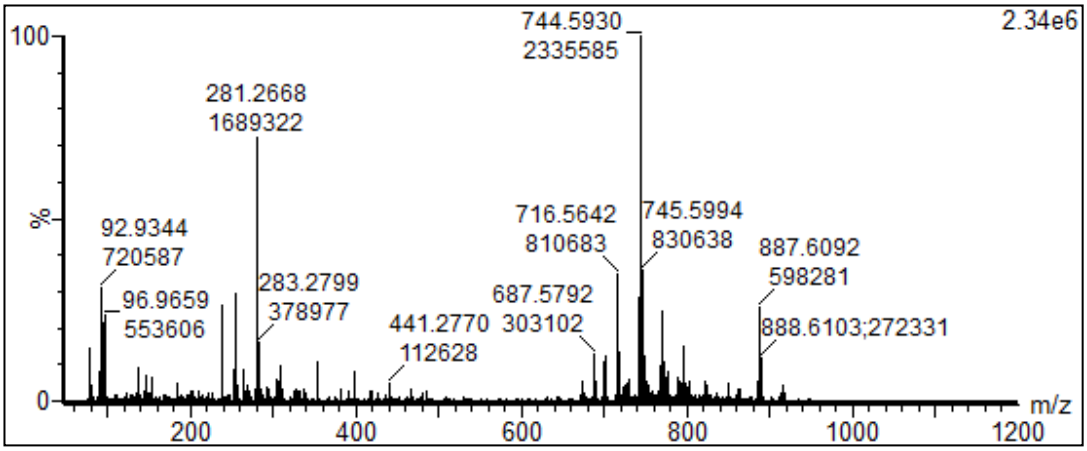

Figure 3.15: A spectrum for the mass range *m/z* 50-1200 for the LNCaP cell line using the optimised parameters as discussed by this paper. This data was acquired on the Xevo G2-SX using a LASER REIMS ionisation source in negative mode.

Figure 3.15 clearly highlights that this protocol is adaptable to more than one cell line. The data was acquired with minimal sample preparation and with rapid analysis time, of approximately 8 minutes per 96 well plate. As observed, it is also useful for both lipidomics and metabolomic approaches due to the presence of amino acid small molecule species.

3.6. Conclusion

This paper reports a study of sample preparation and instrumental parameters for the optimised Laser-REIMS analysis of cell lines (Table 3-3). This work has demonstrated that optimisation of both the sample and analytical workflow is vital to ensure a rapid and streamlined approach to REIMS experimentation.

Table 3-3: A table demonstrating the key parameters optimised

Parameter	Optimised Value
Laser power	0.028 W
IPA Flow Rate	170 µL/min
Dwell Time	3 second
Cone Voltage	100 V
Suspension Volume	100 µL
Cell Count	4 million cells per plate

Optimisation aided in a number of aspects, including reduction of; cost, instrument down time, and time required for analysis per study. By targeting a number of areas of the system, the overall signal to noise acquired is optimal for cell samples. It has also been demonstrated that due to the large molecular coverage, analysis of smaller metabolite species is a possibility, enabling integrated 'omics' approaches.

3.7. Acknowledgments

The author acknowledges and gives thanks for the work and services provided by the following departments

- EPSRC and Waters for funding of a studentship to DM
- ToF-SIMS instrument EPSRC grant EP/S019863/1

3.8. References

(1) Schäfer, K.-C.; Dénes, J.; Albrecht, K.; Szaniszló, T.; Balog, J.; Skoumal, R.; Katona, M.; Tóth, M.; Balogh, L.; Takáts, Z. In Vivo, In Situ Tissue Analysis Using Rapid Evaporative Ionization Mass Spectrometry. *Angew. Chem. Int. Ed.* **2009**, *48* (44), 8240–8242. https://doi.org/10.1002/anie.200902546.

(2) Balog, J.; Szaniszlo, T.; Schaefer, K.-C.; Denes, J.; Lopata, A.; Godorhazy, L.; Szalay, D.; Balogh, L.; Sasi-Szabo, L.; Toth, M.; Takats, Z. Identification of Biological Tissues by Rapid Evaporative Ionization Mass Spectrometry. *Anal. Chem.* **2010**, *82* (17), 7343–7350. https://doi.org/10.1021/ac101283x.

(3) Tzafetas, M.; Mitra, A.; Paraskevaidi, M.; Bodai, Z.; Kalliala, I.; Bowden, S.; Lathouras, K.; Rosini, F.; Szasz, M.; Savage, A.; Balog, J.; McKenzie, J.; Lyons, D.; Bennett, P.; MacIntyre, D.; Ghaem-Maghami, S.; Takats, Z.; Kyrgiou, M. The Intelligent Knife (IKnife) and Its Intraoperative Diagnostic Advantage for the Treatment of Cervical Disease. *Proc. Natl. Acad. Sci.* **2020**, *117* (13), 7338–7346. https://doi.org/10.1073/pnas.1916960117.

(4) Balog, J.; Sasi-Szabó, L.; Kinross, J.; Lewis, M. R.; Muirhead, L. J.; Veselkov, K.; Mirnezami, R.; Dezs\Ho, B.; Damjanovich, L.; Darzi, A.; others. Intraoperative Tissue Identification Using Rapid Evaporative Ionization Mass Spectrometry. *Sci. Transl. Med.* **2013**, *5* (194), 194ra93–194ra93.

(5) Identification of the Species of Origin for Meat Products by Rapid Evaporative Ionization Mass Spectrometry | Journal of Agricultural and Food Chemistry https://pubs.acs.org/doi/abs/10.1021/acs.jafc.6b01041 (accessed Feb 10, 2020).

(6) Characterization and Identification of Clinically Relevant Microorganisms Using Rapid Evaporative Ionization Mass Spectrometry | Analytical Chemistry https://pubs.acs.org/doi/pdf/10.1021/ac501075f (accessed Feb 10, 2020).

(7) Jones, E.; Michael, S.; Sittampalam, G. S. Basics of Assay Equipment and Instrumentation for High Throughput Screening. In *Assay Guidance Manual*; Sittampalam, G. S., Grossman, A., Brimacombe, K., Arkin, M., Auld, D., Austin, C. P., Baell, J., Bejcek, B., Caaveiro, J. M. M., Chung, T. D. Y., Coussens, N. P., Dahlin, J. L., Devanaryan, V., Foley, T. L., Glicksman, M., Hall, M. D., Haas, J. V., Hoare, S. R. J., Inglese, J., Iversen, P. W., Kahl, S. D., Kales, S. C., Kirshner, S., Lal-Nag, M., Li, Z., McGee, J., McManus, O., Riss, T., Saradjian, P., Trask, O. J., Weidner, J. R., Wildey, M. J., Xia, M., Xu, X., Eds.; Eli Lilly & Company and the National Center for Advancing Translational Sciences: Bethesda (MD), 2004.

(8) Schäfer, K.-C.; Szaniszló, T.; Günther, S.; Balog, J.; Dénes, J.; Keserű, M.; Dezső, B.; Tóth, M.; Spengler, B.; Takáts, Z. In Situ, Real-Time Identification of Biological Tissues by Ultraviolet and Infrared Laser Desorption Ionization Mass Spectrometry. *Anal. Chem.* **2011**, *83* (5), 1632–1640. https://doi.org/10.1021/ac102613m.

(9) Lightbody, G.; Haberland, V.; Browne, F.; Taggart, L.; Zheng, H.; Parkes, E.; Blayney, J. K. Review of Applications of High-Throughput Sequencing in Personalized Medicine: Barriers and Facilitators of Future Progress in Research and Clinical Application. *Brief. Bioinform.* **2019**, *20* (5), 1795–1811. https://doi.org/10.1093/bib/bby051.

(10) Fatou, B.; Saudemont, P.; Leblanc, E.; Vinatier, D.; Mesdag, V.; Wisztorski, M.; Focsa, C.; Salzet, M.; Ziskind, M.; Fournier, I. In Vivo Real-Time Mass Spectrometry for Guided Surgery Application. *Sci. Rep.* **2016**, *6* (1), 1–14. https://doi.org/10.1038/srep25919.

(11) Vogel, A.; Venugopalan, V. Mechanisms of Pulsed Laser Ablation of Biological Tissues. *Chem. Rev.* **2003**, *103* (2), 577–644. https://doi.org/10.1021/cr010379n.

(12) Cooper, G. M. The Molecular Composition of Cells. *Cell Mol. Approach 2nd Ed.* **2000**.

(13) Jones, E. A.; Simon, D.; Karancsi, T.; Balog, J.; Pringle, S. D.; Takats, Z. Matrix Assisted Rapid Evaporative Ionization Mass Spectrometry. *Anal. Chem.* **2019**, *91* (15), 9784–9791. https://doi.org/10.1021/acs.analchem.9b01441.

(14) Lucey, B. P.; Nelson-Rees, W. A.; Hutchins, G. M. Henrietta Lacks, HeLa Cells, and Cell Culture Contamination. *Arch. Pathol. Lab. Med.* **2009**, *133* (9), 1463–1467. https://doi.org/10.1043/1543-2165-133.9.1463.

(15) Jeucken, A.; Brouwers, J. F. High-Throughput Screening of Lipidomic Adaptations in Cultured Cells. *Biomolecules* **2019**, *9* (2). https://doi.org/10.3390/biom9020042.

(16) Horoszewicz, J. S.; Leong, S. S.; Kawinski, E.; Karr, J. P.; Rosenthal, H.; Chu, T. M.; Mirand, E. A.; Murphy, G. P. LNCaP Model of Human Prostatic Carcinoma. *Cancer Res.* **1983**, *43* (4), 1809–1818.

(17) Park, S.; Ang, R. R.; Duffy, S. P.; Bazov, J.; Chi, K. N.; Black, P. C.; Ma, H. Morphological Differences between Circulating Tumor Cells from Prostate Cancer Patients and Cultured Prostate Cancer Cells. *PLoS ONE* **2014**, *9* (1). https://doi.org/10.1371/journal.pone.0085264.

(18) Wang, R.; Li, B.; Lam, S. M.; Shui, G. Integration of Lipidomics and Metabolomics for In-Depth Understanding of Cellular Mechanism and Disease Progression | Elsevier Enhanced Reader. *J. Genet. Genomics* **2019**, *47*, 69–83. https://doi.org/10.1016/j.jgg.2019.11.009.

3.9. Supplementary

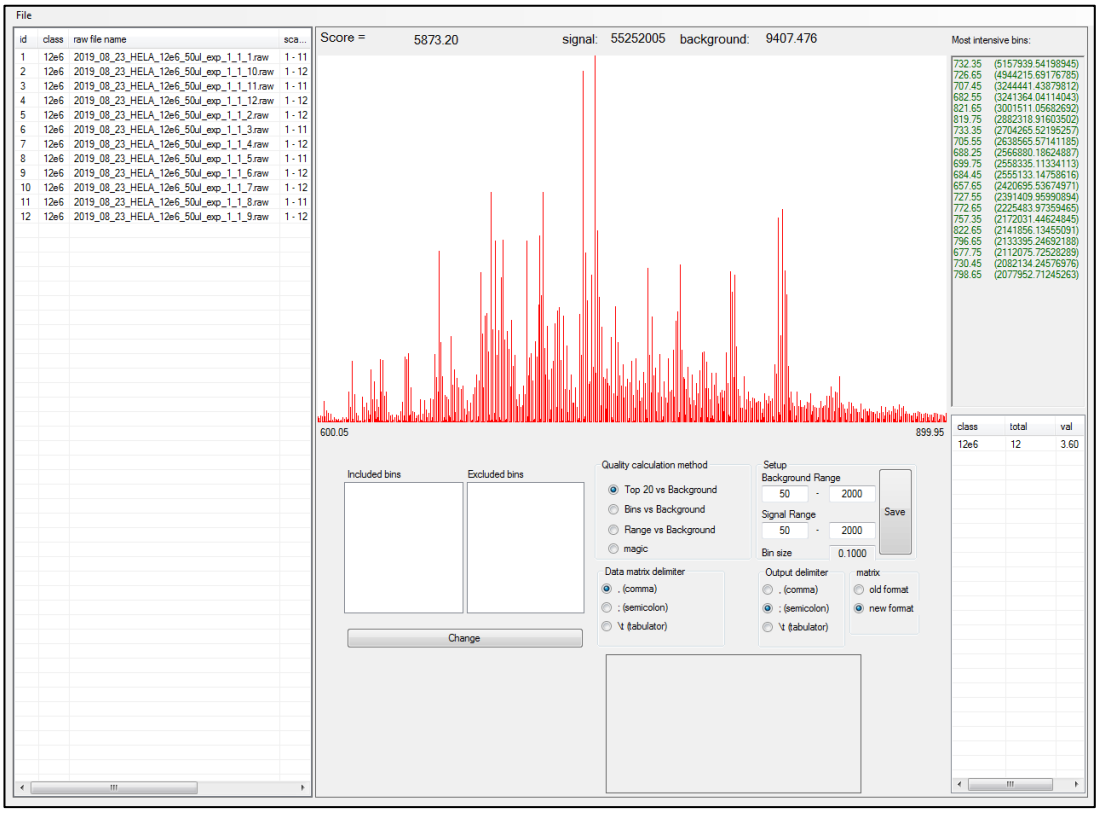

Figure 3.16: A screenshot showing the interface of the Spectral Quality Analyser software, highlighting the mass region selected and the output.

Table 3-4: A table showing the key fragments and their assignments following MS/MS analysis of *m/z* 794.56

Parent Ion *m/z*	Daughter Ion *m/z*	Fragment theoretical mass	Fragment Assignment	Putative Assignment
794.5617	168.06	168.0431	Phosphocholine with loss of CH3	PC(16:0/18:1)
	224.0723	224.0693	Glycerophosphocholine with loss of CH3 and H2O	
	255.2514	255.233	sn1 RCOO- ion	
	281.2633	281.2486	sn2 RCOO- ion	

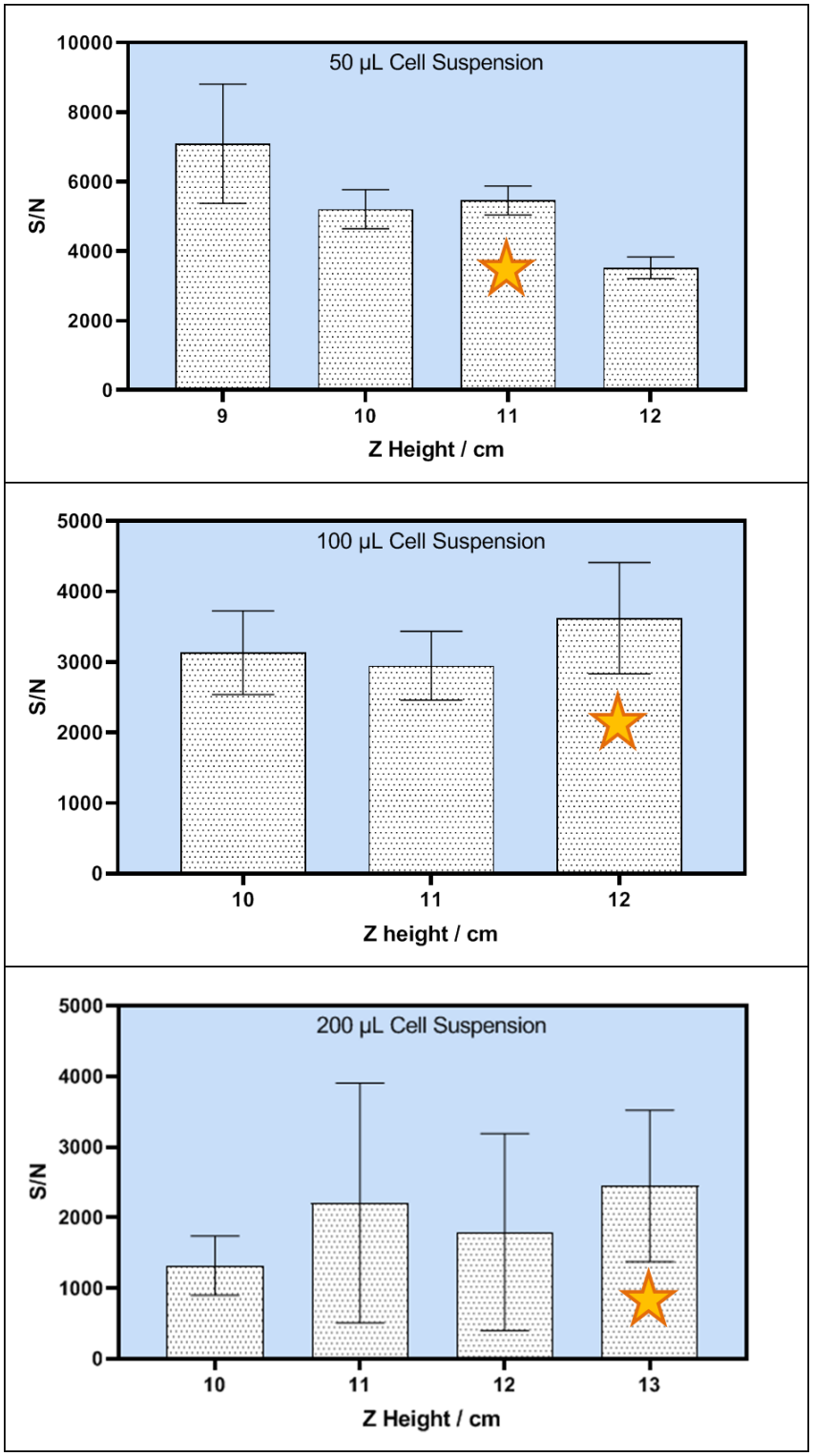

Figure 3.17: The average S/N for each volume of cell suspensions at the selected heights. The stars highlight the selected Z height value for each volume. This data was acquired on the Xevo G2-SX using a LASER REIMS ionisation source in negative mode.

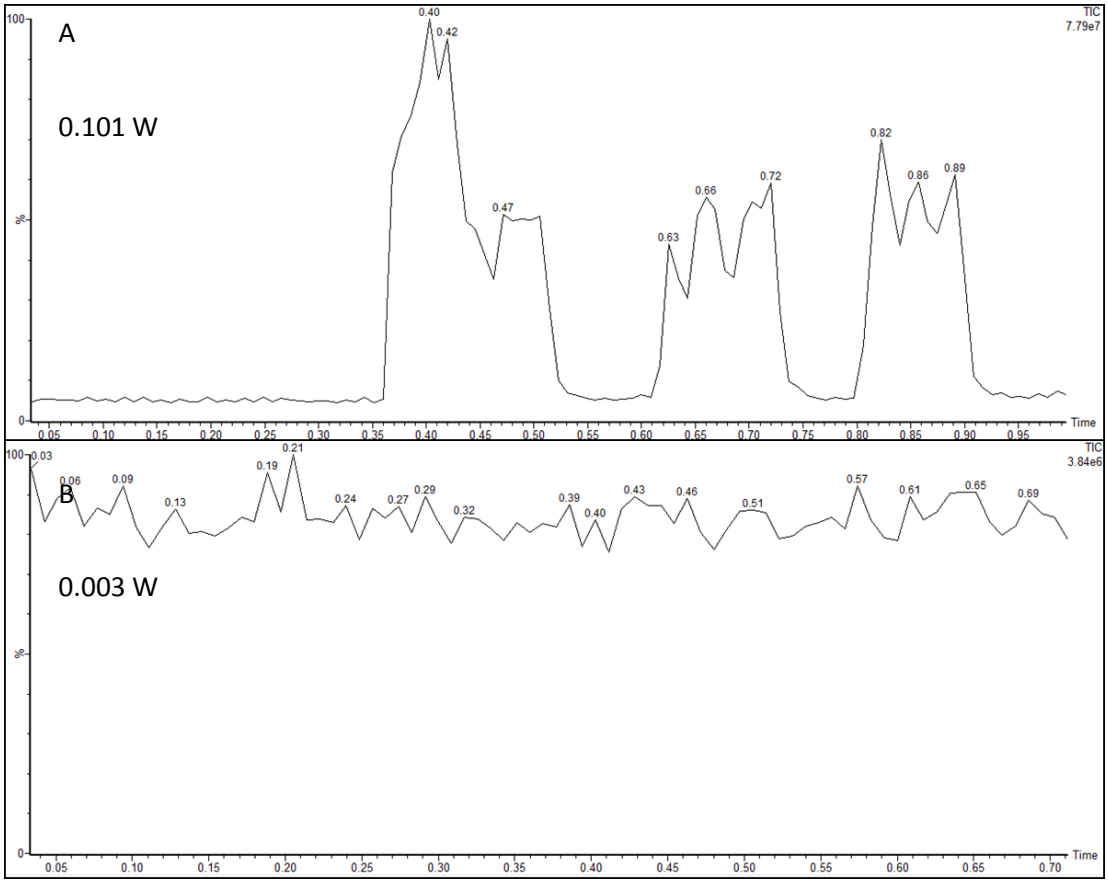

Figure 3.18: Chromatograms showing the burn events for the highest laser power (A) and the lowest laser power (B) This data was acquired with an 8 second laser dwell time for a cell suspension volume of 50 µL for 1e5 cells per well. The data was acquired on the Xevo G2-SX using a LASER REIMS ionisation source in negative mode.

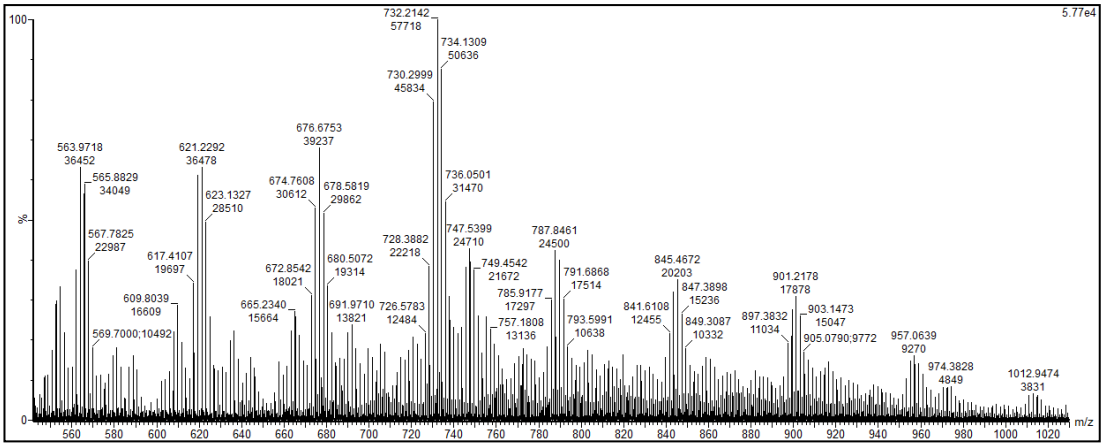

Figure 3.19: A spectrum showing the PEG repeating units caused from burning the plastic casing of the well plate during prolonged exposure to the laser. This data was acquired with an 8 second laser dwell time for a cell suspension volume of 50 µL for 1e5 cells per well. The data was acquired on the Xevo G2-SX using a LASER REIMS ionisation source in negative mode.

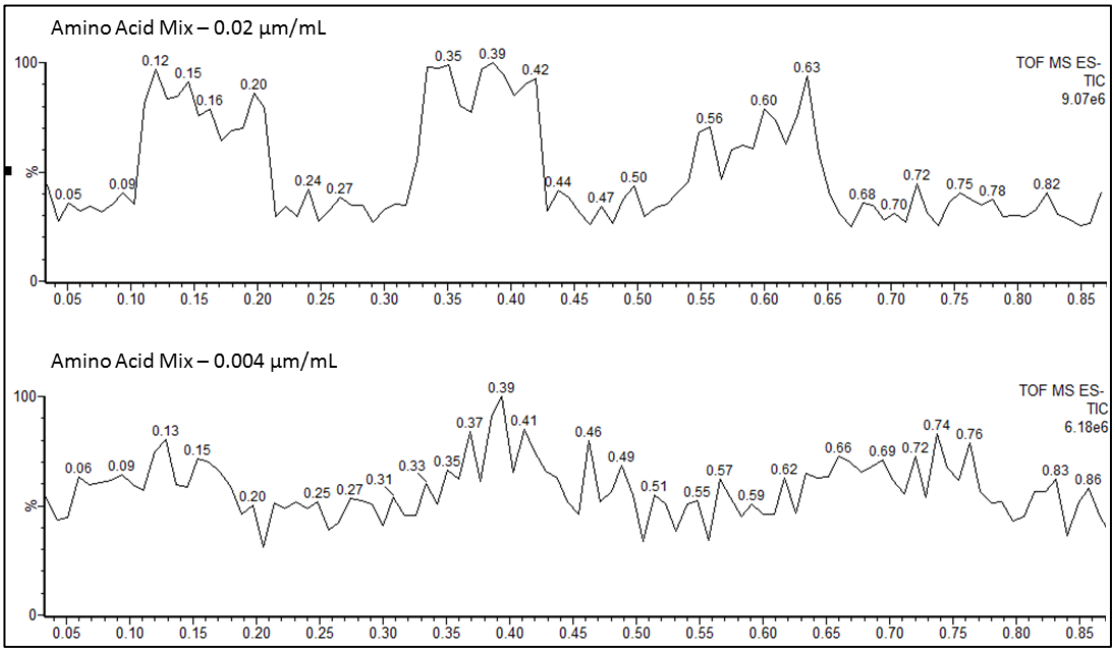

Figure 3.20: The chromatograms for the 0.02 and 0.004 µM amino acid dilutions. The data was acquired on the Xevo G2-SX using a LASER REIMS ionisation source in negative mode.

Chapter 4

Changes in Prostate Cancer Cells Post NSAID Exposure as Determined via ToF-SIMS and DESI-MS Lipidomic Experiments

4. Changes in Prostate Cancer Cells Post NSAID Exposure as Determined *via* ToF-SIMS and DESI-MS Lipidomics Experiments

Danielle J McDougall[1], Irma Berrueta Razo[1], Emrys Jones[2], Alex Henderson[1], Claire Hart[3], Michael Brown[3], Kaye Williams[5], Adam McMahon[4], Nicholas Lockyer[1]

1. Department of Chemistry, Photon Science Institute, Alan Turing Building, University of Manchester, Manchester, UK
2. Waters, Department of Research and Development, Wilmslow, UK
3. Manchester Cancer Research Centre, University of Manchester, Manchester, UK
4. Division of Informatics, Imaging and Data Sciences, Wolfson Molecular Imaging Centre, University of Manchester, Manchester, UK
5. Division of Pharmacy and Optometry, Faculty of Biology, Medicine and Health, Stopford Building, University of Manchester, Manchester, UK

4.1. Abstract

The current detection and treatment of prostate cancer (PCa) has a number of limitations, including lack of specificity for cancer types and therefore overtreatment issues. As a result, an alternative treatment approach of using ibuprofen was explored. This study examined a number of PCa cell lines, which differ in aggression, specifically observing the lipidomic fingerprint, post drug treatment. LNCaP, LNCaP-C4-2, LNCaP-C4-2B, and PNT2-C2 cell lines were analysed by a number of mass spectrometry imaging methods, including desorption electrospray ionisation (DESI) and time of flight secondary ion mass spectrometry (ToF-SIMS). These methods were analysed to exploit the benefits of these techniques individually and collaboratively. Following lipidomic experiments, multivariate statistical evaluation tools demonstrated a number of changing species. Following the COX-2 pathway, these changing lipids were scrutinised by examining the effect of inhibition on these pathways following drug addition.

4.2. Introduction

Prostate cancer is the second most common cancer in men worldwide, and the fifth overall cause of death in males.[1] It is predicted that in the UK 1 in 6 men will develop prostate cancer, however, it has been demonstrated that 86% of cases have a life expectancy of over 5 years.[2] Certain forms of the disease can be very slow growing, such a prostatic adenocarcinoma, which makes up about 90% of all cases.[3] As a result, in the majority of cases, the patient will die with cancer, not from cancer.[4] Prostate cancer diagnoses are categorised into three groups, localised, regional and distant. This grouping helps describe the level of migration of the cancer throughout the body.[5] Prostatic adenocarcinoma is considered local, and as mentioned, constitutes the majority of cases. However, if this cancer progresses far enough, this can spread to outside the prostate to nearby lymph nodes. Despite this, the estimated survival rate is almost 99% after 5 years.[5] Conversely, a very small number of cases are thought to be highly invasive and metastasis rapidly to the bone marrow stroma (BMS). These cases are considered distant and the type is predominantly prostatic small cell carcinoma. At this stage, the patient is given an estimated 6-12 months survival.[6]

Currently, diagnosis of this disease primarily involves a blood sample being screened for an increase in the prostate-specific antigen (PSA). However, this method has been demonstrated as unreliable and therefore is combined with other methods such as a digital rectal exam (DRE) or biopsies. After an abnormal PSA screening or DRE, a patient is typically sent for a biopsy. From this it is estimated that 75% of biopsies returned are benign.[7] There is no simple method for distinguishing between the indolent and aggressive form of this cancer, and as a result, the patient may be treated despite having the less aggressive strain. This treatment will involve the full removal of the prostate and all surrounding tissue, known as a radical prostatectomy.[3] However, the treatment itself can lead to a large

number of side effects that can drastically reduce the patient's quality of life. These include; urinary and rectal incontinency, growth of breast tissue, and erectile dysfunction.[8] Due to the high rate of the benign form of cancer, a large number of patients will have suffer more from this treatment, than with the cancer itself. As a result, it is imperative to discover new ways to diagnose and treat this cancer.

It has been demonstrated in literature that non-steroidal anti-inflammatory drugs (NSAIDs), such as ibuprofen, can potentially prevent further growth of PCa cells, offering an alternative treatment approach.[9,10] As a result, this paper aims to explore this alternative treatment method using cell based models, looking at a range of prostate cancer aggressions. The cells will be analysed using mass spectrometry imaging techniques to explore changes to the lipidome post treatment. Currently, there is a multitude of mass spectrometry imaging modalities available for lipidomics experiments on tissue samples, each with its own strengths.[11,12] Desorption electrospray ionisation (DESI) is an ambient method that allows the samples to be analysed with minimal sample preparation and without the constraints of a vacuum chamber. However, it has limitations including spatial resolution and detection of smaller metabolite species. Conversely, time-of-flight secondary ion mass spectrometry (ToF-SIMS), although is an ultrahigh vacuum method, has the ability to image to a much higher spatial resolution, allowing for lipidomic changes to be investigated at the single cell level, potentially showing subcellular information.[13] Due to their individual strengths, both of these modalities were explored to examine each methods advantage for cell monolayer samples and delve into how these methods can complement each other.

4.2.1. Mode of Action of Ibuprofen

Ibuprofen is a well-known and commonly used non-steroidal anti-inflammatory drug (NSAID). It is a non-selective inhibitor of the cyclooxygenase enzymes, COX-1 and COX-2.[14] Cyclooxygenases are enzymes whose primary role is the reduction of arachidonic acid (AA) into prostaglandin species (PGs). The arachidonic acid pathway has been shown to be essential in the progression of prostate cancer.[15] PGs are classified as eicosanoids and one of the most important of these is prostaglandin 2 (PGE2). PGE2 has an important biological role in the promotion of inflammation, angiogenesis, and growth. Prostatic cancer has the highest level of COX-2 expression in comparison to all other tissues. COX-2 is expressed in response to pro-inflammatory species such as PGE2 and as a result of this overexpression, the cell becomes resistant to apoptosis.[16] Therefore, it has been theorised that the addition of a COX-2 inhibitor may provide an additional therapeutic mechanism by slowing down prostate cancer cell growth and therefore slowing down the overall progression of the disease.[17]

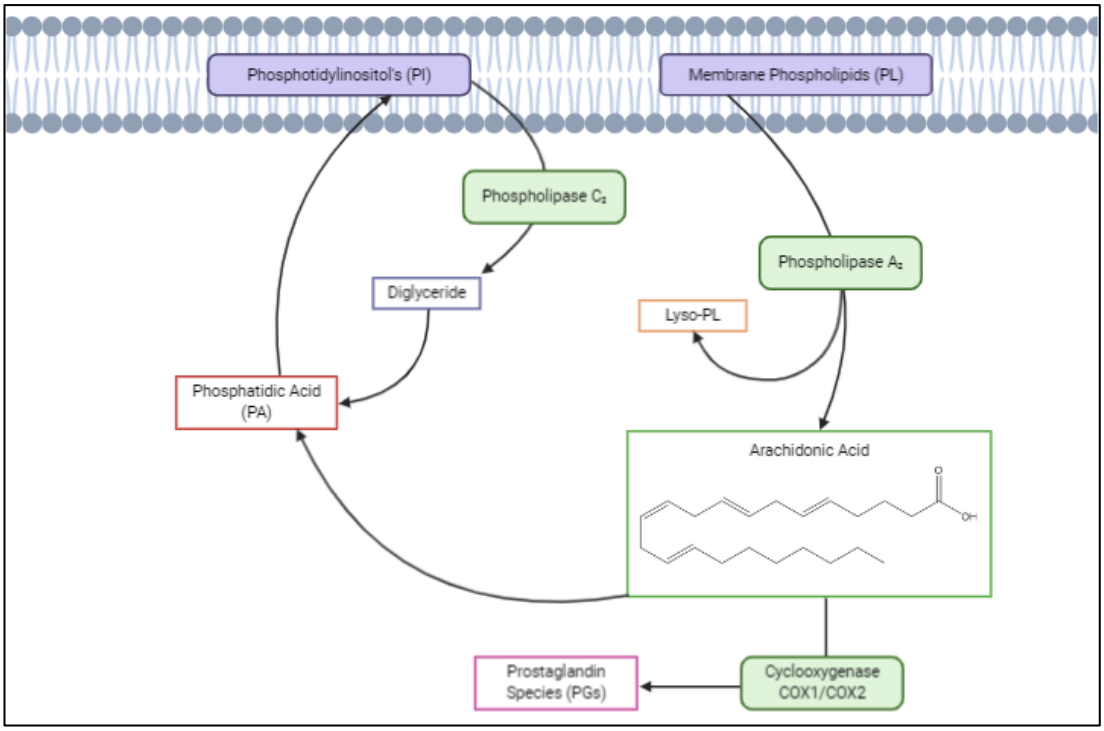

Figure 4.1: A simplified schematic of the COX-2 pathway, adapted18

Arachidonic acid is a fatty acid, made up of 20 carbon atoms and 4 carbon-carbon double bonds. Its lipid nomenclature is 20:4. Arachidonic acid is released from the cell phospholipid membranes and is then converted into PGE2 *via* the COX enzymes (Figure 4.1). This release mechanism can occur in two ways. The first involves the reduction of phosphatidic acid (PA) species into arachidonic acid. The second release mechanism occurs *via* the cleavage of membrane phospholipid species, creating lyso-lipid species and arachidonic acid. As the role of ibuprofen is to inhibit COX-2, it is theorised that, if the drug has an effect on the cells, this should result in an increase in AA, which may be observed using MSI methods. However, it has been demonstrated that in order to regulate the overall concentration of free fatty acids in a system, AA can be involved in a re-acylation cycle back into membrane lipids, which is known as the Lands Cycle.[19] Therefore, this interaction will be the primary target of the lipidomic study.

In human samples, the main produced metabolites of ibuprofen are 2-hydroxyl-ibuprofen (2-OH-IBP) and a carboxylic acid form (CBX-IBP)[20] (Figure 4.2). In order to fully explore the interaction of ibuprofen in cell material, ibuprofen and its metabolites were targeted during the imaging experiments. This will allow for spatial information about the target region of the drug.

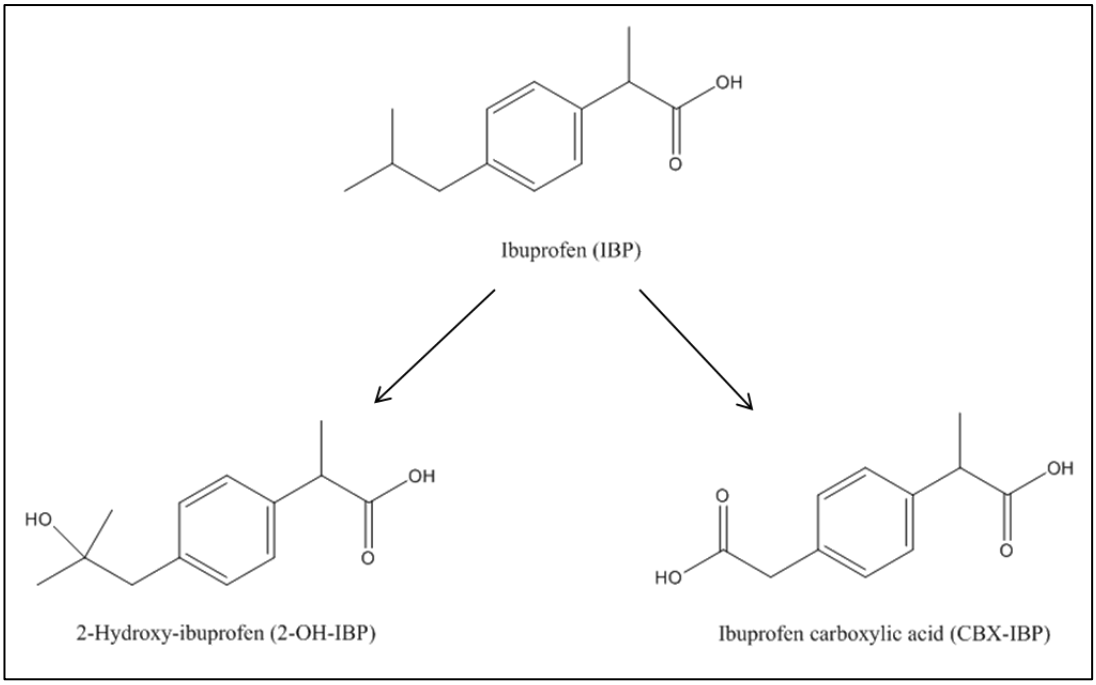

Figure 4.2: Labelled structures of ibuprofen and the major metabolites

4.2.2. Cell Lines

For this experiment, it was crucial to have cells with the same phenotype to ensure that any differences that are observed due to drug interaction are as a result of the differing aggressions. For this reason, the cell lines described above, LNCaP, LNCaP-C4-2 and LNCaP-C4-2B, were selected. To serve as a normal control for healthy tissue, the PNT2-C2 cell line was utilised.

4.2.2.1.LNCaP

The LNCaP cell line was derived from a needle biopsy from a patient suffering with lymph node adenocarcinoma of the prostate.[21] LNCaP demonstrates a good baseline model for looking at the metastatic potential within prostatic cell lines due to its reduced metastatic capacity. This cell line also offers the possibility observe the involvement of hormones and androgen response on the growth rate and other homeostatic factors.[22] Overall, LNCaP has

proven to be an effective model for lymph node metastatic prostate cancer despite its low metastatic potential.[23]

4.2.2.2.LNCaP Derivatives

There are several, well established, derivatives of the LNCaP Cell line. Experimentation continued on this cell line in the 1980s and this cell line was used to seed a xenograft into a nude mouse.[24] This created an LNCaP tumour on the flank of the mouse. This created a slightly more invasive model of the cell line named LNCaP-C4-2 (C42). Following this, the mouse underwent metastatic mutations due to the cancer, spreading to the bone marrow stroma (BMS). This was then isolated as a much more aggressive and invasive model, LNCaP-C4-2B (C42B). [21,22]

4.2.2.3.PNT2-C2

In order to fully explore the differences between cancerous cell lines, it is essential to have a biological control. PNT2-C2 was selected as the biological control as it is a normal human epithelial cell line and primarily non-tumorigenic. Using the SV40 protein, this cell line was derived and immortalised in the early 1990s and holds many characteristics that are unique to healthy tissue.[25]

Table 4-1: Information about the androgen sensitivity and common metastasis for each cell line

Cell line	Model	Androgen sensitivity	Metastasis
LNCaP	Human	Androgen dependent	Lymph node
LNCaP-C4-2	Mouse	Androgen independent	Bone marrow stroma
LNCaP-C4-2B	Mouse	Androgen independent	Bone marrow stroma
PNT2-C2	Human	Androgen independent	-

4.3. Materials and methods

4.3.1. Chemicals

All solvents and culture media, unless specified, were obtained from Sigma-Aldrich (Poole, UK). The solvents were of HPLC grade or purer.

4.3.1.1.Cell Culture

The cell lines selected for this project are all cultured in the same media, which allows for standardisation throughout the cell lines. The media used is RPMI media substituted with FCS (HyClone, 10%), L-glutamine (1%), HEPES buffer (1%), and sodium pyruvate (1%). Due to the strong androgen hormone involvement within this cell line, it is essential that the FCS selected be from a batch containing approximately >50% male calves. Therefore, prior to culture, the FCS was batch tested in order to ensure the cells didn't undergo any additional stress during growth.

4.3.2. Drug Treatment

4.3.2.1.Drug treatment sample preparation – DESI and SIMS

For the SIMS and DESI sample preparation, the appropriate substrate, either silicon wafers or glass coverslips respectively, were sonicated for 15 minutes with hexane (5 mL) followed by methanol (5 mL), and added to each well of a 6 well plate. Following this, the corresponding cells were seeded at a final density of 900,000 cells per well with a final media volume of 3 mL. These were incubated at 37 ˚C and 5% CO_2 for 48 hours to allow the cells to settle before drug addition. The media was then aspirated and 3 mL of fresh media containing ibuprofen was added to the corresponding wells for each concentration. The cells were placed into incubator once more for each designated time point. Following drug treatment, the media was once again aspirated and each well was rinsed twice with PBS (1x, 50 µl) followed by ammonium formate (150 mM, 50 µL). The well plates were then flash frozen and stored at -80 ˚C until analysis.

4.3.2.2.Ibuprofen

An initial stock solution was made up of 500 mM ibuprofen (Sigma Aldrich) using DMSO. Aliquots were then diluted into methanol to give a final DMSO concentration of 10% in secondary stocks of 50 mM and 100 mM. From these stocks, the desired concentrations were made up using media, allowing for a final DMSO concentration below 5%. The final concentrations were as shown (Table 4-2).

Table 4-2: The makeup of each of the concentrations for ibuprofen and the final concentration of DMSO for each.

Concentration	Total Volume (mL)	Volume of DMSO stock (mL)	Volume of 100 mM EtOH stock (µL)	Volume of 50 mM EtOH stock (µL)	Volume of Media (EtOH*)Added (mL)	Final DMSO concentration
500 mM	10	10	-	-	-	100%
100 mM	5	1	-	-	4*	20%
50 mM	10	1	-	-	9*	10%
10 mM	10	-	1000	-	9	2%
8 mM	10	-	800	-	9.2	1.60%
5 mM	10	-	-	1000	9	1%
2 mM	10	-	-	400	9.6	0.40%
1 mM	10	-	-	200	9.8	0.20%
0.1 mM	10	-	-	20	9.88	0.02%

4.3.3. MTT Assay

The MTT assay is a colorimetric assay that uses the cells' metabolic activity to determine the viability post drug treatment. If a cell is metabolically active, the yellow tetrazolium salt (3-(4,5-dimethylthiazol-2-yl)-2,5-diphenyltetrazolium bromide) is reduced to form a purple formazan crystal (Supplementary; Figure 4.11). Once the cells have been incubated with MTT for an appropriate amount of time, quantification of the cell growth and viability can be measured by recording the absorbance at 570 nm. Prior to the assay, the cells were seeded and drug treated as above. Once the corresponding time point has been reached, the plate is collected and prepared for the MTT assay. A solution of MTT (2.5 mg/ml in PBS, 50 µL) is added to each well, and the plates were incubated in the dark for 4 hours at 37 ˚C. Following this, all media was aspirated and 200 µL of DMSO was added to each well. The plates were then placed on a shaking table to allow for the formazan to fully dissolve. The absorbance was then recorded at 570 nm on a microplate reader.

4.3.4. MS analysis

4.3.4.1.Desorption Electrospray Ionisation (DESI) Mass Spectrometry

DESI-MS analysis of the glass cover slips were acquired on the Waters Xevo G2-XS QToF instrument with an attached DESI source. The DESI sprayer used was a prototype with an added heated capillary and fixed geometry. This was optimised to allow for highest signal of lipid species and highest spatial resolution. The fixed geometry of the sprayer allowed for higher consistancy between various aquisitions.[26] The solvent of choice was 98:2 methanol:H_2O and the selected mass range is typical for a lipidomics experiment, at 50-1200 Da. This allowed for a full coverage of the species of interest. The instrument was operated with a solvent flow rate of 1.5 µL/min using the heated capilary at 12,000 V and 500 ^{o}C. The spatial resolution used ranged from 250 µm down to 20 µm, depending on the sample of interest. The instrument ran at a typical rate of 4 scans per second. Tandem MS experiements were run using a collision energy between 15 - 65 V. The data was aquired in both polarities.

4.3.4.2.Time of Flight Secondary Ion Mass Spectrometry

The instrument used for SIMS analysis was the J105 3D chemical imager (Ionoptika Ltd, Chandler's Ford, UK). The ion beam employed used the 40 keV C_{60}^{+} source. Using a field of view of 280 x 280 µm, and a raster of 128 x 128 pixels, with a beam focus of approximately 2µm. The mass range acquired was 95 - 1072 Da. The ion dose was 2.1 x 10^{13} ions/cm^2 which allowed for depth profiling of the sample. The samples were analysed in both positive and negative ion mode.

4.3.5. Data Analysis

For all experiments, each cell line sample was repeated in triplicate during the growth phase, then in further triplicate at different passages. For DESI and ToF-SIMS analysis, each sample was analysed and three individual regions were selected and extracted, allowing for technical repeats and the calculation of error bars using standard deviation. Multivariate analysis used was principal component analysis (PCA). For DESI experiments, regions of interest were selected and normalised to total ion count using the HD imaging software (HDI v1.4, Waters Corporation, Wilmslow). For each ROIs the top 1000 most abundant peaks were then extracted into a .csv format and uploaded into Metaboanalyst, v4.0[27] for principal component and additional multivariate analysis. For PCA, the 600-900 mass range was selected to allow for analysis of the changing lipid region. All MS/MS spectra were acquired using data directed analysis (DDA) with DESI in negative mode. An MS survey scan was run with DESI by rastering across the sample acquiring the full mass range (50-1200) for 0.5 s. The top 15 peaks detected were fragmented for 0.25 s per mass window with a collision energy ramp from 15 -65 V. These 15 peaks will then be entered into an exclusion list and the process repeated, detecting the next 15 top peaks and so on.

In order to analyse the ToF-SIMS data, images were examined using Ionoptika Image Analyser software (v2, Ionoptika, Southampton). For PCA of the SIMS data, the files were read into an in-house Matlab (Mathworks) code which allowed for ROIs to be drawn. The selected pixels were sum normalised before undergoing multivariate analysis. All graphs were created using the GraphPad Prism 8.3 software (GraphPad Software, La Jolla California USA).

4.4. Results and Discussion

4.4.1. MTT Assay

In order to fully explore the effects of ibuprofen on a range of cell lines, an MTT assay was run at a series of drug concentrations. This indicated the concentration at which the drug stopped all metabolic activities within the cell.

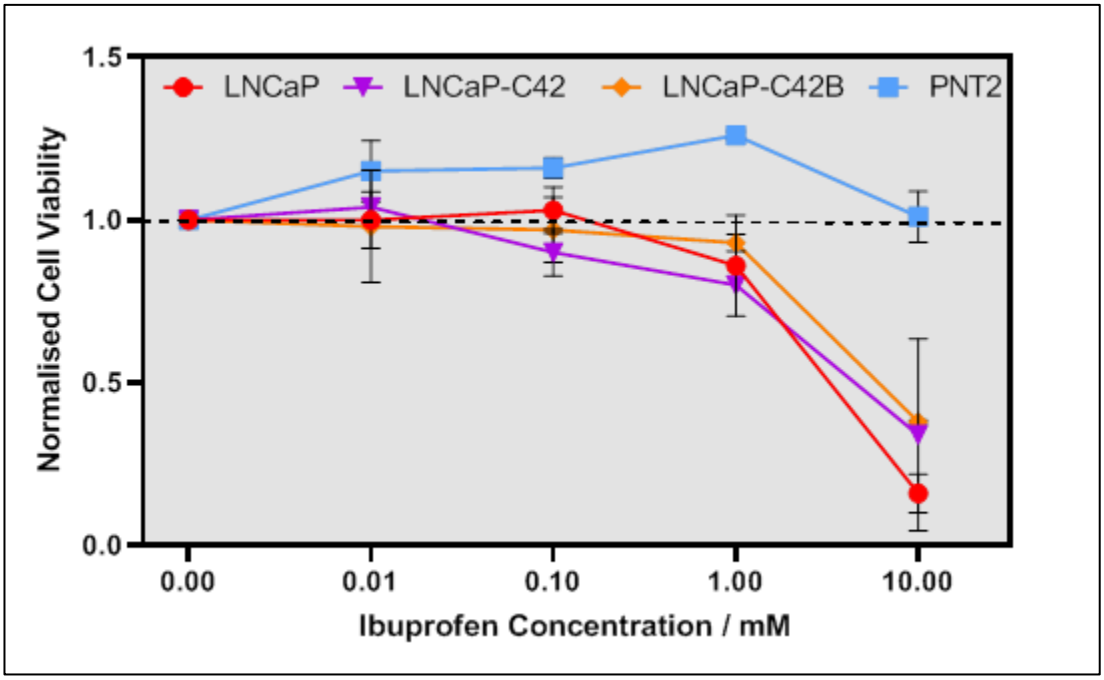

Figure 4.3: The normalised cell viability for each labelled cell line for a range of ibuprofen concentrations. The data was acquired post MTT assay using a UV colorimeter at the wavelength 570 nm.

As shown (Figure 4.3) at a concentration above 1 mM there is a clear decline of metabolic activity for all cell lines, except the PNT2-C2. This demonstrates that the drug is interacting with the cancerous cell lines, whereas the healthy control cell line remains unaffected. For PNT2-C2, at 10 mM the viability of the cell line remains unchanged from the control. This data also highlighted a range of concentrations, between 0.1 mM – 1 mM, where the drug is interacting with the cell lines, but not yet halting metabolic activity. Therefore, within this

concentration range, the interactions of the lipids for the cancerous cell lines can be explored further.

4.4.2. Desorption electrospray ionisation

Using DESI to analyse the cell lines post drug treatment, the lipid region was targeted to explore the drug interactions. As previously mentioned, arachidonic acid metabolism is inhibited by the NSAID. In order to explore this, the signal from AA was normalised to the sum of the lipid signal (*m/z* 600 – 900) for the cell lines at the selected drug concentrations.

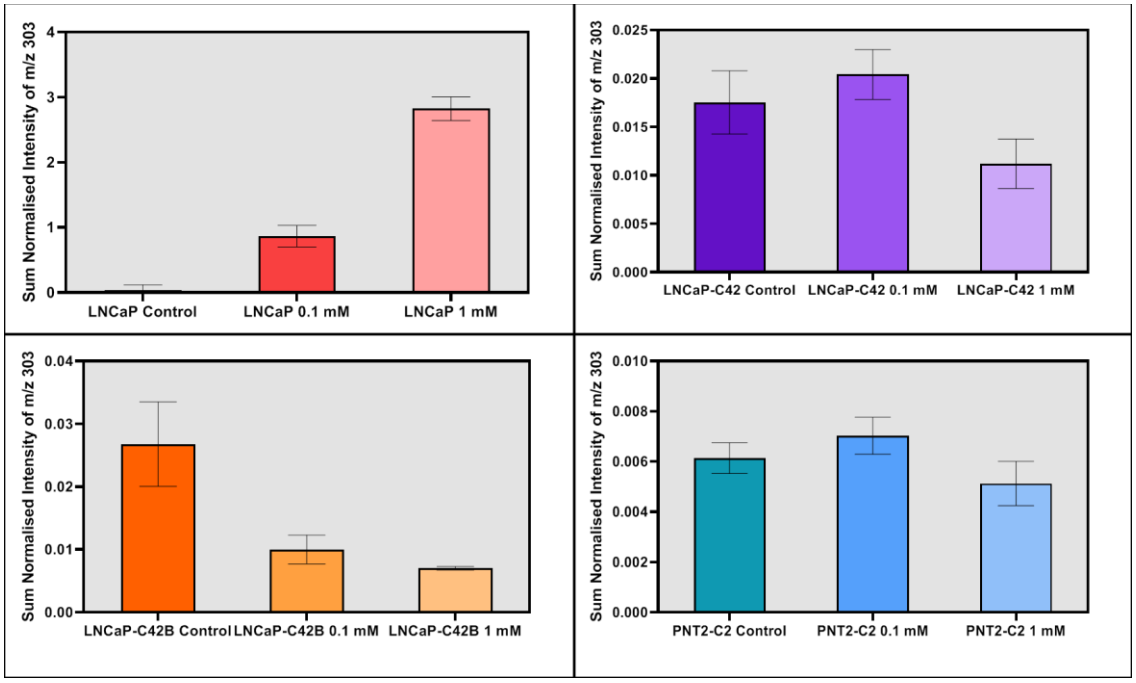

Figure 4.4: Ratio of arachidonic acid intensity to the summed lipid species signal for the selected drug concentrations for each labelled cell line. This data was acquired using the Xevo-G2-XS instrument with DESI ionisation source, in negative mode.

For the LNCaP cell line, the ratio of the AA species to summed total of the lipid species (Figure 4.4) shows an overall rise as you increase the NSAID concentration. With increasing dose of ibuprofen, one would expect an accumulation of AA as it can no longer undergo the conversion to the PGs. For the LNCaP-C42 and C42B, observed is a shift in maxima towards the lower concentrations with increasing cell aggression. This result will be explored in

more detail later in this chapter. Conversely, the PNT2-C2 species exhibit no overall trend due to the overlapping error bars. As demonstrated by the MTT assay (Figure 4.11), the ibuprofen does not alter the metabolic activity of this cell line. This data supports the suggestion that the ibuprofen does not interact with the control cell line, PNT2-C2, therefore not inhibiting the COX-2 pathway.

4.4.3. Desorption Electrospray Ionisation Principal Component Analysis

In order to explore any further differences observed for the lipid species, multivariate analysis PCA was run for each of the cell lines for the selected concentrations.

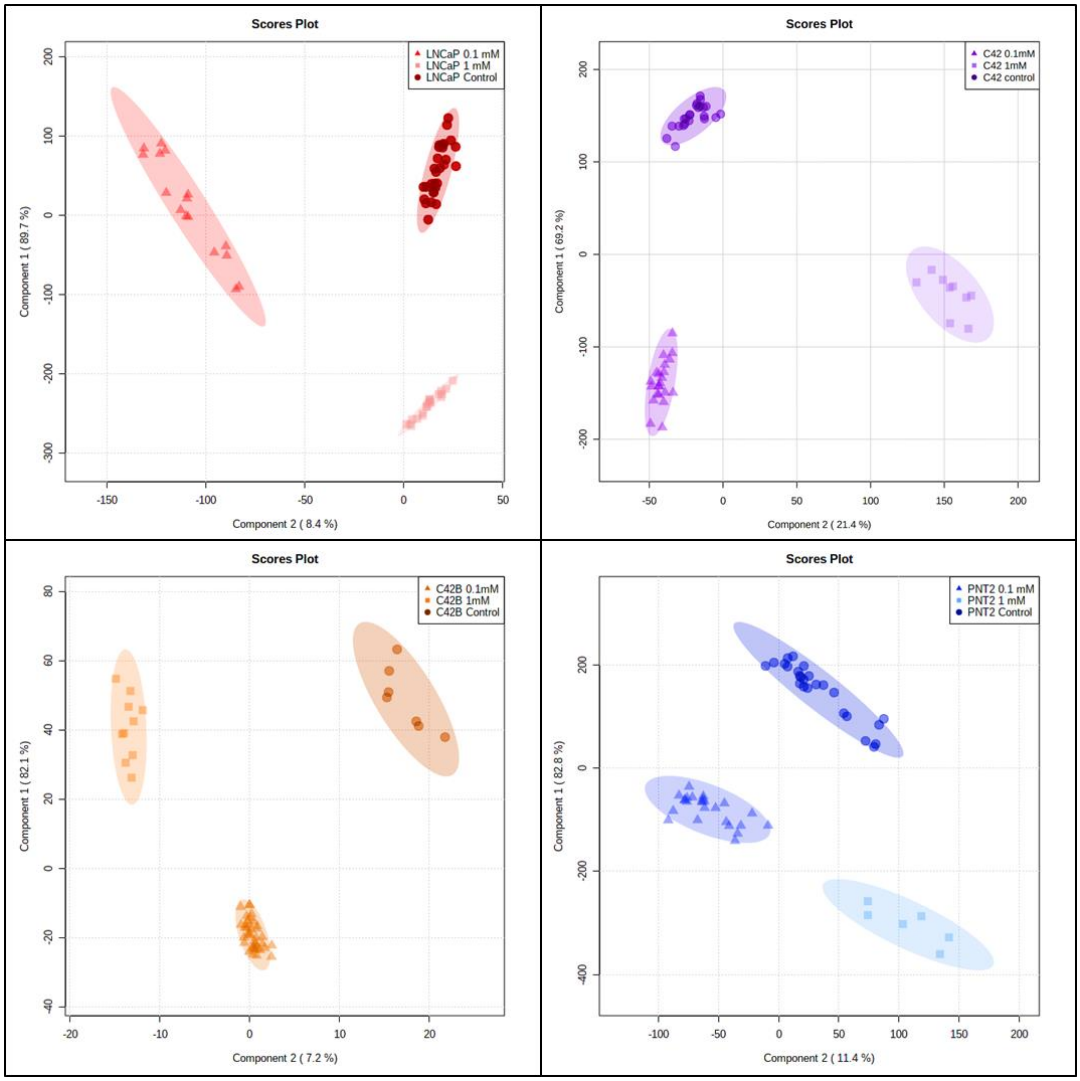

Figure 4.5: PCA plots for each of the selected cell lines at a range of drug concentrations. The PCA was acquired on the 600-900 mass range for negative mode data. The above plots were created using metaboanalyst. This data was acquired using the Xevo-G2-XS instrument with DESI ionisation source, in negative mode.

As shown by the PCA, observed is a clear separation of each of the drug treatments (Figure 4.5). The loadings were extracted to further examine the *m/z* values creating the separation observed. For each cell line, the top 8 highest loaded species were surveyed and a list of potential species created (Table 4-3). Tandem MS experiments were run on these *m/z* values to gain an additional degree of confidence. Where lipid species have been quantified, the fragmentation information has been supplied (Supplementary; Figure 4.12,

Table 4-5). Where MS/MS was unable to fully characterise the lipid, accurate mass was used to determine the most likely species. Future work will focus on confirming these species, for example through the analysis of authentic standards or LC-MS/MS of extracts.

Table 4-3: The extracted loadings for the LNCaP cell line post drug treatment. This data was acquired using the Xevo-G2-XS instrument with DESI ionisation source in negative mode. The red values are those without full MS/MS confirmation

LNCaP Control					
m/z	Putative Assignment	PC1	PC2	PPM Error	Theoretical *m/z*
766.5375	PE (20:4/18:0)	0.12191	-0.086305	2.2	766.5392
750.5410	PE(P-18:0/20:4)	0.12112	-0.17959	4.4	750.5443
748.5224	PE(P-18:1/20:4)	0.11676	-0.079577	8.4	748.5287
774.5364	PE (P-18:0/20:6)	0.067957	-0.04781	10.2	774.5443
728.5585	PE(P-18:0/18:1)	0.064072	-0.072747	2.1	728.5600
773.5336	PG(18:1/18:1)	0.061638	-0.21756	0.3	773.5338
752.5566	PE(P-18:0/20:3)	0.053741	-0.22498	4.5	752.5600
717.5280	DG(44:9)	0.042434	-0.18543	25.5	717.5463
LNCaP 0.1 mM					
m/z	Putative Assignment	PC1	PC2	PPM Error	Theoretical *m/z*
744.5550	PE(18:1/18:0)	0.65345	-0.36319	0.1	744.5549
716.5244	PE(16:0/18:1)	0.46161	-0.32108	1.1	716.5236
742.5389	PE(18:1/18:1)	0.44427	-0.27331	0.4	742.5392
717.5280	DG(44:9)	0.19011	-0.14347	25.5	717.5463
743.5438	PG(34:3)	0.18911	-0.13033	76.5	743.4869
766.5375	PE (20:4/18:0)	0.17233	-0.2522	2.2	766.5392
748.5224	PE(P-18:1/20:4)	0.13994	-0.2762	21.8	748.5387
768.5518	PE(18:0/20:3)	0.13674	-0.088743	4.0	768.5549
LNCaP 1 mM					
m/z	Putative Assignment	PC1	PC2	PPM Error	Theoretical *m/z*
641.4240	PA(22:3/10:0)	-0.0024549	-0.0017169	8	641.4188
653.4771	PA(P-16:0/18:3)	-0.0040953	-0.0034547	33	653.4552
618.3633	PE(P-28:0)	-0.0044208	-0.0010795	140	618.4504
681.5023	PA(36:4)	-0.0051583	-0.0021366	23	681.4865
601.3494	PA(P-20:1)	-0.0054848	0.001037	123	601.4239
705.4877	PA(P-38:5)	-0.0062077	-0.002476	1.7	705.4865
675.4903	PA (16:0/18:0)	-0.0070557	-0.010054	9	675.4970
661.3641	PG(28:2)	-0.0088301	-0.0028087	67	661.4086

As observed by the loadings (Table 4-3), at high concentrations the PCA separation is driven by a change in the PA species. Using the raw data, the highest loaded species defined were examined to explore this result further.

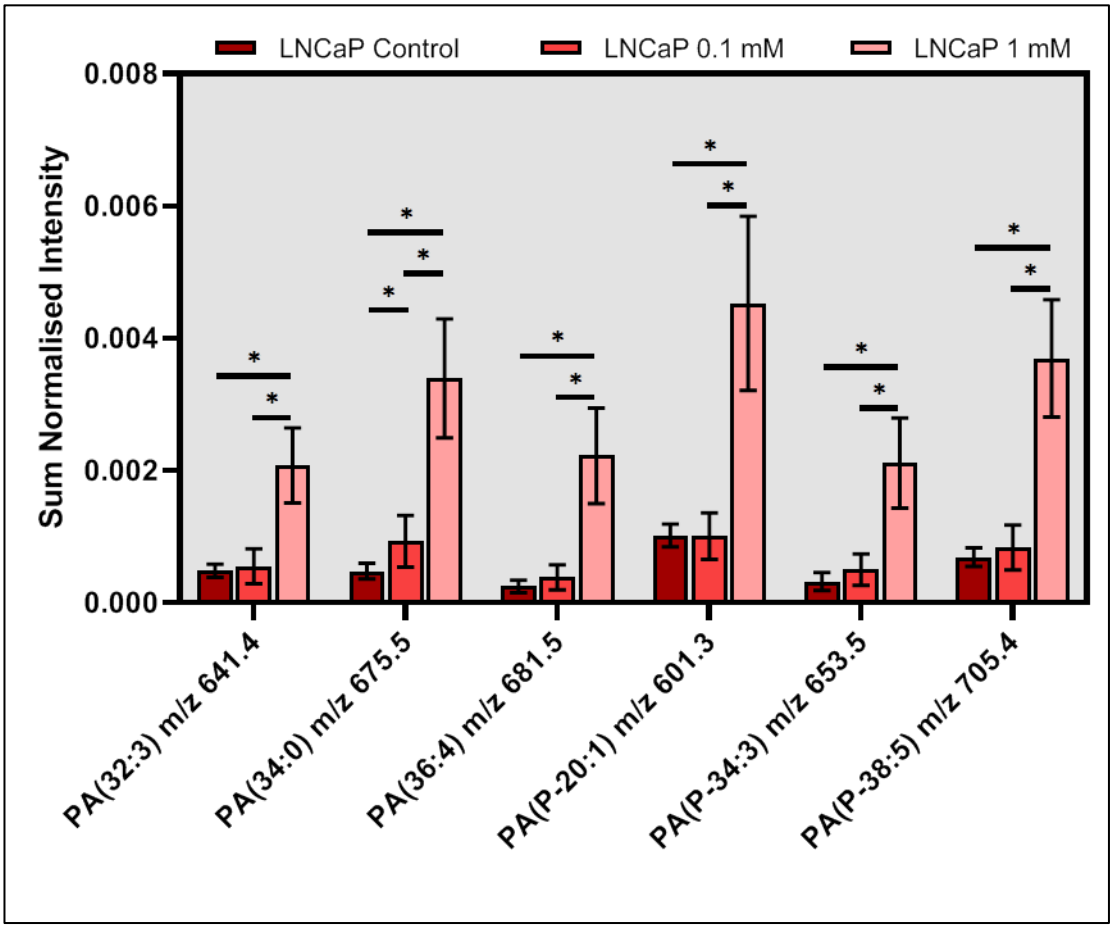

Figure 4.6: The intensity of the highest loaded PA species for each of the selected drug concentration for the LNCaP cell line normalised to the sum of the total lipid signal. The asterisks indicates significance <0.001 calculated using Ordinary one way ANOVA with Graphpad Prism software This data was acquired using the Xevo-G2-XS instrument with DESI ionisation source, in negative mode.

As observed, at higher concentrations of drug, an overall significant increase in the presence of PA is observed (Figure 4.6). This result can provide evidence to demonstrate that the conversion of PA to AA is a reversible mechanism, as suggested by the Lands cycle. Therefore, at higher ibuprofen doses the abundance of AA can trigger the exchange back into PA. Hence, the overall increase of these species observed at 1 mM ibuprofen.

For the more aggressive cell line, LNCaP-C42, the PA species decreased with drug concentration (Supplementary; Table 4-6, Table 4-7). However, a rise in phosphatidylinositol lipid abundance is observed.

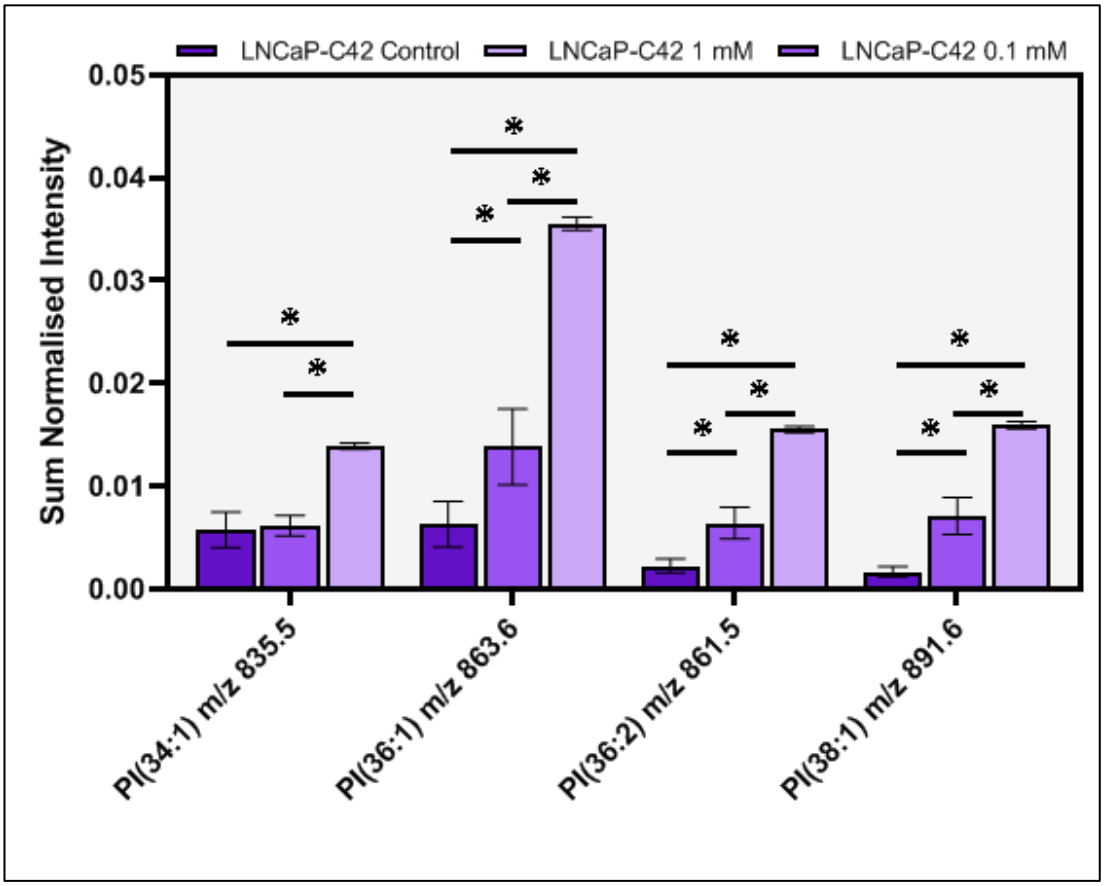

Figure 4.7: The intensity of the highest loaded PI species for each of the selected drug concentration for the LNCaP-C42 cell line normalised to the sum of the total lipid signal. The asterisks indicates significance <0.001 calculated using Ordinary one way ANOVA with Graphpad Prism software This data was acquired using the Xevo-G2-XS instrument with DESI ionisation source, in negative mode.

It is observed, Figure 4.7, that there is a significant increase in the PI species for both drug concentrations. This rise could be due to the process of conversion of AA to PA progressing past this point and converting the PA species back into the PI lipids. Following the trend observed for the relative values of AA for the LNCaP-C42, reaching a maximum and then decreasing (Figure 4.4), this result further suggests that increasing arachidonic acid causes change in the equilibrium favouring the conversion back into PI species. Future work will aim to explore this result further. For the most aggressive cell line LNCaP-C42B no

discernible pattern of changing lipid species with concentration is observed. This suggests that the cell response to ibuprofen is different for the highly aggressive cell line, LNCaP-C42B. Future work warrants further investigation into the changes observed with PCA.

4.4.4. Secondary Ion Mass Spectrometry

ToF-SIMS offers an advantage in terms of single-cell spatial resolution over DESI and therefore was compared to the data acquired using DESI to explore these strengths for lipidomics research. Using the LNCaP and PNT2-C2 cell lines as a basis for comparison, the drug challenge study was repeated for the SIMS technique.

4.4.4.1.Secondary Ion Mass Spectrometry Principal Component Analysis

To allow for comparison of this mass spectrometry technique to the DESI analysis, the samples were analysed post drug treatment with PCA, in the same way.

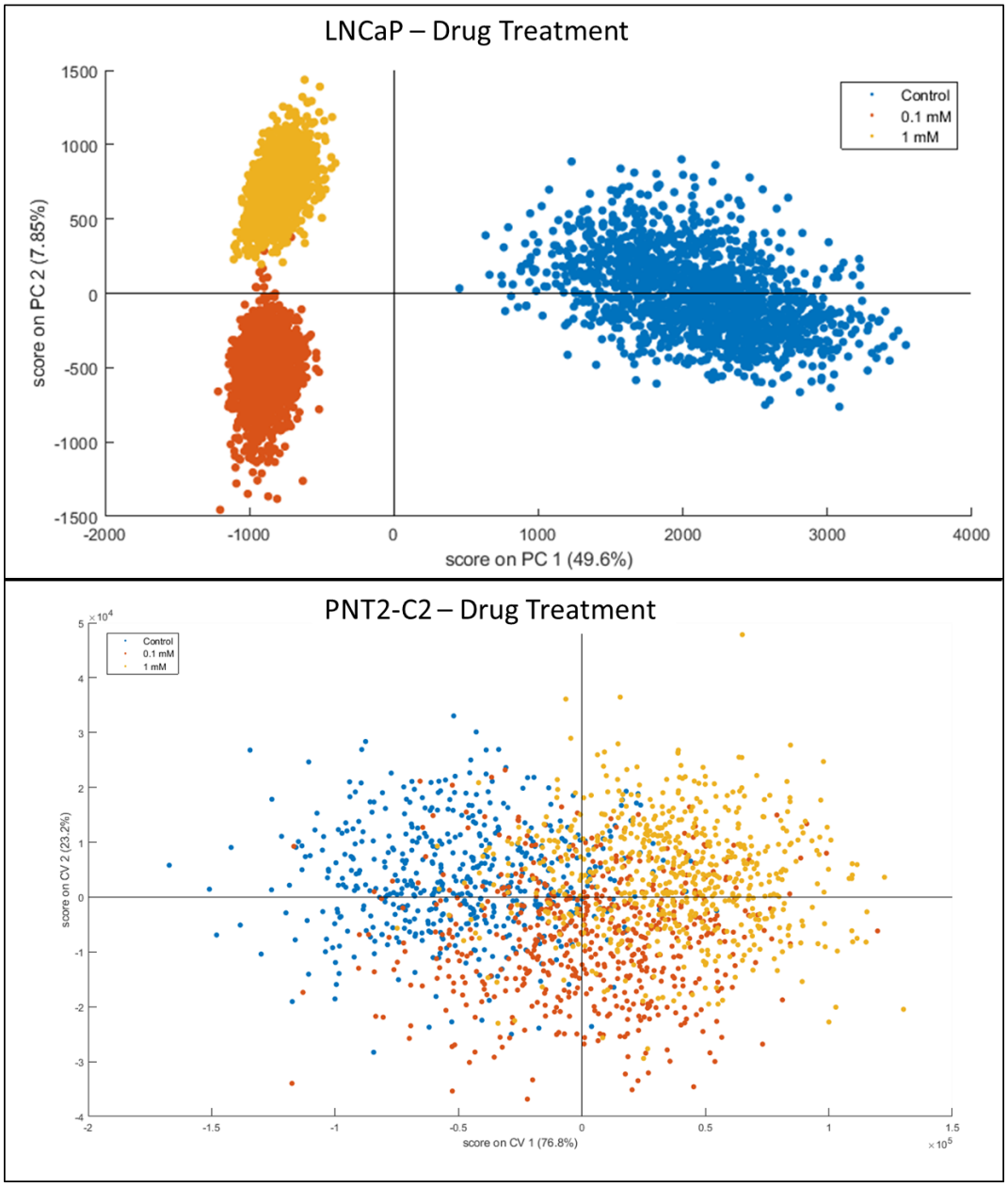

Figure 4.8: A PCA plot for the LNCaP and the PNT2-C2 cell line post drug treatment. PCA was run using the full mass range in negative mode. The initial data was acquired with the ToF-SIMS utilising the C_{60}^{+} ion beam in negative mode.

The above PCA plot (Figure 4.8), demonstrates that for the LNCaP cell line there is a clear separation between the drug treatments, whereas this is not observed with the PNT2-C2 cell line. These results are consistent with what has been demonstrated with the previous DESI data. However, the ionisation processes in DESI and SIMS are very different, and it would be reasonable to expect that they reveal different aspects of changes to the lipid

profile. To further investigate this, the loadings (Supplementary; Figure 4.13) were extracted for the LNCaP cell line.

Table 4-4: The extracted loadings and suggested species and chemical formula for each species

m/z	PC1	Suggested Species	Formula	Adduct	Theoretical Mass
96.88	0.273	H2PO4-	$H_2PO_4^-$	$[M-H]^-$	96.9696
100.05	0.209	Sphingolipid species	C5H12NO	$[M-H]^-$	-
103.06	0.08459	DPPC	C5H13NO-	$[M-H]^-$	-
112.12	0.06282	-	-	$[M-H]^-$	-
117.12	0.07444	-	-	$[M-H]^-$	-
119.14	0.07667	-	-	$[M-H]^-$	-
121.02	0.1141	-	-	$[M-H]^-$	-
122.10	0.07576	-	-	$[M-H]^-$	-
128.05	0.151	-	-	$[M-H]^-$	-
134.15	0.134	Homocysteine	C4H10NO2S	$[M-H]^-$	136.0426
137.09	0.2959	-	-	$[M-H]^-$	-
139.02	0.09677	-	-	$[M-H]^-$	-
140.01	-0.0007176	Ethanolamine Phosphate Ion		$[M-H]^-$	-
144.04	0.08309	-	-	$[M-H]^-$	-
152.90	-0.06068	Glycerol-3-phosphate ion with loss of H2O	C3H6PO5	$[M-H]^-$	152.9958
155.05	0.1261	-	-	$[M-H]^-$	-
159.03	-0.09837	Cholesterol	C12H17	$[M-H]^-$	161.0444
181.01	0.1397	-	-	$[M-H]^-$	-
183.06	0.01149	DPPC	$[C5H14NPO4]^-$	$[M-H]^-$	183.0617
199.01	-0.04771	-	-	$[M-H]^-$	-
241.11	-0.02029	Inositol Phosphate ion - H20	C6H10PO8−	$[M-H2O]^-$	241.01
255.33	-0.03236	FA (16:0)	C16H31O2−	$[M-H]^-$	255.233
281.35	-0.03974	FA (18:1)	C18H33O2−	$[M-H]^-$	281.2486
283.26	-0.02219	FA (18:1)	C18H31O2−	$[M-H]^-$	283.2643

Due to the high energy nature of the C60 ion beam, the majority of species observed are lipid fragments. However, despite this, the signal acquired allows for information about the lipid headgroups responsible for the differences observed in the PCA plot. As shown, (Table

4-4) there are a number of fatty acid species observed causing changes between the control and drug treated state. This is an interesting result when combined with the information that there are more lyso-species observed with DESI, post drug admission. This could potentially support the theory that the lyso-species are upregulated post ibuprofen dose as an effect of the COX-2 inhibition. This again, highlights the usefulness of these imaging techniques when used in combination. Further work will include MS/MS experiments to help identify the remaining species

4.4.4.2.Secondary Ion Mass Spectrometry Imaging

Due to the high spatial resolution (~1 μm spot size) exhibited by the C60 ion beam, intracellular information can potentially be obtained. Using ToF-SIMS, the samples were depth profiled as described earlier. The two main species targeted and observed were *m/z* 180 which is a phosphatidylethanolamine (PE) fragment[28] and *m/z* 125 which corresponds to thymine, a nucleic base fragmented from DNA (Supplementary; Table 4-9). Their differing biochemical origins will allow for a visual representation of the cell structural information observed in each layer.

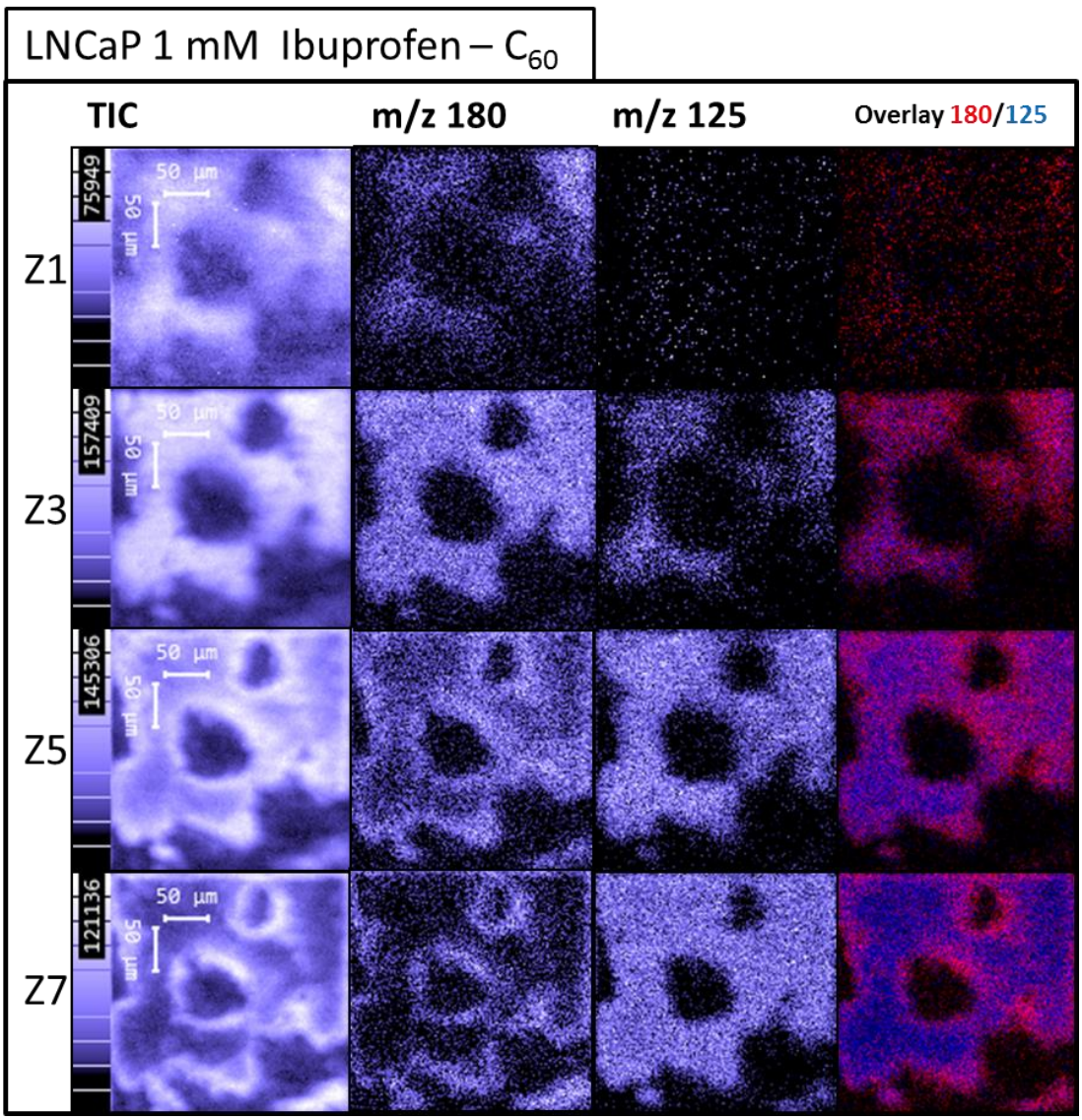

Figure 4.9: ToF-SIMS images highlighting the differences of labelled *m/z* species during the depth profiling for the LNCaP species. The Z values denote the etch layer number through the sample as a result of depth profiling through the sample. The data was acquired using the C_{60}^+ ion beam, at an image width of 280x280 µm with 128x128 pixels. The images shown are negative mode.

As the ion beam etches through the molecular layers with higher C60 ion beam dose, less of the fragment species associated with the membrane is observed, *m/z* 180, and more of the DNA fragment species is detected, *m/z* 125 (Figure 4.9). This is due to the C60 ion beam etching away the uppermost surface of the sample, through the membrane, allowing for intracellular material to be observed. This is highlighted by the overlay image of these two species. To explore the instrument sensitivity to smaller molecules, ibuprofen and its metabolites were targeted.

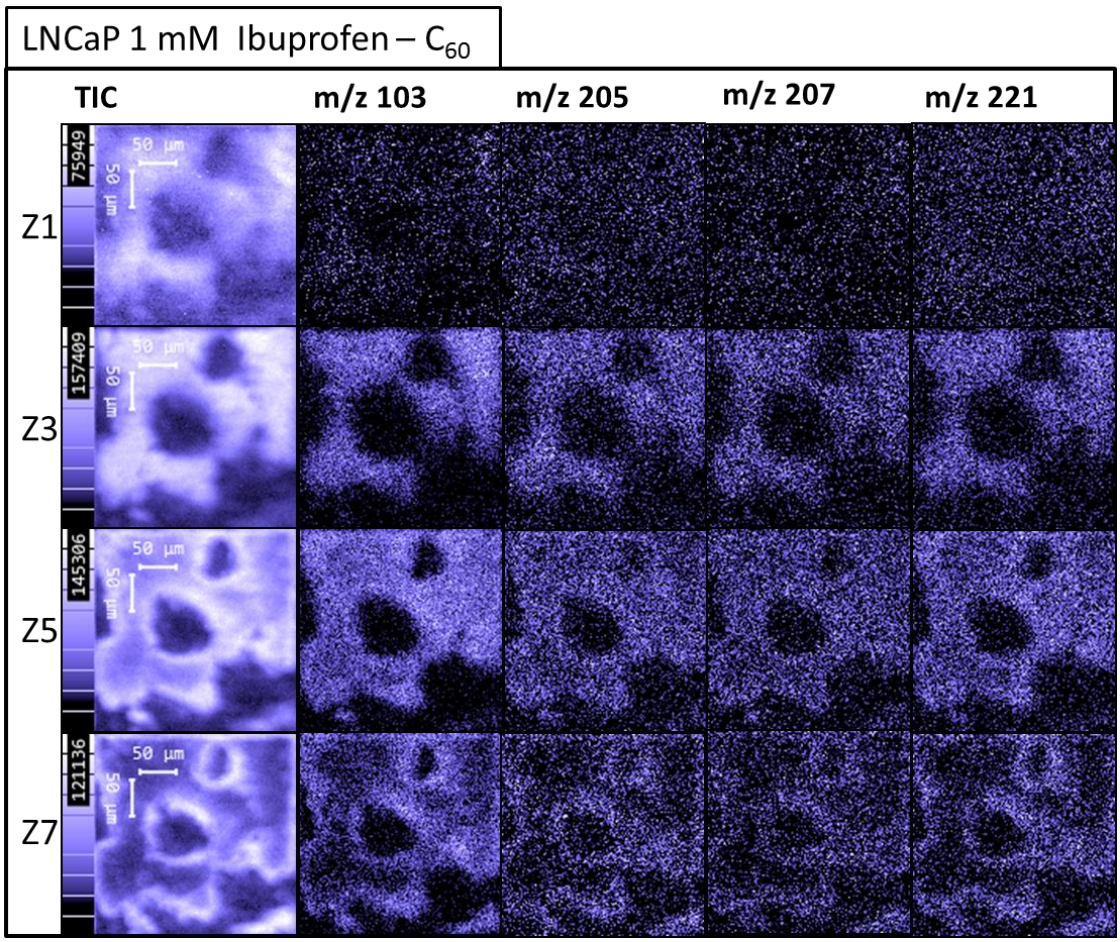

Figure 4.10: ToF-SIMS images highlighting the differences between the ibuprofen metabolites for the control versus the 1 mM ibuprofen for the LNCaP cell line. The Z values denote the etch layer number through the sample as a result of depth profiling through the sample. The intensity scale and max count for each layer is shown on the left hand side. The data was acquired using the C60+ ion beam, at an image width of 280x280 µm with 128x128 pixels. The images shown are negative mode.

In Figure 4.10, the distribution of signal from the ibuprofen and its metabolites (Figure 4.2) is seen to concentrate around the cell membrane region. None of the metabolites are observed in the control images, further confirming the signal belongs to the ibuprofen metabolites (Supplementary; Figure 4.14, Figure 4.15). This immediately highlights the usefulness of high spatial resolution in order to observe spatial distribution of molecules for cellular material. Therefore, this data highlights the benefits of using SIMS for cell based lipidomic experiments.

4.5. Conclusion

The data acquired clearly demonstrates that the normal prostatic cell line, PNT2-C2, is relatively unaffected by ibuprofen. Whereas, following the MTT assay, the cancerous cell lines (LNCaP, LNCaP-C42, and LNCaP-C4-2B) show clear metabolic decline with increasing ibuprofen concentration. This highlights the potential for ibuprofen to be used as an alternative treatment approach, due to little influence on non-cancerous cell lines as a model for healthy tissue. The data also exhibits an overall increase in arachidonic acid post drug addition. This causes changes in the conversion of phosphatidic acid and membrane phospholipids to arachidonic acid. Overall for the cancerous cell lines, metabolic changes occur, causing differences for the PA and PI species with respect to addition of drug. Future work will focus on this result, allowing for more information into why this change occurs.

Comparison of the two mass spectrometry imaging techniques, allows for a clear insight into the overall complementary nature of these methods, providing a more comprehensive overview of the changes to each cell line, as a result of increasing drug concentration. DESI provides much more information about changing intact lipid species, as observed within the mass range *m/z* 600-900, whereas ToF-SIMS analysis provides high spatial resolution images and as a result, spatial distribution information can be obtained for drug metabolites. Future work will employ larger cluster primary ions for ToF-SIMS, including water clusters, which have been shown to enhance molecular sensitivity towards intact lipids and also offer sub micrometer resolution[13].

4.6. Acknowledgments

The author acknowledges and gives thanks for the work and services provided by the following departments

- EPSRC and Waters for funding of a studentship to the author
- ToF-SIMS instrument EP/S019863/1

4.7. References

(1) Rawla, P. Epidemiology of Prostate Cancer. *World J. Oncol.* **2019**, *10* (2), 63–89. https://doi.org/10.14740/wjon1191.

(2) Cancer Research UK - Prostate Cancer Statistics 2019 https://www.cancerresearchuk.org/health-professional/cancer-statistics/statistics-by-cancer-type/prostate-cancer#heading-Two.

(3) Alizadeh, M.; Alizadeh, S. Survey of Clinical and Pathological Characteristics and Outcomes of Patients With Prostate Cancer. *Glob. J. Health Sci.* **2014**, *6* (7), 49–57. https://doi.org/10.5539/gjhs.v6n7p49.

(4) Patrikidou, A.; Loriot, Y.; Eymard, J.-C.; Albiges, L.; Massard, C.; Ileana, E.; Di Palma, M.; Escudier, B.; Fizazi, K. Who Dies from Prostate Cancer? *Prostate Cancer Prostatic Dis.* **2014**, *17* (4), 348–352. https://doi.org/10.1038/pcan.2014.35.

(5) Nguyen-Nielsen, M.; Frøslev, T.; Friis, S.; Borre, M.; Harving, N.; Søgaard, M. Completeness of Prostate Cancer Staging in the Danish Cancer Registry, 2004–2009. *Clin. Epidemiol.* **2012**, *4* (Suppl 2), 17–23. https://doi.org/10.2147/CLEP.S32004.

(6) Nadal, R.; Schweizer, M.; Kryvenko, O. N.; Epstein, J. I.; Eisenberger, M. A. Small Cell Carcinoma of the Prostate. *Nat. Rev. Urol.* **2014**, *11* (4), 213–219. https://doi.org/10.1038/nrurol.2014.21.

(7) Verbeek, J. F. M.; Roobol, M. J. What Is an Acceptable False Negative Rate in the Detection of Prostate Cancer? *Transl. Androl. Urol.* **2018**, *7* (1), 54–60. https://doi.org/10.21037/tau.2017.12.12.

(8) Jonas Hugosson, Johan Stranne, Sigrid V. Carlsson. Radical Retropubic Prostatectomy: A Review of Outcomes and Side-Effects. *Acta Oncol. 50*, 92–97.

(9) Andrews, J.; Djakiew, D.; Krygier, S.; Andrews, P. Superior Effectiveness of Ibuprofen Compared with Other NSAIDs for Reducing the Survival of Human Prostate Cancer Cells. *Cancer Chemother. Pharmacol.* **2002**, *50* (4), 277–284. https://doi.org/10.1007/s00280-002-0485-8.

(10) Mahmud, S.; Franco, E.; Aprikian, A. Prostate Cancer and Use of Nonsteroidal Anti-Inflammatory Drugs: Systematic Review and Meta-Analysis. *Br. J. Cancer* **2004**, *90* (1), 93–99. https://doi.org/10.1038/sj.bjc.6601416.

(11) Eberlin, L. S.; Ferreira, C. R.; Dill, A. L.; Ifa, D. R.; Cooks, R. G. Desorption Electrospray Ionization Mass Spectrometry for Lipid Characterization and Biological Tissue Imaging. *Biochim. Biophys. Acta BBA - Mol. Cell Biol. Lipids* **2011**, *1811* (11), 946–960. https://doi.org/10.1016/j.bbalip.2011.05.006.

(12) Passarelli, M. K.; Winograd, N. Lipid Imaging with Time-of-Flight Secondary Ion Mass Spectrometry (ToF-SIMS). *Biochim. Biophys. Acta BBA - Mol. Cell Biol. Lipids* **2011**, *1811* (11), 976–990. https://doi.org/10.1016/j.bbalip.2011.05.007.

(13) Tian, H.; Six, D. A.; Krucker, T.; Leeds, J., A.; Winograd, N. Subcellular Chemical Imaging of Antibiotics in Single Bacteria Using C60-Secondary Ion Mass Spectrometry. *Anal. Chem.* **2017**, *89*, 5050–5057. https://doi.org/DOI: 10.1021/acs.analchem.7b00466.

(14) Bushra, R.; Aslam, N. An Overview of Clinical Pharmacology of Ibuprofen. *Oman Med. J.* **2010**, *25* (3), 155–1661. https://doi.org/10.5001/omj.2010.49.

(15) YANG, P.; CARTWRIGHT, C. A.; LI, J.; WEN, S.; PROKHOROVA, I. N.; SHUREIQI, I.; TRONCOSO, P.; NAVONE, N. M.; NEWMAN, R. A.; KIM, J. Arachidonic Acid Metabolism in Human Prostate Cancer. *Int. J. Oncol.* **2012**, *41* (4), 1495–1503. https://doi.org/10.3892/ijo.2012.1588.

(16) Ablin, R., J.; Mason, M. *Metastasis of Prostate Cancer*; Cancer Metastasis - Biology and Treatment; Springer, 2008; Vol. 10.

(17) Koontongkaew, S.; Monthanapisut, P.; Saensuk, T. Inhibition of Arachidonic Acid Metabolism Decreases Tumor Cell Invasion and Matrix Metalloproteinase Expression. *Prostaglandins Other Lipid Mediat.* **2010**, *93* (3), 100–108. https://doi.org/10.1016/j.prostaglandins.2010.07.002.

(18) Sumida, C.; Graber, R.; Nunez, E. Role of Fatty Acids in Signal Transduction: Modulators and Messengers. *Prostaglandins Leukot. Essent. Fatty Acids* **1993**, *48*, 117–122.

(19) Pérez, R.; Matabosch, X.; Llebaria, A.; Balboa, M. A.; Balsinde, J. Blockade of Arachidonic Acid Incorporation into Phospholipids Induces Apoptosis in U937 Promonocytic Cells. *J. Lipid Res.* **2006**, *47* (3), 484–491. https://doi.org/10.1194/jlr.M500397-JLR200.

(20) Comprehensive study of ibuprofen and its metabolites in activated sludge batch experiments and aquatic environment | Elsevier Enhanced Reader https://reader.elsevier.com/reader/sd/pii/S0048969712011643?token=7902B11774D35B76E25BB5143F1465C36A555779CE0BF3321C25E3DE17DF8B724C3FDCE61B634228D92B02304E25C834 (accessed Sep 9, 2020). https://doi.org/10.1016/j.scitotenv.2012.08.073.

(21) Horoszewicz, J. S.; Leong, S. S.; Kawinski, E.; Karr, J. P.; Rosenthal, H.; Chu, T. M.; Mirand, E. A.; Murphy, G. P. LNCaP Model of Human Prostatic Carcinoma. *Cancer Res.* **1983**, *43* (4), 1809–1818.

(22) van Steenbrugge, G. J.; van Uffelen, C. J.; Bolt, J.; Schröder, F. H. The Human Prostatic Cancer Cell Line LNCaP and Its Derived Sublines: An in Vitro Model for the Study of Androgen Sensitivity. *J. Steroid Biochem. Mol. Biol.* **1991**, *40* (1–3), 207–214.

(23) MuraliKrishna, P. S.; Gondi, C. S.; Lakka, S. S.; Julta, A.; Estes, N.; Gujrati, M.; Rao, J. S. RNA Interference-Directed Knockdown of Urokinase Plasminogen Activator and Urokinase Plasminogen Activator Receptor Inhibits Prostate Cancer Cell Invasion, Survival and Tumorigenicity In Vivo. *J. Biol. Chem.* **2005**, *280* (43), 36529–36540. https://doi.org/10.1074/jbc.M503111200.

(24) Wu, H.-C.; Hsieh, J.-T.; Gleave, M. E.; Brown, N. M.; Pathak, S.; Chung, L. W. K. Derivation of Androgen-Independent Human LNCaP Prostatic Cancer Cell Sublines: Role of Bone Stromal Cells. *Int. J. Cancer* **1994**, *57* (3), 406–412. https://doi.org/10.1002/ijc.2910570319.

(25) Cussenot, O.; Berthon, P.; Berger, R.; Mowszowicz, I.; Faille, A.; Hojman, F.; Teillac, P.; Le Duc, A.; Calvo, F. Immortilization of Human Adult Normal Prostatic Epithelial Cell by Liposomes Containing Large T-SV40 Gene. *J. Urol.* **1991**, *143*, 881–886.

(26) Investigation of the Impact of Desorption Electrospray Ionization Sprayer Geometry on Its Performance in Imaging of Biological Tissue | Analytical Chemistry https://pubs.acs.org/doi/abs/10.1021/acs.analchem.6b00345 (accessed Jan 11, 2021).

(27) Chong, J.; Wishart, D. S.; Xia, J. Using MetaboAnalyst 4.0 for Comprehensive and Integrative Metabolomics Data Analysis. *Curr. Protoc. Bioinforma.* **2019**, *68* (1), e86. https://doi.org/10.1002/cpbi.86.

(28) Phan, N. T. N.; Munem, M.; Ewing, A. G.; Fletcher, J. S. MS/MS Analysis and Imaging of Lipids across Drosophila Brain Using Secondary Ion Mass Spectrometry. *Anal. Bioanal. Chem.* **2017**, *409* (16), 3923–3932. https://doi.org/10.1007/s00216-017-0336-4.

4.8. Supplementary

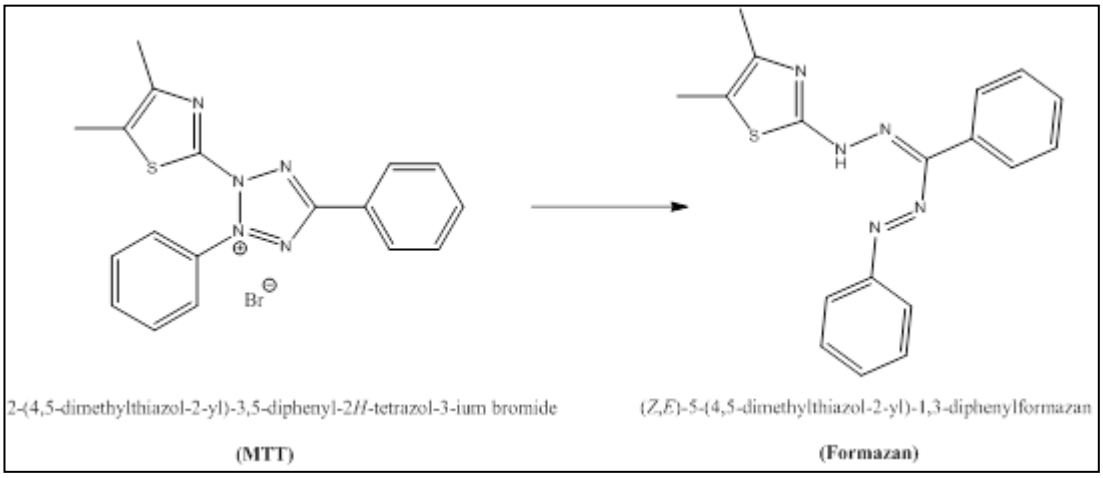

Figure 4.11: The metabolic conversion of MTT into formazan exhibited in the MTT assay.

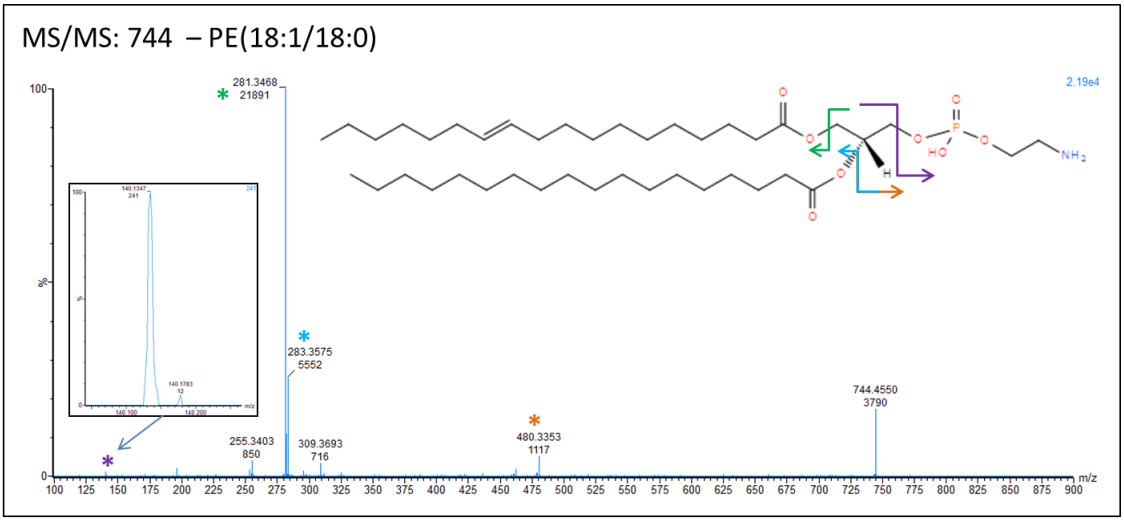

Parent Ion m/z	Daughter Ion m/z	Fragment theoretical mass	Fragment Assignment	Putative Assignment
744.5450	140.1371	140.0118	Ethanolamine phosphate ion	PE(18:1/18:0)
	281.3503	281.2486	sn2 RCOO- ion	
	283.3609	283.2643	sn1 RCOO- ion	
	480.3398	480.3096	Loss of sn2 acyl chain as ketene (RCH=C=O) from [M-H]-	
	460.3217	460.2834	Neutral loss of sn1 RCOOH group from [M-H]-	
	462.3426	462.2990	Neutral loss of sn2 RCOOH group from [M-H]-	

Figure 4.12: A demonstration of an MS/MS spetrum for *m/z* 744. The structure for this species has been shown and the relative framents have been superimposed upon the structure. The corresponding fragment peaks have been highlighted with an astericks of the same colour. Below, is a list of the fragments observed and the assignments and associated theoretical masses. The data was acquired using the Xevo-G2-XS instrument with DESI ionisation source, in negative mode.

Table 4-5: The top loaded *m/z* values, following PCA for each of the cell lines, LNCaP, LNCaP-C42 and LNCaP-C42B, postMS/MS experiments. Each *m/z* value has associated fragment ions and the assignment and theoretical mass. The putative assignment for each *m/z* value has been labelled. Rows highlighted in blue show the fragment species conveying the minor intensity lipid species.

Parent Ion *m/z*	Daughter Ion *m/z*	Fragment theoretical mass	Fragment Assignment	Putative Assignement
606.3769	140.1002	140.0118	Ethanolamine phosphate ion	PE(16:0/10:0)
	171.0991	171.1391	sn2 RCOO- ion	
	255.2326	255.2330	sn1 RCOO- ion	
623.3036	152.9963	152.9958	Glycerol-3-phosphate ion with loss of H2O	PA(18:1/10:0)
	171.0135	171.1391	sn2 RCOO- ion	
	281.2464	281.2486	sn1 RCOO- ion	
641.4247	152.9963	152.9958	Glycerol-3-phosphate ion with loss of H2O	PA(22:3/10:0)
	307.0108	307.1316	Neutral loss of sn1 RCOOH group from [M-H]-	
	325.1856	325.1422	Loss of sn1 acyl chain as ketene (RCH=C=O) from [M-H]-	
	333.9827	333.2799	sn1 RCOO- ion	
653.4625	159.0592	152.9958	Glycerol-3-phosphate ion with loss of H2O	PA(P-16:0/18:3)
	171.1071	171.0064	Glycerol-3-phosphate ion	
	375.1887	375.2306	Neutral loss of sn2 RCOOH group from [M-H]-	
	255.2294	255.2330	FA 16:0 SN2 RCOO- ion	
	277.1841	277.2173	FA 18:3 SN1 RCOO- ion	
675.5135	171.1366	171.0064	Glycerol-3-phosphate ion	PA (16:0/18:0)

	255.2196	255.2330	sn1 RCOO- ion	
	283.2610	283.2643	sn2 RCOO- ion	
700.5218	140.0130	140.0118	Ethanolamine phosphate ion	PE(P-16:0_18:1)
	152.9963	152.9958	Glycerol-3-phosphate ion with loss of H2O	
	255.2326	255.2330	FA 16:0 SN1 RCOO- ion	
	281.2464	281.2486	FA 18:1 SN2 RCOO- ion	
	418.2718	418.2728	Neutral loss of sn2 RCOOH group from [M-H]-	
	436.2776	436.2834	Loss of sn2 acyl chain as ketene (RCH=C=O) from [M-H]-	
716.5244	140.0154	140.0118	Ethanolamine phosphate ion	PE(16:0/18:1)
	196.0379	196.0000	Loss of plasmenyl group in PE	
	255.2359	255.2330	FA 16:0 SN1 RCOO- ion	
	281.2498	281.2486	FA 18:1 SN2 RCOO- ion	
	452.2792	452.2783	Loss of sn2 acyl chain as ketene (RCH=C=O) from [M-H]-	
	460.2831	460.2834	Neutral loss of sn1 RCOOH group from [M-H]-	
	253.2195	253.2173	FA 16:1 SN1 RCOO- ion	
	283.2610	283.2643	FA 18:0 SN2 RCOO- ion	Minor species - PE(16:1/18:0)
722.5034	140.0106	140.0118	Ethanolamine phosphate ion	PE(P-16:0/20:4)
	259.2433	259.2431	Loss of CO2 from sn2 RCOO- ion (PUFA)	
		303.2330	FA 20:4 SN2 RCOO- ion	
	418.2718	418.2728	Neutral loss of sn2 RCOOH group from [M-H]-	

	436.2819	436.2834	Loss of sn2 acyl chain as ketene (RCH=C=O) from [M-H]-	
	482.2621	482.2677	Neutral loss of plasmenyl group RCH=CHOH) from [M-H]-	
728.5585	281.2498	281.2486	FA 18:1 SN2 RCOO- ion	PE(P-18:0/18:1)
	140.0130	140.0118	Ethanolamine phosphate ion	
	152.9887	152.9958	Glycerol-3-phosphate ion with loss of H2O	
	464.3086	464.3147	Loss of sn2 acyl chain as ketene (RCH=C=O) from [M-H]-	
	309.2775	309.2799	FA 20:1 SN2 RCOO- ion	
	436.2819	436.2834	Loss of sn2 acyl chain as ketene (RCH=C=O) from [M-H]-	Minor species - PE(P-16:0/20:1)
742.5389	140.0179	140.0118	Ethanolamine phosphate ion	PE(18:1/18:1)
	196.0437	196.0000	Loss of plasmenyl group in PE	
	281.2498	281.2486	sn1 RCOO- ion	
	460.2783	460.2834	Neutral loss of sn2 RCOOH group from [M-H]-	
	478.2977	478.2939	Loss of sn2 acyl chain as ketene (RCH=C=O) from [M-H]-	Minor species - PE(16:0/20:2)
747.5098	152.9988	152.9958	Glycerol-3-phosphate ion with loss of H2O	PG(18:1/16:0)
	255.2359	255.2330	sn2 RCOO- ion	
	281.2498	281.2486	sn1 RCOO- ion	
	391.2314	391.2255	Neutral loss of sn1 RCOOH group and glycerol from [M-H]-	

	465.2747	465.2623	Neutral loss of sn1 RCOOH group from [M-H]-	
	483.2782	483.2729	Loss of sn1 acyl chain as ketene (RCH=C=O) from [M-H]-	
748.5224	140.0057	140.0118	Ethanolamine phosphate ion	PE(P-18:1/20:4)
	152.9988	152.9958	Glycerol-3-phosphate ion with loss of H2O	
	259.2400	259.2431	Loss of CO2 from sn2 RCOO- ion (PUFA)	
	303.2290	303.2330	sn2 RCOO- ion PE(P-18:1/20:4)	
	329.2501	329.2486	sn2 RCOO- ion	
	436.2690	436.2834	Loss of sn2 acyl chain as ketene (RCH=C=O) from [M-H]-	Minor species - PE(P-16:0/22:5)
750.5410	140.0130	140.0118	Ethanolamine phosphate ion	PE(P-18:0/20:4)
	196.0408	196.0000	Loss of plasmenyl group in PE	
	152.9988	152.9958	Glycerol-3-phosphate ion with loss of H2O	
	303.2325	303.2330	FA 20:4 SN2 RCOO- ion	
	259.2400	259.2431	Loss of CO2 from sn2 RCOO- ion (PUFA)	
	464.3130	464.3147	Loss of sn2 acyl chain as ketene (RCH=C=O) from [M-H]	
	331.2657	331.2643	FA 22:4 SN2 RCOO- ion	
	436.2861	436.2834	Loss of sn2 acyl chain as ketene (RCH=C=O) from [M-H]-	Minor species - PE(P-16:0/22:4)
752.5560	140.0009	140.0118	Ethanolamine phosphate ion	PE(P-18:0/20:3)
	196.0265	196.0000	Loss of plasmenyl group in PE	
	305.2421	305.2486	sn2 RCOO- ion	

	446.2848	446.3041	Neutral loss of sn2 RCOOH group from [M-H]-	
	464.3041	464.3147	Loss of sn2 acyl chain as ketene (RCH=C=O) from [M-H]-	
	333.2725	333.2799	sn2 RCOO- ion	
	418.2634	418.2728	Neutral loss of sn2 RCOOH group from [M-H]-	
	436.2819	436.2834	Loss of sn2 acyl chain as ketene (RCH=C=O) from [M-H]-	
	512.3731	512.3147	Neutral loss of plasmenyl group RCH=CHOH) from [M-H]-	Minor species - PE(P-16:0/22:3)
760.5056	152.9988	152.9958	Glycerol-3-phosphate ion with loss of H2O	PS(16:0/18:1)
	255.2326	255.2330	FA 16:0 SN1 RCOO- ion	
	281.2464	281.2486	FA 18:1 SN2 RCOO- ion	
	391.2233	391.2255	Neutral loss of sn2 RCOOH group and serine from [M-H]-	
	409.2352	409.2361	Loss of sn2 acyl chain as ketene (RCH=C=O) and serine from [M-H]-	
	417.2345	417.2412	Neutral loss of sn1 RCOOH group and serine from [M-H]-	
	673.4684	673.4814	Loss of serine from precursor ion	
766.5375	140.0082	140.0118	Ethanolamine phosphate ion	PE (20:4/18:0)
	196.0379	196.0000	Loss of plasmenyl group in PE	
	283.2645	283.2643	FA 18:0 SN2 RCOO- ion	
	303.2325	303.2330	FA 20:4 SN1 RCOO- ion	

	462.3044	462.2990	Neutral loss of sn1 RCOOH group from [M-H]-	
	480.3047	480.3096	Loss of sn1 acyl chain as ketene (RCH=C=O) from [M-H]-	
	305.2456	305.2486	FA 18:1 SN2 RCOO- ion	
	281.2430	281.2486	FA 20:3 SN1 RCOO- ion	
	484.2459	484.2834	Neutral loss of sn2 RCOOH group from [M-H]-	Minor species - PE (20:3/18:1)
768.5518	152.9937	152.9958	Glycerol-3-phosphate ion with loss of H2O	PE(18:0/20:3)
	283.2541	283.2643	sn1 RCOO- ion	
	305.2421	305.2486	sn2 RCOO- ion	
773.5336	152.9963	152.9958	Glycerol-3-phosphate ion with loss of H2O	PG(18:1/18:1)
	281.2498	281.2486	sn1 RCOO- ion	
774.5364	140.0106	140.0118	Ethanolamine phosphate ion	PE (P-18:0/20:6)
	152.9937	152.9958	Glycerol-3-phosphate ion with loss of H2O	
	196.0351	196.0000	Loss of plasmenyl group in PE	
	327.2295	327.2330	FA 20:6 SN2 RCOO- ion	
	464.3086	464.3147	Loss of sn2 acyl chain as ketene (RCH=C=O) from [M-H]-	
	329.2464	329.2486	FA 20:5 SN2 RCOO- ion	
	462.3044	462.2990	Loss of sn2 acyl chain as ketene (RCH=C=O) from [M-H]-	Minor species - PE (P-18:1/20:5)
788.5448	152.9963	152.9958	Glycerol-3-phosphate ion with loss of H2O	PS (18:1/18:0)
	281.2498	281.2486	FA 18:1 SN2 RCOO- ion	

	283.2645	283.2643	FA 18:0 SN1 RCOO- ion	
	419.2558	419.2568	Neutral loss of sn2 RCOOH group and serine from [M-H]-	
	417.2345	417.2412	Neutral loss of sn1 RCOOH group and serine from [M-H]-	
	435.2481	435.2517	Loss of sn1 acyl chain as ketene (RCH=C=O) and serine from [M-H]-	
	437.2655	437.2674	Loss of sn2 acyl chain as ketene (RCH=C=O) and serine from [M-H]-	
	701.5075	701.5127	Loss of serine from precursor ion	
790.5374	152.9861	152.9958	Glycerol-3-phosphate ion with loss of H2O	PE(18:1/22:5)
	329.2352	329.2486	sn2 RCOO- ion	
	460.6911	460.2834	Neutral loss of sn2 RCOOH group from [M-H]-	
794.5617	140.0179	140.0118	Ethanolamine phosphate ion	PE (18:0/22:4)
	196.0293	196.0000	Loss of plasmenyl group in PE	
	283.2610	283.2643	FA 18:0 SN2 RCOO- ion	
	331.2619	331.2643	FA 22:3 SN1 RCOO- ion	
	462.2868	462.2990	Neutral loss of sn1 RCOOH group from [M-H]-	
	480.2913	480.3096	Loss of sn1 acyl chain as ketene (RCH=C=O) from [M-H]-	
	510.3000	510.2990	Neutral loss of sn2 RCOOH group from [M-H]-	
802.554	152.9963	152.9958	Glycerol-3-phosphate ion with loss of H2O	PS(O-20:0/18:1)
	281.2430	281.2486	sn2 RCOO- ion	

	433.2694	433.3088	Neutral loss of sn2 RCOOH group and serine from [M-H]-	
	451.2701	451.3194	Loss of sn2 acyl chain as ketene (RCH=C=O) and serine from [M-H]-	
	715.5007	715.5647	Loss of serine from precursor ion	
835.5266	152.9937	152.9958	Glycerol-3-phosphate ion with loss of H2O	PI(18:1/16:0)
	281.2464	281.2486	FA 18:1 SN1 RCOO- ion	
	255.2359	255.2330	FA 16:0 SN2 RCOO- ion	
	223.0027	223.0013	Inositol phosphate ion - 2 H2O	
	241.0124	241.0119	Inositol phosphate ion - H2O	
	259.0325	259.0225	Inositol phosphate ion	
	315.0478	315.0487	Glycerophosphoinositol -H2O	
	579.2787	579.2940	Neutral loss of sn2 RCOOH group from [M-H]-	
	553.2718	553.2783	Neutral loss of sn1 RCOOH group from [M-H]-	
848.6545	153.0039	152.9958	Glycerol-3-phosphate ion with loss of H2O	PC(18:1/20:1)
	281.2464	281.2486	sn1 RCOO- ion	
	309.2810	309.2799	sn2 RCOO- ion	
	798.6561	798.6018	Loss of CH3 and chloride from precursor ion	
861.5361	152.9963	152.9958	Glycerol-3-phosphate ion with loss of H2O	PI(18:1/18:1)
	223.0057	223.0013	Inositol phosphate ion - 2 H2O	
	241.0124	241.0119	Inositol phosphate ion - H2O	
	281.2498	281.2486	sn2 RCOO- ion	

	417.2303	417.2412	Neutral loss of sn1 RCOOH group and inositol from [M-H]-	
	579.3033	579.2940	Neutral loss of sn1 RCOOH group from [M-H]-	
	597.3052	597.3045	Loss of sn1 acyl chain as ketene (RCH=C=O) from [M-H]-	
863.5562	152.9937	152.9958	Glycerol-3-phosphate ion with loss of H2O	PI(18:0/18:1)
	223.0088	223.0013	Inositol phosphate ion - 2 H2O	
	241.0124	241.0119	Inositol phosphate ion - H2O	
	281.2532	281.2486	sn2 RCOO- ion	
	283.2576	283.2643	sn1 RCOO- ion	
	419.2516	419.2568	Neutral loss of sn2 RCOOH group and inositol from [M-H]-	
	581.3097	581.3096	Neutral loss of sn2 RCOOH group from [M-H]-	
864.5624	152.9963	152.9958	Glycerol-3-phosphate ion with loss of H2O	PS (22:4_20:1)
	309.2846	309.2799	sn2 RCOO- ion	
	331.2657	331.2643	sn1 RCOO- ion	
	445.2652	445.2725	Neutral loss of sn1 RCOOH group and serine from [M-H]-	
	777.5272	777.5440	Loss of serine from precursor ion	
885.5417	152.9937	152.9958	Glycerol-3-phosphate ion with loss of H2O	PI(20:4/18:0)
	222.9966	223.0013	Inositol phosphate ion - 2 H2O	
	241.0092	241.0119	Inositol phosphate ion - H2O	
	283.2532	283.2643	sn1 RCOO- ion	

	297.0462	297.0381	Glycerophosphoinositol -2H2O
	303.2290	303.2330	sn2 RCOO- ion
	419.2516	419.2568	Neutral loss of sn2 RCOOH group and inositol from [M-H]-
	581.3097	581.3096	Neutral loss of sn2 RCOOH group from [M-H]-

Table 4-6: Top highest loaded species for the LNCaP-C42 post drug addition

C42 Control					
m/z	Putative Assignment	PC1	PC2	PPM Error	Theoretical *m/z*
687.5356	PA(P-36:0) / PA(O-36:1)	0.19722	-0.13152	3	687.5334
665.3992	PA(34:5)	0.17387	-0.087504	29	665.4188
760.5056	PS(34:1)	0.12342	-0.061471	10	760.5134
651.3428	L-PI(22:2)	0.10951	-0.054106	13	651.3515
605.3284		0.084528	-0.04501		
623.3478	L-PI(20:2)	0.08398	-0.043561	44	623.3202
758.564	PC(34:1)	0.079226	-0.045097	8	758.5705
601.3494	PA(P-20:1)	0.06485	-0.030935	123	601.4239
C42 0.1 mM					
m/z	Putative Assignment	PC1	PC2	PPM Error	Theoretical *m/z*
790.5374	PE (40:6)	-0.13114	-0.1249	2	790.5392
728.5492	PE(P36:1)	-0.13656	0.036389	14	728.56
752.5519	PE(P38:3)	-0.13692	-0.020682	10	752.56
768.5409	PE (38:3)	-0.15516	-0.10832	18	768.5549
750.5364	PE(P-38:4)	-0.16351	-0.0098875	10	750.5443
766.5267	PE (38:4)	-0.18596	-0.15566	16	766.5392
744.545	PE (36:1)	-0.22394	-0.38103	13	744.5549
700.5218	PE(P-34:1)	-0.22869	0.037583	9	700.5236
C42 1 mM					
m/z	Putative Assignment	PC1	PC2	PPM Error	Theoretical *m/z*
862.5463	PS(42:6)	-0.03006	0.034449	16	862.5604
835.5266	PI(34:1)	-0.030382	0.062699	9	835.5342
773.5281	PG(36:2)	-0.040656	0.080222	7	773.5338
861.5361	PI(36:2)	-0.052578	0.083935	15	861.5499
891.579	PI(38:1)	-0.061944	0.089693	19	891.5968
864.5624	PS(42:5)	-0.063247	0.099217	15	864.576
890.5764	PS(44:6)	-0.095114	0.13636	17	890.5917
863.5655	PI(36:1)	-0.10723	0.20174	5	863.5655

Table 4-7: Top highest loaded species for the LNCaP-C42B post drug addition

C42B Control					
m/z	Putative Assignment	PC1	PC2	PPM Error	Theoretical *m/z*
606.3769	PE(26:0)	0.004699	0.10523	61	606.414
628.06		0.0058843	0.12001		
714.5156	PE(36:2)	-0.064383	0.11164	2	714.5079
745.5457	PG(34:2)	-0.023398	-0.13	57	745.5025
846.6511	PC(O-42:6)	0.011656	0.096887	15	846.6382
854.5233	PS(42:10)	0.0092528	0.077096	29	854.4978
862.5463	PS(42:6)	0.030276	-0.11552	16	862.5604
886.5473	PS(44:8)	0.018776	0.50946	14	886.5604
C42B 0.1 Mm					
m/z	Putative Assignment	PC1	PC2	PPM Error	Theoretical *m/z*
836.5333	PE(44:11)	-0.069082	0.15798	11	836.5236
861.5361	PI(36:2)	-0.10203	-0.085748	15	861.5499
788.5448	PS (36:1)	-0.12726	0.15019	0	788.5447
888.5607	PS(44:7)	-0.14042	-0.30902	17	888.576
864.5624	PS(42:5)	-0.17334	0.096545	15	864.576
890.5764	PS(44:6)	-0.19804	-0.15916	17	890.5917
835.5266	PI(34:1)	-0.21194	0.29518	9	835.5342
747.5098	PA (40:6)	-0.27733	-0.12255	11	747.5182
C42B 1 Mm					
m/z	Putative Assignment	PC1	PC2	PPM Error	Theoretical *m/z*
862.5463	PS(42:6)	0.030276	-0.11552	16	862.5604
684.5906	GlcCer(d32:2(2OH))	0.029295	-0.28637	124	684.5056
860.5206	PS(42:7)	0.020188	-0.075247	28	860.5447
739.4017	PA(40:10)	0.013254	-0.075925	44	739.4344
686.5156	PC(P-30:1)	0.0097886	-0.092294	3	686.513
725.3852	PI(26:0)	0.0072449	-0.05389	54	725.4247
698.3607	PS(30:4)	0.0057846	-0.046955	61	698.4039
794.5617	PE 40:4	0.0027356	-0.010945	11	794.5705

Table 4-8: Top highest loaded species for the PNT2-C2 post drug addition

PNT2 Control					
m/z	Putative Assignment	PC1	PC2	PPM Error	Theoretical *m/z*
885.5414	PI (38:4)	0.67632	-0.1519	9	885.5499
788.5448	PS (36:1)	0.39061	0.0045313	0	788.5447
742.545	PE 36:2	0.29942	0.060495	7	742.5392
886.5473	PS(44:8)	0.22904	-0.063751	14	886.5604
766.5267	PE (38:4)	0.22643	0.096524	16	766.5392
887.5537	PI(38:3)	0.20294	-0.12806	13	887.5655
748.5123	PE(P38:5)	0.13812	-0.11004	21	748.5287
722.5034	PE(P-36:4)	0.13398	0.069616	13	722.513
PNT2 0.1 mM					
m/z	Putative Assignment	PC1	PC2	PPM Error	Theoretical *m/z*
744.545	PE 36:1	0.19186	-0.38712	13	744.5549
836.5333	PE(44:11)	0.10543	-0.2424	11	836.5236
863.5655	PI(36:1)	0.092227	-0.4137	5	863.5655
789.5358	PG(38:8)	0.075888	-0.17739	81	789.4712
861.5361	PI(36:2)	0.073104	-0.24979	15	861.5499
745.5457	PG(34:2)	0.070961	-0.23326	57	745.5025
883.5314	PI (38:5)	0.069497	-0.13745	3	883.5342
790.5374	PE (40:6)	0.0682	-0.17642	2	790.5392
PNT2 1 mM					
m/z	Putative Assignment	PC1	PC2	PPM Error	Theoretical *m/z*
750.5364	PE(P-38:4)	-0.0050065	0.0040266	10	750.5443
684.5906	GlcCer(d32:2(2OH))	-0.0068473	0.023407	124	684.5056
802.554	PC(38:7)	-0.0078912	0.017382	18	802.5392
800.5189	PC(38:8)	-0.010365	-0.0005334	5	800.5236
669.4467	PA(34:3)	-0.010615	0.026087	5	669.4501
601.3494	PA(P-20:1)	-0.017138	0.037522	123	601.4239
847.6406	PG(O-42:0)	-0.017584	0.021485	46	847.6797
848.6545	PC(P42:4)	-0.019017	0.027888	0	848.6539

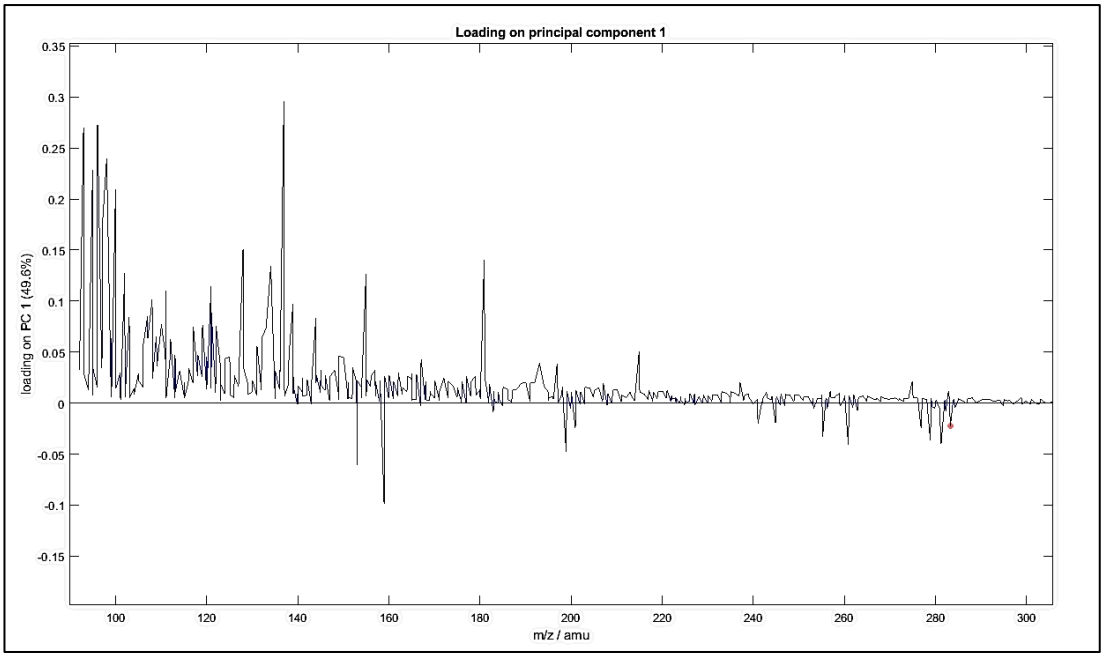

Figure 4.13: The extracted loadings from PC1 following PCA for the LNCaP cell line post ibuprofen drug addition. This data was acquired using the C_{60}^{+} ion beam in negative mode.

Table 4-9: The theoretical masses and assignments of the selected species

m/z	Species	Chemical Structure	Adduct	Theoretical Mass
180.05	PE headgroup fragment	[C5H11NPO4]	$[M-H]^-$	180.0426
125.03	Thymine	[C5H6N2O2]	$[M-H]^-$	125.0357

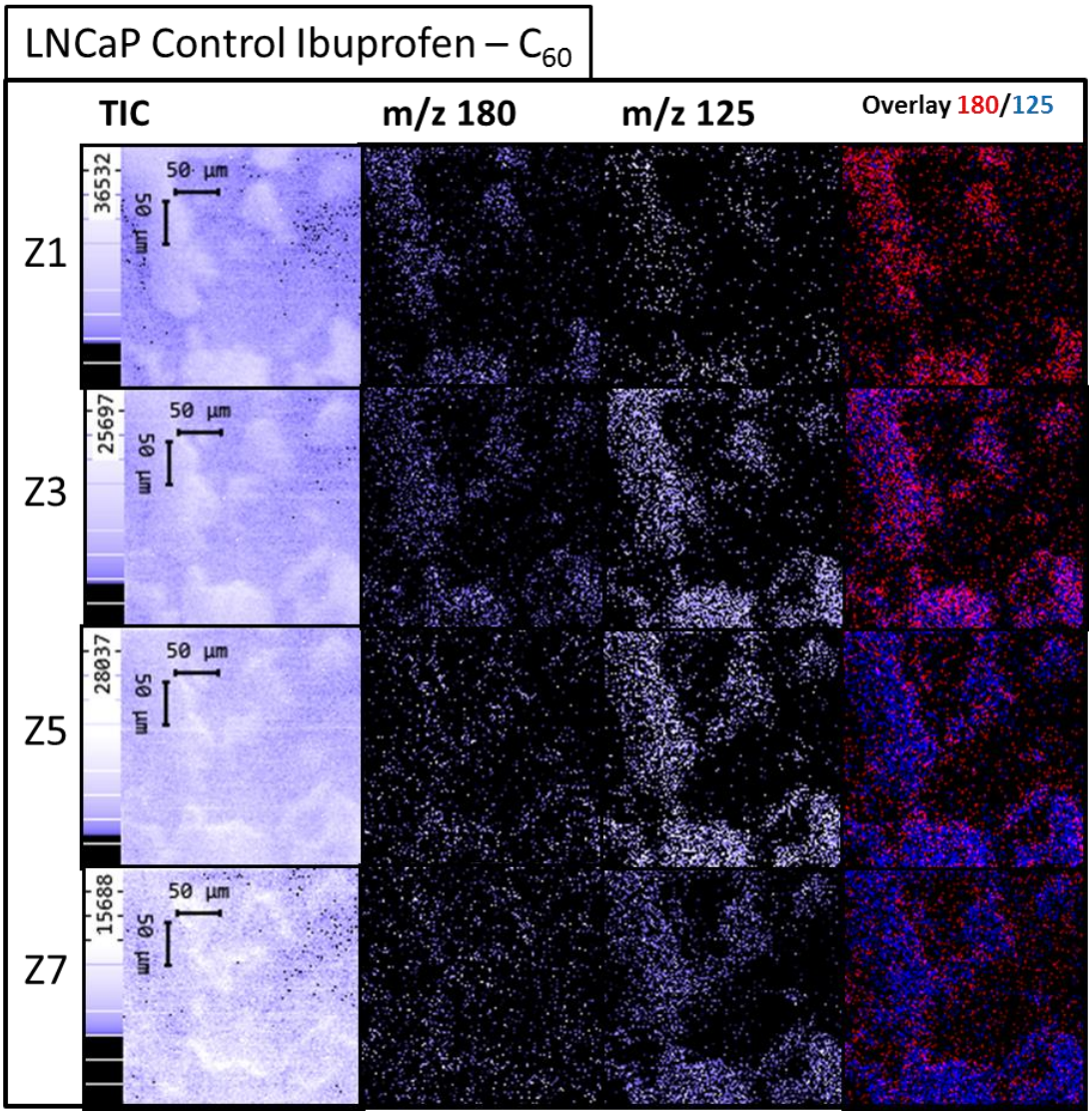

Figure 4.14: ToF-SIMS images highlighting the differences of labelled *m/z* species, during the depth profiling for the LNCaP species. The Z values denote the depth layer through the sample. The data was acquired using the C_{60}^{+} ion beam, at an image width of 280x280 µm with 128x128 pixels. The images shown are negative mode.

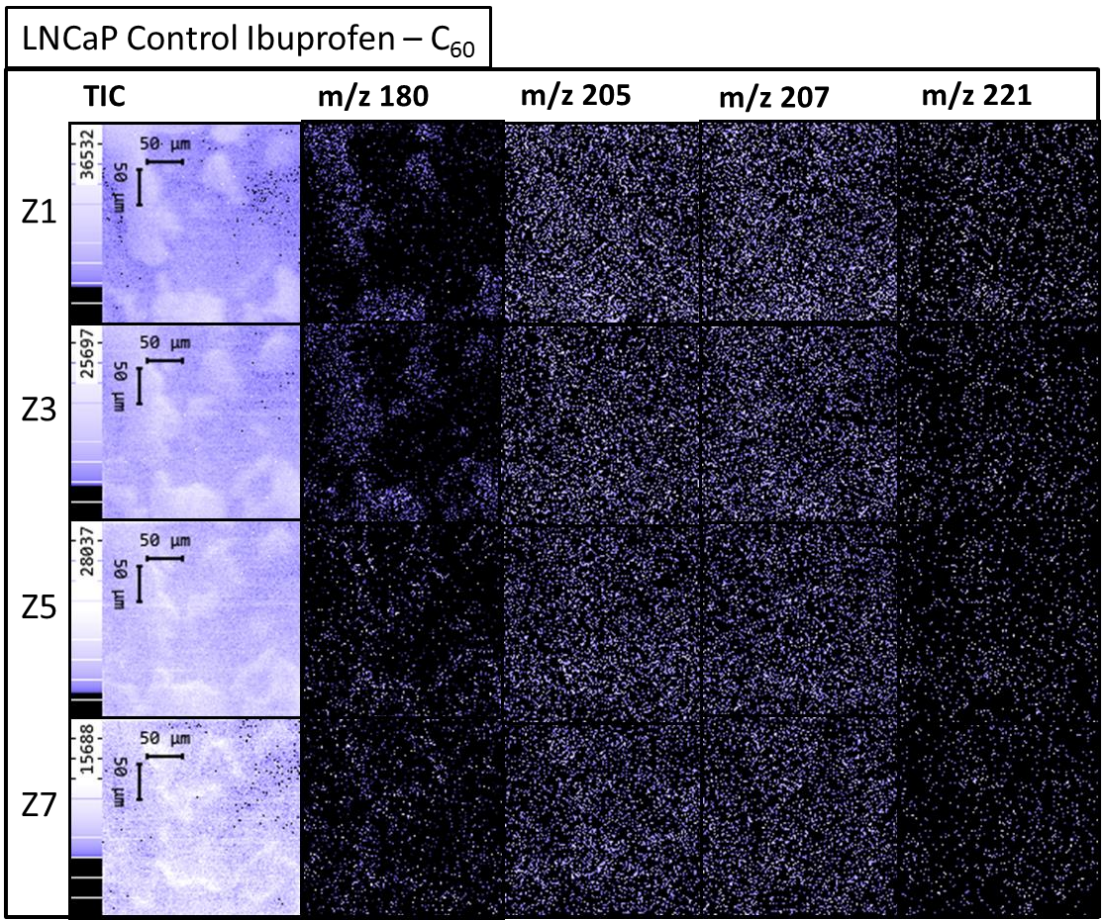

Figure 4.15: ToF-SIMS images highlighting the differences of labeled *m/z* species, corresponding to the ibuprofen metabolites, during the depth profiling for the LNCaP species. The Z values denote the depth layer through the sample. The data was acquired using the C_{60}^{+} ion beam, at an image width of 280x280 µm with 128x128 pixels. The images shown are negative mode.

Chapter 5

Conclusions and Future Work

5. Conclusion and Future Work

This thesis has successfully compared a variety of mass spectrometry imaging techniques using a variety of sample types for lipidomics applications. Using a combination of prostate cancer cell lines, differing in aggression, desorption electrospray ionisation was able to distinguish between these cell lines where immunofluorescent staining was unable to do so. This was due to the ability of DESI to define a lipid profile for the individual cell lines, and apply that information to the mixed pellets. Future work will focus on obtaining the IF stained image for the sections analysed with ToF-SIMS. Also, image fusion of the acquired MSI data to the IF image will be explored[1] to allow for correlation between the lipid profiles with the pathology of the samples and as a result further confirmation of the assigned cell line regions. LC-MS/MS methods could also be explored to enable further examination of the extracted cell lipidome.[2]

Rapid evaporative ionisation mass spectrometry (REIMS) has demonstrated in literature the potential to be utilised for high throughput lipidomic experiments. This study highlighted an optimised protocol for Laser REIMS, which can be expanded to a variety of cell based experiments that allows for the best S/N to be achieved for the lipid region of interest. Future work will explore this method on the cell based experiments described by this thesis.

So far, this work has demonstrated the abilities of these methods to observe the samples in a fairly natural, hydrated state. Therefore the involvement of drug treated samples was examined. An MTT assay initially highlighted the potential of using the NSAID drug, ibuprofen, as an therapeutic treatment approach. This assay revealed that the ibuprofen caused a measurable metabolic decline for only the cancerous cell lines used, and not the normal cell line. DESI analysis of the cancerous cell lines highlighted that an overall rise in phosphatidic acid and phosphatidylinositol species were observed with increasing drug

dose. The high spatial imaging of these samples with secondary ion mass spectrometry highlighted the distribution of the drug and potential metabolites within the sample. This demonstrated that using these methods together gives a plethora of data allowing for different areas to be exploited. Further work will employ MS/MS methods on the ToF-SIMS data to enable an additional degree of confidence to assignments. Also, a range of ion beams will be utilised to observe the differences in species which each ion beam presents. This will allow for a thorough comparison of the strengths of each ion beam available. Additional work will be undertaken to explore the changing lipidome in relation to the biological pathways altered with increasing concentration of drug.

Overall, this thesis demonstrates the ability and benefits of using a variety of mass spectrometry methods for lipidomic experiments due to the complementary nature of the data extracted.

5.1. References

(1) Race, A. M.; Rae, A.; Vorng, J.-L.; Havelund, R.; Dexter, A.; Kumar, N.; Steven, R. T.; Passarelli, M. K.; Tyler, B. J.; Bunch, J.; Gilmore, I. S. Correlative Hyperspectral Imaging Using a Dimensionality-Reduction-Based Image Fusion Method. *Analytical Chemistry* **2020**. https://doi.org/10.1021/acs.analchem.9b05055.

(2) Eiriksson, F. F.; Nøhr, M. K.; Costa, M.; Bödvarsdottir, S. K.; Ögmundsdottir, H. M.; Thorsteinsdottir, M. Lipidomic Study of Cell Lines Reveals Differences between Breast Cancer Subtypes. *PLoS ONE* **2020**, *15* (4), e0231289. https://doi.org/10.1371/journal.pone.0231289.